國立臺灣大學電機資訊學院光電工程學研究所

碩士論文

Graduate Institute of Photonics and Optoelectronics

College of Electrical Engineering and Computer Science

National Taiwan University

Master Thesis

矽核光纖製程和退火方法之改善與探討耦合形波導折射率感測器的優化

Improvement in Fabrication and Annealing Methods of Silicon Cored Fibers and Optimization of Coupled Waveguide Refractive Index Sensors

蘇江平

Chiang-Ping Saw

指導教授：王倫 博士

Advisor: Lon A. Wang, Ph.D.

中華民國 111 年 9 月

September, 2022

doi:10.6342/NTU202204042

誌謝

首先我要感謝我的父母無條件的支持我的教育。也要感謝指導教授王倫教授給予研究上的空間。除此之外。我也感謝在我研究上給與很大幫助和常和我討論的學長威駿，永霖，楷儒，志揚與同學淞普，天行。還有其他在實驗室有緣認識的朋友台憲，皓云，浩丙鑌和證宸等也感謝他們對於很多事情上的幫助。最後我要感謝我的女友文玉給予的支持與陪伴。

2022/09/15

doi:10.6342/NTU202204042

中文摘要

在本論文中，我們研究並提出了提高 SCF 產量和品質的方法。我們還設計了一套用於設計耦合型波導折射率傳感器的指南。在第二章中，我們推斷氣泡的形成導致 SCF 產量低和質量差。我們發現通過增加預形體的內徑可以緩解該問題，並提出了一種新的兩段式 SCF 抽絲方法以配合新的預形體尺寸。我們也設計並建造了這種新方法所需的自動化設備。我們還做了爐體加熱預形體的熱模擬，以了解熔爐的各種參數如何影響抽絲過程中預形體的溫度分佈。在第三章中，我們通過熱模擬和實驗研究了 CO2 雷射退火過程中，SCF 的溫度分佈，以便有效的控制退火過程。我們也建立了一個 SCF 矽核溫度檢測器和 SCF 定位器材以利於退火實驗。我們還研究了 SCF 中單模耦合和單模傳輸的可行性，並編寫了一個程序來識別在少模光纖中傳播的模式的。我們也對 SCF 的光場進行近場測量。在第四章中，我們使用耦合模理論和數值分析來找出提高耦合型波導折射率傳感器性能的方向，並用光學模擬驗證我們的推導。

關鍵字: 矽核光纖、光纖抽絲、雷射退火，折射率感測器，耦合模理論

doi:10.6342/NTU202204042

Abstract

In this thesis, we investigated and developed methods to improve the production and quality of SCF. We also devised a set of guidelines for designing coupling-based waveguide refractive index sensors. In chapter 2, we deduced that the formation of air bubbles causes low yield and poor quality of SCF. We found out the problem can be partly mitigated by increasing the inner diameter of the preform. Therefore, a new two-stage drawing method for SCF drawing is proposed to draw the preforms with new geometry. Automated equipment needed for this new method is designed and built. We also conducted thermal modeling to understand how the furnace parameters affect the temperature distribution of the preform during the drawing process. In chapter 3, we investigated the temperature distribution in SCF during CO2 laser annealing through thermal simulation and experiment so that we can better control the annealing process. A new annealing set-up is built with a thermal monitor and a SCF positioning system. We also investigated the viability of single mode coupling and transmission in SCF and wrote a computer program to identify the amplitude of modes traveling in a few-mode fiber. Near field measurement of SCF is also carried out. In chapter 4, we used Coupled Mode Theory with numerical analysis to devise a set of guidelines for improving performance in a coupled waveguide RI sensor. The results are validated with optical simulation.

Keywords: silicon cored fiber, fiber drawing, fiber annealing, refractive index sensor, coupled mode theory

doi:10.6342/NTU202204042

Statement of contribution

Original Contribution

1. Devising Guidelines for Improving Performance of Coupled Waveguide Sensor
2. Thermal Modelling of Fiber Drawing Furnace and Preform
3. Thermal Modelling of CO2 Laser Annealing Process

General Contribution

1. Designing and building system for two-stage preform drawing system, including all hardware and software
2. Designing and building system for automated fiber drawing
3. Discovering the reason for instable fiber drawing yield: Air bubble formation
4. Set up temperature monitoring and optical positioning systems for CO2 laser annealing, including all hardware and software.
5. Calculating condition for single mode transmission between multimode SCF and writing mode decomposing algorithm to identify amplitude of modes in multimode fiber

doi:10.6342/NTU202204042

Content

doi:10.6342/NTU202204042

doi:10.6342/NTU202204042

doi:10.6342/NTU202204042

doi:10.6342/NTU202204042

LIST OF FIGURES

doi:10.6342/NTU202204042

doi:10.6342/NTU202204042

doi:10.6342/NTU202204042

doi:10.6342/NTU202204042

doi:10.6342/NTU202204042

doi:10.6342/NTU202204042

doi:10.6342/NTU202204042

doi:10.6342/NTU202204042

LIST OF TABLES

doi:10.6342/NTU202204042

Chapter 1 Introduction

1.1 Motivation

Semiconductor fibers, an evolution from silica based optical fibers was first fabricated since 2004 by Fink's group from MIT [1]. The wider range of semiconductor material used as core of the optical fiber provides two advantage in the field of non-linear optics and infrared transmission. The two earliest material used in semiconductor fiber, silicon and germanium, shows much higher third order nonlinearity $\chi^{(3)}$ than silica. They also have higher refractive index suitable for tight mode confinement to maintain the high intensity needed for non-linear optics effect. Previous research had observed non-linear effects such as multiphoton absorption [2], self- and cross-phase modulation (SPM and XPM) [3], as well as four-wave mixing (FWM) [4] in various semiconductor fibers. These effects can be developed for used in all-optical modulation, parametric amplification [5], frequency comb generation [6] and supercontinuum generation [7]. Compared to its planar counterpart, fiber based non-linear devices shows comparable performance with the added advantage of easier integration with other fiber-based system. As for infrared transmission, normal silica fiber is transparent only up to about 2.5 μm [8] due to the presence of oxygen bond. Even though fluoride and chalcogenide glass fiber are transparent up to 9 μm, they are limited by issues of fragility and disintegrates under high optical power [9]. On the other hand, semiconductor such as zinc selenide (ZnSe) and Indium Antimonite (InSb) has low loss up to 20 μm and are very stable under high power transmission [10]. Possible applications include mid-infrared sensors to probe the natural resonance in organic materials, lasers and amplifiers utilizing the high-power transmission capability and huge Raman gain of group IV semiconductor material.

doi:10.6342/NTU202204042

However, for these applications to work well, the semiconductor fiber must be of good quality. Criteria of good quality includes low intrinsic loss, low scattering loss and good mechanical strength. Therefore, in this thesis, we will emphasis our effort in improving the quality of the production of silicon cored fiber, our in-house semiconductor fiber both in the drawing and post processing stage. After prove of concept in silicon cored fiber production and annealing in our lab by previous students, we will try to improve their methods by investigating the physics behind these processes using both simulation and experiments. Knowing the potential of using semiconductor fiber as mid infrared sensors, we investigated criteria that will improve performance of coupled waveguide refractive index sensor to help in designing semiconductor fiber-based sensor in the future.

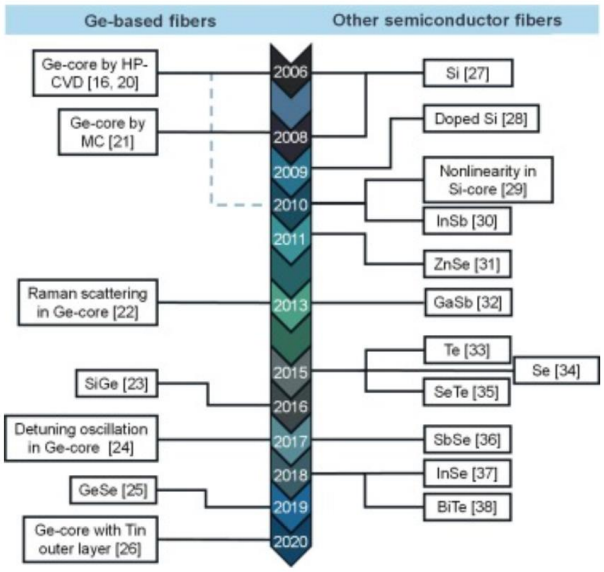

Fig. 1-1 List of semiconductor fibers and first fabricated date

doi:10.6342/NTU202204042

1.2 Literature Review

1.2.1 Silicon-cored Fiber Fabrication

High Pressure Vapor Deposition Method

Silicon-cored fiber (SCF), part of a larger family of semiconductor fibers was first fabricated in 2006 by a group collaboration between Pennsylvania State University and the Optoelectronics Research Centre at the University of Southampton [11] using HPCVD method. A carrier gas is used to transport precursor into hollow glass capillaries with inner diameter down to hundreds of nanometers. The precursor is deposited layer by layer on the inner wall of the capillary until the desired layer thickness is reached or until the pore is completely sealed. Layer by layer deposition enables not only homogenous but heterogeneous making this process suitable for fabrication of multilayer semiconductor transistor structure in fiber [12]. Due to the low temperature of deposition, substance with large thermal coefficient mismatch can be deposited without introducing too much stress. However, the process is time consuming due to the slow reaction at low temperature and takes weeks to fabricate only centimeters of fiber. For SCF fabricated using HPCVD method, the silicon core is in amorphous hydrogenated form which is suitable for non-linear optics due to its large nonlinearity compared to crystalline silicon [13]. However, loss in amorphous silicon is higher than its crystalline counterpart. Therefore, SCF fabricated using HPCVD method required post processing such as annealing to lower the loss. Some semiconductor is deposited as crystalline structure.

doi:10.6342/NTU202204042

Molten Core Drawing (MCD)

Ballato's group at Clemson University first demonstrated the use of molten core drawing (MCD) method for the fabrication of SCF and it becomes the most widely used method for semiconductor drawing today [14]. Semiconductor material in the form of powder or rod is inserted into a glass preform before being drawn at temperature above the glass softening temperature which is around 1900 K. At drawing temperature, the glass can deform but it still has high enough viscosity to contain the liquid semiconductor inside. Utilizing the fact that fused silica's softening temperature is higher than most semiconductors' melting temperature, most semiconductors can be drawn using this method except for materials that will sublimate such as ZnSe. Due to the high drawing temperature, oxygen will diffuse into the core and limit the minimum core size unless a diffusion barrier [15] such as CaO layer is placed between the core and the cladding. With HPCVD method being expensive and time consuming, MCD method is the option for mass production as meters of fiber can be drawn from a preform utilizing commercial glass fiber drawing equipment. Further cost down can be achieved with the use of powder-in-tube [14] instead of rod-in-tube [16] method as single-crystal rod is more than 100 times the price of powder silicon considering the cost-to-weight ratio of the material. Both powder-in-tube and rod-in-tube method will introduce air into the fiber's core due its fill factor of less than 1. Vacuum is applied to the preform during the drawing process to reduce the effect of such problem. Recently, a new method using sol-gel method to form a seamless silica layer surrounding the silicon rod was proposed and the lowest loss (0.1dB/cm) without post processing was recorded [17].

doi:10.6342/NTU202204042

1.2.2 SCF Annealing

Low loss in SCF has been a target since SCF was first fabricated. The loss in SCF is determined by the grain size because the boundaries between crystal grains will scatter the light in the core. Some of the methods used by other groups to increase grain size include furnace annealing [18], rapid photothermal processing [19], laser annealing with argon-ion continuous wave (CW) laser at 488nm [20] and CO2 gas laser at 10.6μm [21]. All of these methods have been widely used in annealing of thin film semiconductor layers. Laser annealing methods involve liquid phase epitaxy while the other methods are solid phase epitaxy. During 488nm laser annealing, the silicon core absorbs the laser energy and is heat up to melting temperature while during CO2 laser annealing, it is the silica cladding that absorbs the laser energy and transfers the heat to the silicon core. As the silicon melts down, the edge where the molten and solid silicon meet is called the phase front. When the laser beam scanned across fiber along the fiber's core axis, the phase front moved along. The silicon region where the phase front sweeps through experienced re-solidification. Under the right condition, crystal growth rate is way higher than nucleation rate, the silicon will have large areas of single crystal region [22]. Otherwise, the silicon solid will be mostly polycrystalline or if the cooling rate is too high, no nuclear is formed and the silicon core become mostly amorphous. To reach the optimum condition for annealing, previous research has pointed out that controlling the temperature gradient and cooling rate along the phase front is crucial similar to Zone Melting or Czochralski Method for producing single crystal wafer [21]. To monitor the temperature gradient and cooling rate we need to develop a temperature monitoring device as will be discussed later.

As the silicon core crystallized, its volume expands and thus the stress in the core of SCF annealed using 488nm laser shows an increase in stress. As the cladding is

doi:10.6342/NTU202204042

not heat up to softening point, the volume mismatch between the cladding and core is so high that the lattice of silicon changes [20]. However, during CO2 laser annealing, as the glass cladding itself will heat up to softening point, it will reshape or slightly change its volume to accommodate for the increase in size of silicon crystal. This in turn will lower the stress in the core [23].

doi:10.6342/NTU202204042

1.2.3 Single Mode Coupling and Transmission in Multimode Fiber

Selective mode launching in MMF fiber has been investigated for mode division multiplexing. The butt coupling coefficient between two modes is shown in Eq. (1.1) [24]. From Eq. (1.1), for a mode, E_1 to be excited by another mode, E_2 with high efficiency, they must have similar mode field diameter, intensity distribution and large overlap area.

$$\eta = \frac{\left|\int E_1^* E_2 \, dA\right|^2}{\int |E_1|^2 \, dA \int |E_2|^2 \, dA} \tag{1.1}$$

Based on the criteria above, single mode coupling between SMF and MMF has been investigate. One of the methods is central launching method, MMF and SMF are placed so that the central axis of both fiber overlaps, this is to increase overlap region between both fundamental modes of SMF and MMF [25]. However, there is still a difference in mode field diameter of the fundamental modes in SMF and MMF. A method to modify the mode field diameter of SMF is to increase heating time of SMF during splicing so that germanium in SMF core can diffuse out the core increasing the effective core area and mode field diameter [26]. For coupling between fibers with large difference in MFD, a lens is used to modify the mode size between the fiber [7].

After fundamental mode is excited in MMF, without huge bending or change in geometry of the fiber, single mode transmission can be maintained for long distance [27]. Single mode transmission is proved to be able to generate non-linear effects in semiconductor fiber.

doi:10.6342/NTU202204042

1.2.4 Waveguide Based Refractive Index Sensor

Waveguide based refractive index optical sensor can be categorized into two main categories which is resonator based and coupling based. In a resonator based optical sensor, the sensing element's does not guide light. However, its resonance frequency changes with the analyte's refractive index. The evanescent field from the waveguide is used to probe the sensing element and light energy at the resonance frequency from the waveguide is coupled to the sensing element. The loss in light energy to the sensing element manifest itself as local minimum in frequency response of the waveguide. Examples of such sensor including Localized Surface Plasmon Resonance (LSPR) sensors [28] and Whispering Gallery Mode (WGM) sensors [30]. For coupling based sensors, the sensing element itself is a waveguide that can guide light. The coupling strength for different frequency changes with the analyte's refractive index. The power in waveguide at frequency with largest coupling strength will coupled to the sensing element most efficiently and thus will show up as a local minimum in the frequency response. Examples for coupling based sensors include interferometer-based sensor [30], Surface Plasmon Resonance (SPR) sensors [31] Lossy Mode Resonance (LMR) sensors [32] and. Absorption based refractive index sensor generally shows lower sensitivity and lower Full Width Half Maximum (FWHM) while coupling based sensor shows high sensitivity with high FWHM, therefore both of them have similar Figure of Merit (FOM). Currently, the best refractive index sensor has sensitivity of around a few 10 000 nm/RIU achieved by waveguide based SPR sensor [33], fiber based LMR sensor [34]. The current record for FOM is at around 10 000 by some WGM sensors [35]. Waveguide sensors are particularly useful in sensing a very tiny amount of analyte, such as in microfluidic channel due to its small surface area [36]. It

doi:10.6342/NTU202204042

can be used in label free detection method such as gas and chemical sensor [37] and or label free detection with for biosensing [36].

1.3 Organization of the Thesis

Chapter 2 describes the process of finding reasons and solution for low quality and low yield production of SCF through data analysis and mock experiments. In this chapter, a new method for SCF drawing is proposed and the design and fabrication of automated equipment to aid in the new process is explained. A thermal modelling of the fiber drawing furnace is carried out to understand the effect of different furnace parameters on the preform temperature distribution.

Chapter 3 describes the investigation of parameters that effects the temperature distribution during the CO2 laser annealing process of SCF using thermal modelling and experiment. The feasibility of single mode coupling and transmission in SCF is also investigated. A mode decomposition algorithm is also written to distinguish amplitude of modes in multimode fiber.

Chapter 4 establishes guidelines for designing high performance coupled waveguide sensors using analytical and numerical analysis and the results are verify with optical simulation.

doi:10.6342/NTU202204042

Chapter 2 Fiber Drawing

2.1 Introduction

In 2016, SCF was first fabricated in our lab using powder-in-tube method. A non-commercial furnace was used and the fibers was manually drawn (hand drawn) instead of automated drawing. This method is suitable for doing proof of concepts but is not suitable for producing SCF with precise geometry and with high consistency. Both conditions are a must if we want to further develop our SCF into sensors and for other uses. During this process, we also encounter a major problem which is a super low success rate for producing long continues length of SCF. Therefore, in this chapter, we will try to understand the root of this problem and find possible solutions around it. A new drawing process is proposed and automated equipment to realize this process is installed.

2.2 Fiber Drawing Equipment

A commercial optical fiber drawing tower is made up of a furnace system, a preform feeding system, a fiber drawing system, tension sensors, diameter gauges, chemical coating devices and a central control system [38]. Most of these drawing towers are fully automated. In our lab, the drawing tower previously used only includes a furnace system and a preform feeding system (Fig 2-1). Functions of the other parts found on commercial fiber drawing towers was performed manually instead. Our drawing tower stands at about 3 meters tall from ground level to the bottom of the furnace.

doi:10.6342/NTU202204042

2.2.1 Furnace System

The furnace system in our lab is a resistive heating furnace produced locally (Fig. 2-1). It uses a graphite heater as heating element. The graphite heating element is connected to the electrical power supply system through copper electrodes. Surrounding the graphite heater is a thick layer of graphite felt insulator that traps the heat inside the furnace and also isolates the user from the high temperature inside the furnace. Inside the graphene heating element is a center graphite tube that prevents the preform from directly touching the graphite heating element (Fig. 2-2(c)-(d)). This center tube also acts as a cap to prevent nitrogen gas from flowing too rapidly out of the furnace. Below the graphite heating element is another graphite insulation tube that extends out the furnace. It ensures that the temperature gradient of the preform from the hottest part to the surrounding is mild so that the fiber does not experience temperature shock that can cause cracks and fractures. An open loop water-cooling system is used to keep the outer shell of the furnace at room temperature. An inflow and outflow volume monitor and a temperature gauge are used to ensure. N^2 gas is flow constantly into the furnace to prevent oxidation of the graphite heater.

The electrical supply system that powers our furnace converts 220V AC to low voltage high current AC. The AC input power is controlled using a thyristor power regulator with feedback system (Caho model 1206) before converted to high current AC output through a huge transformer (Fig. 2-3(a)-(b)). Temperature is measured using a thermocouple and the reading is used in a feedback loop to prevent huge fluctuation in temperature. The measured temperature and target temperature are displayed on the front of the controller. The whole furnace system takes approximately 1.5 hours to reach 1640°C from cold start.

doi:10.6342/NTU202204042

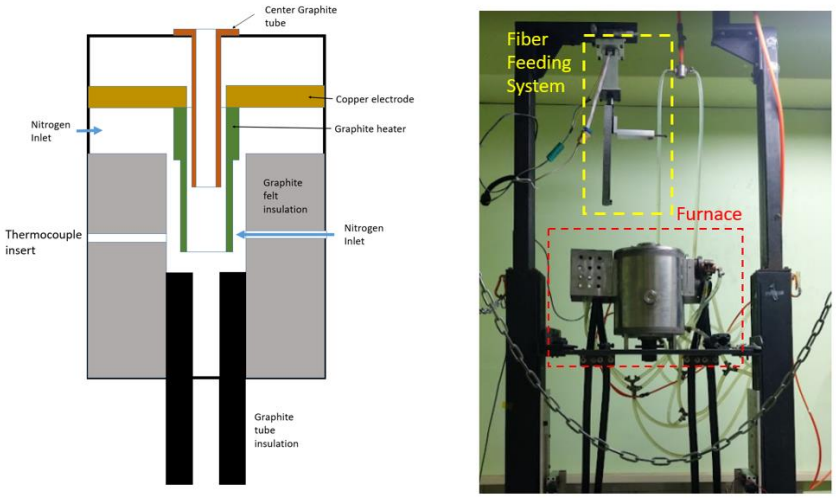

Fig. 2-1 (Left) Drawing of inner components of a furnace system (Right) SCF Drawing Tower

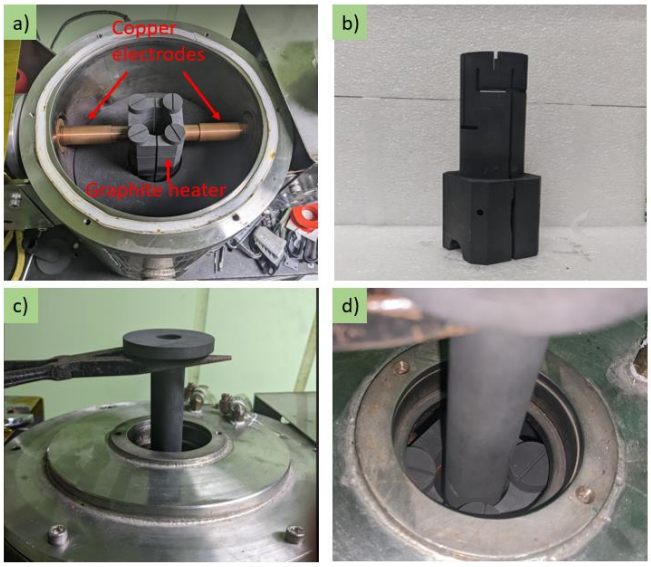

Fig. 2-2 (a) Inside of furnace (b) Graphite heating element (c) Center graphite tube (d) Center graphite tube sits inside the graphite heating element

doi:10.6342/NTU202204042

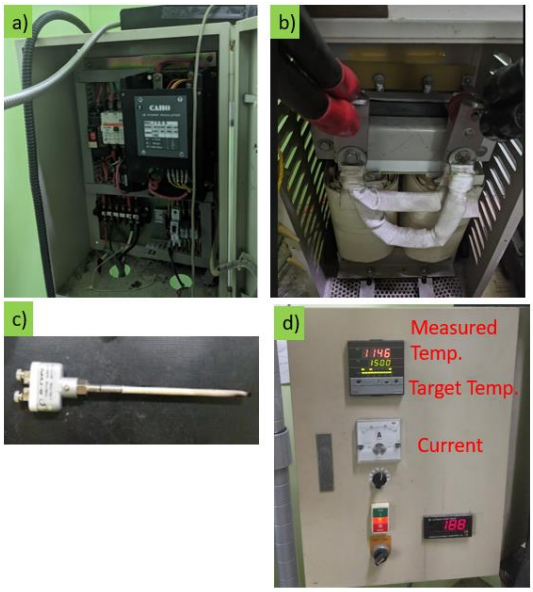

Fig. 2-3: (a) Electrical supply system (b) Transformer (c) Thermocouple (d) Control panel

2.2.2 Preform Feeding System.

The preform feeding system on our drawing tower is consisted of a linear stage and a stepper motor (Fig 2-4b). The stepper motor is controlled by using voltage input as signal. The feeding speed is controlled manually and all knobs can be found on a control panel (Fig 2-4a).

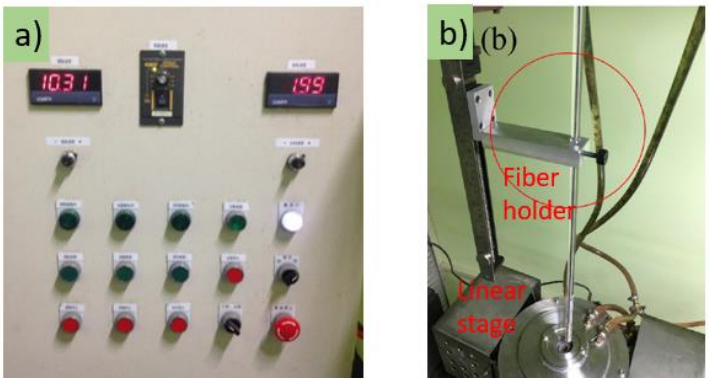

Fig. 2-4 (a) Old control panel for preform feeding system (b) Old preform feeding system's preform holder and linear stage

doi:10.6342/NTU202204042

2.3 Fiber Drawing Process

2.3.1 Preform

In our lab, our furnace has an opening of diameter around 18 mm and therefore the glass preforms used cannot have an overall outer diameter exceeding 15 mm for safety purpose. Our glass preforms were made up of an outer glass hollow tube with outer diameter 10mm and inner diameter 5mm. Another inner glass hollow tube with outer diameter 5mm and inner diameter 3mm is filled with silicon powder and then sleeved into the outer tube to form a glass preform with 10mm overall diameter and 3mm diameter silicon powder core similar to that reported by Ballato's group [14].

2.3.2 Drawing Procedure

When the furnace has reached a preset temperature, usually between 1630 °C to 1660 °C, the preform is inserted into the furnace from the top and clamped with the fiber holder (Fig. 2-5a). The preform is held still for preheating for usually 30 s before the preform feeding system is started. The preform is set to move at a constant speed of between 0.01 mm/s to 0.05 mm/s. As the preform heats up, the hottest part of the preform softens forming a neck. The weight of the preform below the neck is pulled by gravity and move downwards (Fig. 2-5b). As the neck region thins and elongates, the process speeds up. When the lower part of the preform has fallen out of the preform, it is cut off from the thin strain of glass fiber where it is hanged from (Fig. 2-5c). Now by pulling on the glass strain, the drawing process is continued (Fig. 2-5d).

doi:10.6342/NTU202204042

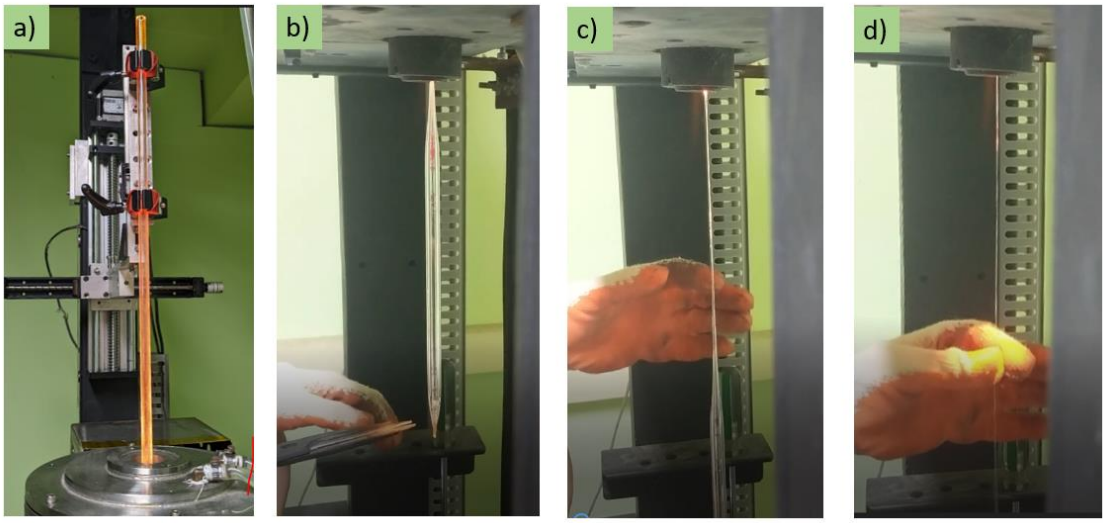

Fig 2-5 (a) Preform inserted into the furnace from the top and clamped with the fiber holder (b) Preform below the neck pulled by gravity and move downwards (c) Thin strain of fiber holding the preform (d) Fiber drawn by hand

2.3.3 Parameters and Data Collection

The whole drawing process can be divided into two parts, the process before hand-drawing starts and the process after it. This division is made because the first part of the process has minimal influenced by human factors. All outcomes will therefore be largely determined by initial conditions. The initial conditions are the parameters we manipulate. The second part of the process is harder to quantify as it is hard to maintain constant input with human intervention. We would therefore assume that if the initial conditions of the first part of the process is set correctly, successful outcome in the second part of the process would be guaranteed. In other words, the outcome for the second part of the process is only determined by conditions in the first part of the drawing process. The success of initial conditions in turn is judged by the outcome of the second process.

doi:10.6342/NTU202204042

The parameters that would influence fiber drawing process are those that affect the temperature distribution and fluid dynamics of the preform. Literature on normal glass fiber drawing has pointed out that peak temperature of the furnace, temperature distribution in the furnace and feeding speed would influence the temperature distribution of the preform [39]. Together with drawing and feeding speed, these factors would affect the neck shape and geometry of the fiber [40-41]. Therefore, in our experiment, these factors are explored to try and improve the quality and yield of SCF.

In our set-up, two parameters that we choose to manipulate is the furnace temperature, or the temperature measured by the thermocouple, T and the feeding speed, V_{feed}. The temperature distribution of the furnace is a function of the material and geometry of the furnace and therefore a constant. (We will explore more of this in the section on the thermal modelling of the furnace.) The drawing speed in the first part of the drawing process is dictated by the weight preform section below the neck. This can be kept constant for specific values of measured temperature and feeding speed by making sure the position of the preform relative to furnace is kept constant. Preheat time of all experiments is also kept constant at 30 s.

The three outcomes which we think can give us insight into the drawing process is the falling time, t_{fall}, presence of silicon flow, Fl and success in producing SCF, S. Falling time is the time taken for the preform to fall out a certain distance relative to the bottom of the furnace. This parameter will likely reflect the temperature distribution and peak temperature of the preform. Another parameter is the presence of silicon flow in the tail of the fallen preform regardless of its continuity (Fig. 2-6). This outcome was recorded because we observed it might have correlation with successful producing SCF. Lastly, the most important outcome is the successful in producing SCF. This is defined by the ability during the hand drawing part of the process to draw at least 10cm of SCF

doi:10.6342/NTU202204042

with continues core. The core also must not have bulge or crack to be considered a successful draw.

Independent Variables	Dependent Variables
Furnace Temperature, T	Falling Time, t_{fall}
Feeding Speed, V_{feed}	Presence of silicon flow, Fl
	Successfully producing SCF, S

Table 2-1 List of independent and dependent variables during fiber drawing

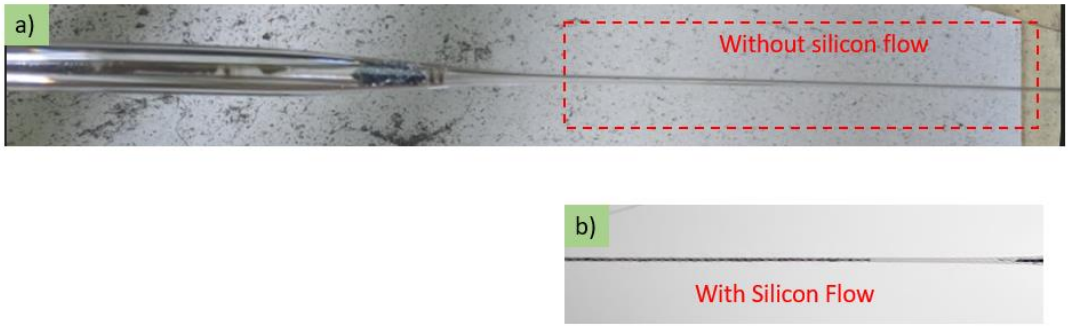

Fig. 2-6 Tail of the preform (a) without silicon flow (b) with silicon flow although not continues

doi:10.6342/NTU202204042

2.4 Data analysis

The variables in the data sets we are analyzing are those listed in Table 2-1: $T, V_{feed}, t_{fall}, Fl$ and S. Fl and S are binary outcomes while T, V_{feed}, t_{fall} are continues value. All of the data are from the optical fiber drawing experiments our lab's teammate conducted between 2017 and 2021. They are categorized into 4 sets, {Wei&Yong, Kai&Yang, CP&Paul_1, CP&Paul_2}. The sets are divided according to the personal doing the experiments, period in which the data was collected, range of the parameters and condition of the furnace. The data sets {Wei&Yong, Kai&Yang, CP&Paul_1, CP&Paul_2} between 2017 to 2018, 2018 to 2020, 2020 to 2021 and 2021 respectively. Between the period where the two sets of data, {CP&Paul_1, CP&Paul_2} were collected, the inner parts of the furnace were changed including a new graphite insulation felt and a new center graphite tube (Fig. 2-8) after a series of breakdown. We suspect that the temperature distribution in furnace fluctuates greatly as will be discussed later in this section. Not all parameters in Table 2-1 are collected across all data sets. Wei&Yong set does not have data on Fl, Kai&Yang set does not have data on S.

2.4.1 Success Rate

The success rate is defined by the number of events where S =1 to the total number of events in each data set. The overall success rate in these periods are listed in Table 2-2. Previously, we thought that the success of drawing SCF in our experiment set-up depends on only the two parameters T and V_{feed}. To see if the hypothesis holds true, a logistic regression analysis using a linear and a quadratic model with S as dependent variable and T, V_{feed} as independent variables was conducted. A quadratic

doi:10.6342/NTU202204042

model is provided together with a linear model as we want to account for non-linearity between T, V_{feed} and S =1 if such relationship exists. From both the analysis, we see that none of the p-values for each independent variable in all data sets have value smaller than 0.05 (95% confidence). Therefore, we do not have enough statistical significance to conclude that T, V_{feed} can affect the outcome of S (Table 2-3).

Data set	$\frac{\text{Number of events where S } = 1}{\text{Total number of events}}$	Success rate
Wei&Yong	$\frac{59}{147}$	0.401
CP&Paul_1	$\frac{13}{50}$	0.26
CP&Paul_2	$\frac{11}{22}$	0.5

Table 2-2 Success rate for each data sets

To find the reasons for such low success rate as seen from Table 2-2, we try to see if there are other outcomes that has correlation with the success rate. One observation we can see is that the success rate greatly increased if when $Fl = 1$ (Table 2-4). As data of Fl was not included in Wei&Yong and Kai&Yang data sets, only the results from the two other data sets are given below. Using a logistic regression to analyze the relationship between Fl and S, we prove that our observation is statistically true as the P-value for both data sets are way smaller than 0.05.

Seeing that FL can influence the outcome of fiber drawing, a logistic regression with is done with independent T, V_{feed} . Again, the P-values are above 0.05 and therefore there is no evidence that Fl is influence by $T$and V_{feed}.

doi:10.6342/NTU202204042

Data Sets	Linear model: Dependent Variable, S		Quadratic model: Dependent Variable, S	
	Independent Variable	P-value	Independent Variable	P-value
Wei&Yong	V_{feed}	0.462	V_{feed}	0.700
			${V_{feed}}^2$	0.803
	T	0.182	T	0.263
			T^2	0.261
CP&Paul_1	V_{feed}	0.505	V_{feed}	0.0976
			${V_{feed}}^2$	0.093
	T	0.063	T	0.446
			T^2	0.451
CP&Paul_2	V_{feed}	0.781	V_{feed}	0.996
			${V_{feed}}^2$	0.996
	T	0.783	T	0.947
			T^2	0.947

Table 2-3 Outcome from linear and quadratic mode

Data sets	Success Rate		Logistic regression (Linear model): Dependent Variable, S, Independent Variables, Fl	
	$Fl = 0$	$Fl = 1$	Coefficient	P-value
CP&Paul_1	0.12	0.48	1.992	0.007
CP&Paul_2	0.14	0.79	0.643	0.003

Table 2-4 Correlation between success rate of and Fl proven using logistic regression model

doi:10.6342/NTU202204042

2.4.2 Temperature Inconsistency in Furnace

The falling time of the preform $t_{fall}$was thought to reflect the temperature distribution inside the furnace. If the overall temperature of the furnace is higher, the glass will have higher temperature and this results in the preform having lower viscosity (Fig. 2-7). With lower viscosity, the glass will deform quicker forming a neck shape and when the silica strand is pulled from the neck, it flows faster. Both of this factor contributes to a lower t_{fall}. The feeding speed of the preform,V_{feed} will lower the peak temperature but widens the temperature distribution curve [41]. These effects on t_{fall} is not so evident though. However, if V_{feed} is kept constant, increasing T cause a decrease in t_{fall}. If this monotonic relationship is not seen, there may be a difference between T and the actual temperature distribution in the furnace. This is also the case in our experiments where the monotonic relation is not seen between data sets and within some data sets as well. Fig. 2-8 shows data of t_{fall} against T plot at $V_{feed} = 0.03\frac{mm}{s}$ from both CP&Paul_1 and CP&Paul_2 datasets. Within the data set of CP&Paul_1, a monotonically decreasing relationship can be seen but the data from CP&Paul_2 does not fit into this relationship. Fig. 2-9 shows data of the t_{fall} against T plot at $V_{feed} = 0.05\frac{mm}{s}$ from CP&Paul_1 and Kai&Yang datasets. Both data sets show monotonically decreasing relationship and numerical wise, they seem close enough to come from a same set. Fig 2-10 shows data of t_{fall} against T plot at $V_{feed} = 0.1\frac{mm}{s}$ from Wei&Yong data set. It shows a slightly increasing relationship between t_{fall} and T and a very big deviation between data point. From these 3 figures, we can only deduce that the measured temperature, T does not show consistency with the real temperature distribution of the preform or furnace. The inner parts of the furnace were refurbished in between the period the two data sets CP&Paul_1and CP&Paul_2 was collected. We also

doi:10.6342/NTU202204042

frequently dissemble our furnace for maintenance and the personnel doing this job differ between data sets. The temperature inconsistency we see from the data analysis might be caused by these factors.

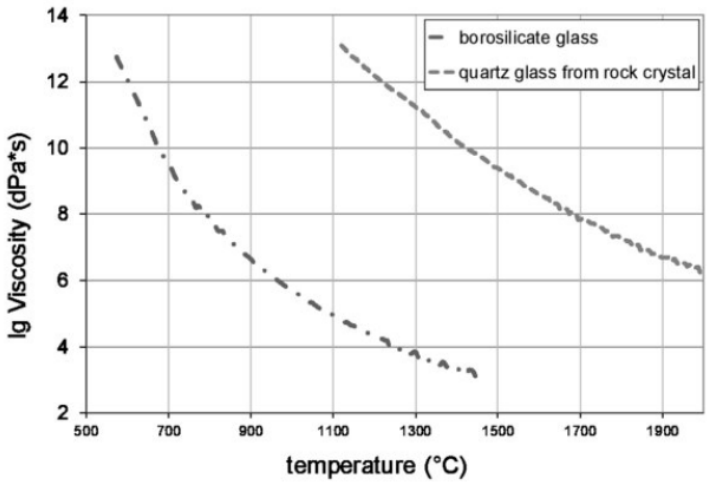

Fig. 2-7 Viscosity of glass decreases as temperature increases

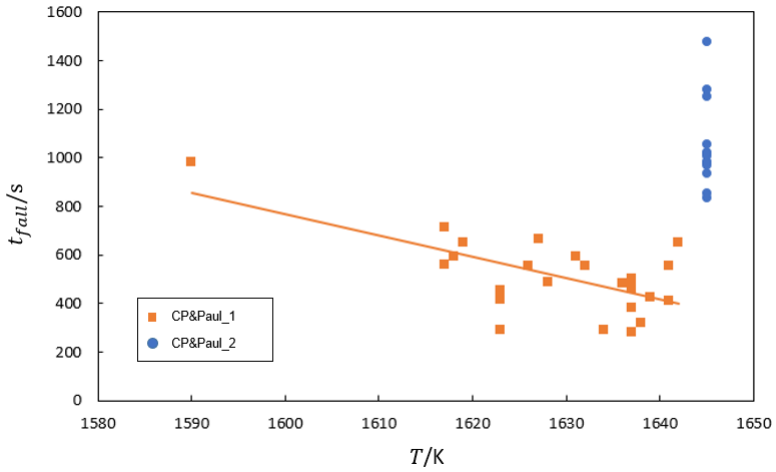

Fig 2-8: t_{fall} against T at $V_{feed} = 0.03\,\frac{mm}{s}$ for CP&Paul_1 (Orange) and CP&Paul_2 (Blue) data set

doi:10.6342/NTU202204042

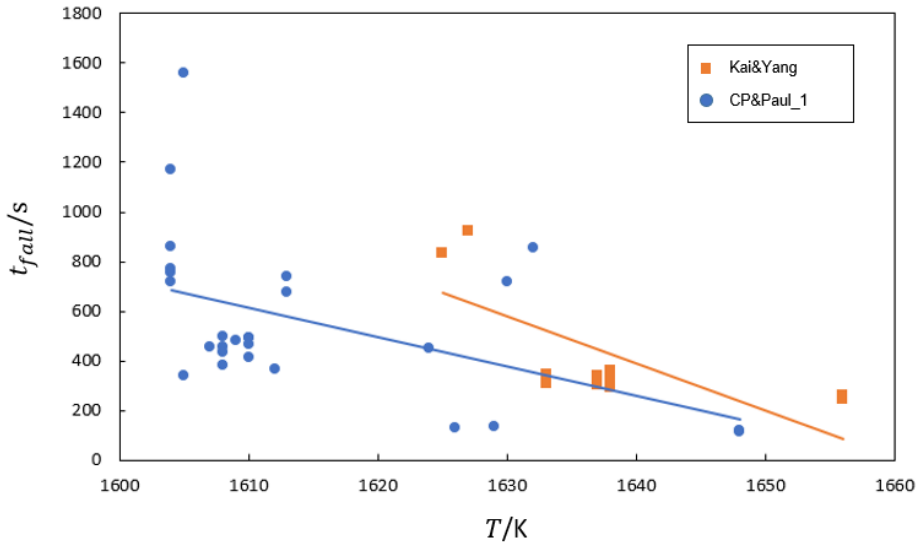

Fig 2-9: t_{fall} against T at $V_{feed} = 0.05\frac{mm}{s}$ for Kai&Yang(Orange) and CP&Paul1 (Blue) data set

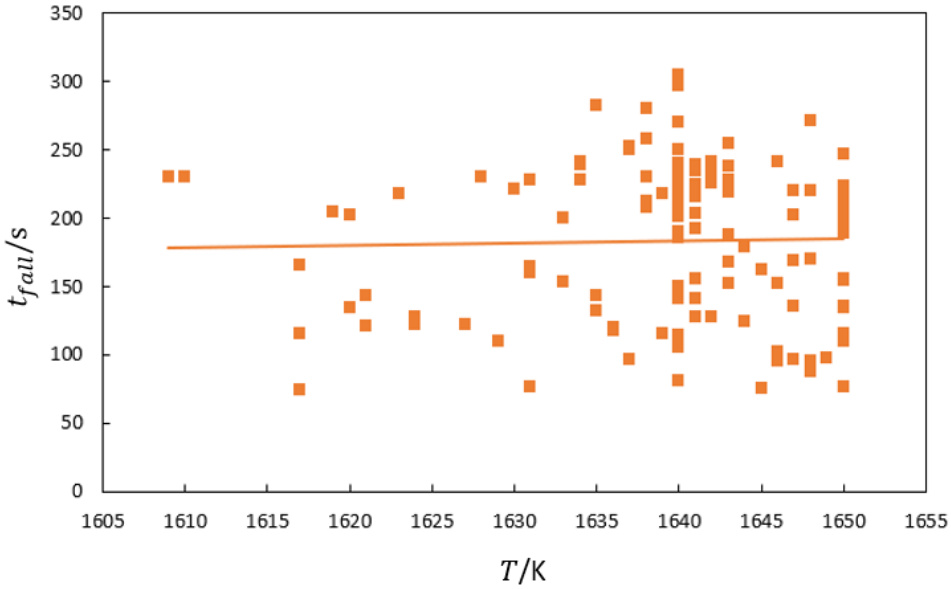

Fig 2-10: t_{fall} against T at $V_{feed} = 0.1\frac{mm}{s}$ for Wei&Yong data set

doi:10.6342/NTU202204042

2.4.3 Conclusion

From the data analysis, we see that the success to draw fiber, $S = 1$ has no statistically significant relationship with T and V_{feed}. This may or may not be due to the real temperature fluctuation that we infer from the day to day fluctuation of t_{fall}. However, we did observe that for all T and V_{feed}, success rate when $Fl = 1$ is way higher than $Fl = 0$ and we prove that this statement is statistically true. However, statistical analysis also shows that Fl was not affected by T and V_{feed}. Therefore, we need to investigate the real reason for the outcome of Fl and try to increase the chance of $Fl = 1$. In the meantime, we also observed temperature inconsistency between measured and real data. To understand factors contributing to this inconsistency, a thermal modeling of the furnace with COMSOL Multiphysics is carried out and the results will be discussed in section 2.6.

doi:10.6342/NTU202204042

2.5 Air bubble

Upon inspection, we see that if there is no flow of silicon at the tail of preform, $Fl = 0$ there is always a void at the neck of the preform. Voids were also observed in the region just above and below the preform neck. Such a phenomenon was also observed previously but we thought that as the viscosity of silicon is so low, it can flow into the neck of preform given that the neck of the preform has the highest temperature compared other part of the preform. To test this assumption, we decided to further investigate the phenomenon of melting and flowing of silicon powder in a narrow tube. As we cannot see into the furnace and we do not have heat source besides the furnace that is powerful enough to melt silicon powder inside the preform tube, the melting process cannot be directly observed. To emulate the same type of phenomenon at lower temperature so we can observe it outside the furnace, experiment with powdered substance with lower melting point is carried out.

2.5.1 Melting of Solder Powder in Glass Preform

Solder powder which is a mix of 60% tin, Sn and 40% lead is chosen as silicon powder substitute due to its low melting point. We fill an inner tube of preform with an outer diameter of 5mm and an inner diameter of 3mm with the solder powder and use Butane gas burner heat the preform producing a high heat zone. The images of the experiment are shown in shown in Fig. 2-11 in chronology order.

In the beginning, the solder powder at the region with peak temperature starts to melt and starts to clump together (Fig. 2-11(a)-(b)). The clump stays at its original position and it starts to grow with the inflow of newly melted solder powder from region further away from the peak temperature line (Fig. 2-11(c)). As the clump fills up

doi:10.6342/NTU202204042

the entire inner diameter of the tube, it starts to move upwards pushed by expanding air below (Fig. 2-11(d)). The air expands due to heating. As the temperature around the tube continue to increase, the solder powder below the peak temperature line starts to melt and form a clump as well. When the clump fills up the entire diameter of the tube, an air pocket is trap between the two clumps of solder below and above the peak temperature line. The air pocket continues to expand and both clumps are pushed further away. From this experiment, we can make a hypothesis about the silicon melt in our preform. The position of peak temperature line would be where the neck region of preform is. Similar to the solder melt, silicon melt might form clumps and the air in the neck region would push the silicon clumps away from the neck forming a void.

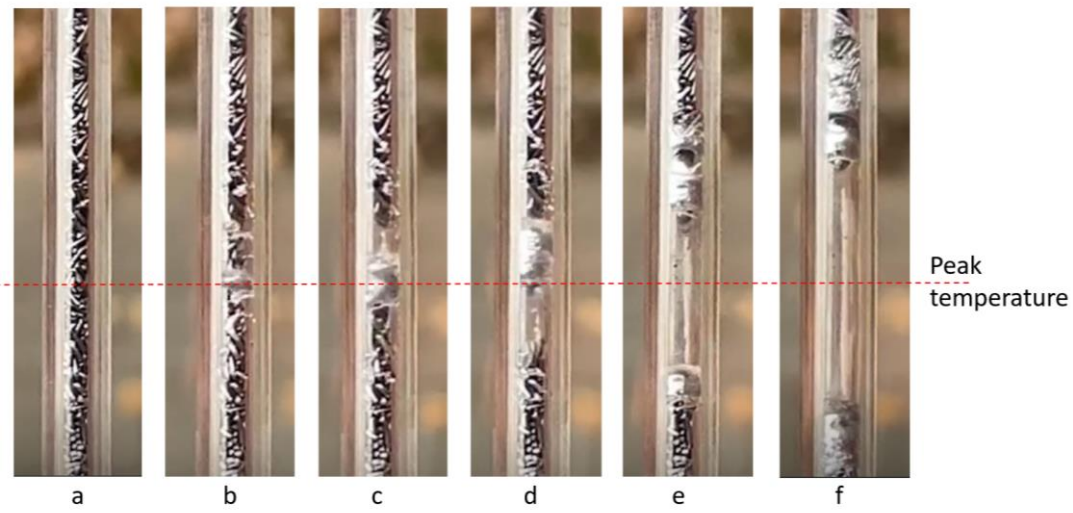

Fig. 2-11 Melting process of solder powder in narrow tube (3mm inner diameter) according to chronology

The same experiment is repeated with two other glass tubes with inner diameter of 5mm and 7mm respectively. The 5mm inner diameter tube shows not much difference from the 3mm inner diameter tube. However, the 7mm tube shows promising result as the molten solder can flow down and fill up the hottest part of the tube. The

doi:10.6342/NTU202204042

image from the experiment is shown in Fig. 2-12. At the beginning, clump forms as the solder powder melts (Fig. 2-12(a)-(c)). However, before the clump can fill up the diameter of the inner tube, it flows downwards (Fig. 2-12(d)). As the tube is heated continuously, solder powder further away from peak temperature region melts and flow down (Fig. 2-12(e)). During this process, no large air pocket was trap in pool of molten solder. As more solder below the peak temperature region is melted as well, we can see small air bubbles rising between the tube wall and molten solder pool thus no air pocket is trapped (Fig. 2-12(f)).

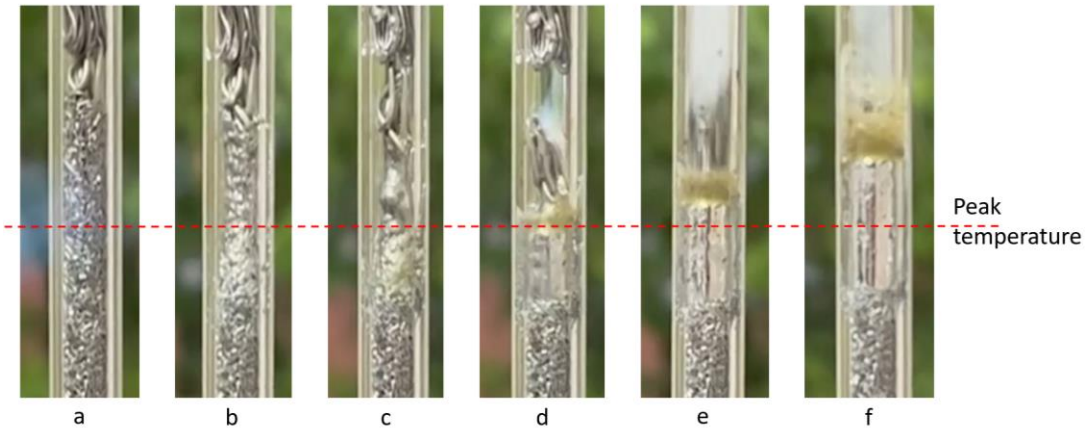

Fig. 2-12 Melting process of solder powder in wide tube (7mm inner diameter) according to chronology

From observation, it seems that the melting of powder in a tube can be separated into two stage. In the first stage, the powder melts and agglomerates together with air between the powder particles flowing to both the top and bottom of the molten pool. As more powder melts, the molten pool becomes large enough to span the diameter of the whole tube, forming a Taylor bubble (Fig 2-13(a)-(b)). (Taylor bubble is a type of bubble which flow in a vertical tube and occupy almost the entire cross section of the tube.) If the Taylor bubble can flow past the molten clump, the molten pool will drop

doi:10.6342/NTU202204042

and come in contact with the unmelt powder below (Fig 2-13(c1)). However, if the Taylor bubble does not flow past the molten pool, it will be trapped between the molten pool and unmelt powder below (Fig 2-13(c2)). The key for the molten clump to flow downwards depends on the Taylor's bubble rising velocity. According to Bretherton [42], the Taylor's bubble rising velocity reached approaches zero when the tube diameter the bubble is in approaches a critical radius R_c:

$$R_c = 0.918\sqrt{\frac{\gamma}{\rho g}} \tag{2.1}$$

where γ is the surface tension of the liquid and gas in the bubble, ρ is the density of the liquid and g is the gravity acceleration. If the rising velocity is near zero, it will appear as the bubble is trapped in the tube.

In the second stage of the powder melting experiment, there are two cases to be considered depending on the radius of the tube, R. For $R > R_c$, as new powder below the molten pool melts, smaller air bubbles are formed and can flow past the molten pool before reaching the Taylor bubble. As the upper powder melts, the Taylor bubble can also flow past the newly melt powder and there will be no air bubble trapped between the molten pool (Fig. 2-13(d1)-(e1)). For $R < R_c$, as powder below the bubble melts and air between the powder flows into the trapped Taylor bubble. The Taylor bubble expands due to the influx of new gas particles and also the expansion pushing the molten clump above further up the tube. A large air pocket separates the molten pool into two sections (Fig. 2-13(d2)-(e2)).

The R_c for both molten solder and silicon is calculated (Table 2-5). For molten solder, the experiment agrees with the calculation as for tube diameter below 7 mm (radius 3.5 mm), the rising velocity of Taylor bubble is still too slow to be observed to

doi:10.6342/NTU202204042

flow past the molten pool. Next, a similar experiment is performed with silicon to see if the same phenomenon holds true for silicon as well.

Material	γ / N m^{-1}	ρ / Kg m^3	R_c/mm
Solder (SN60Pb40)	0.42	8400	2.0
Silicon	0.7	2530	4.9

Table 2-5 Fluid parameters for molten solder and silicon [43-44]

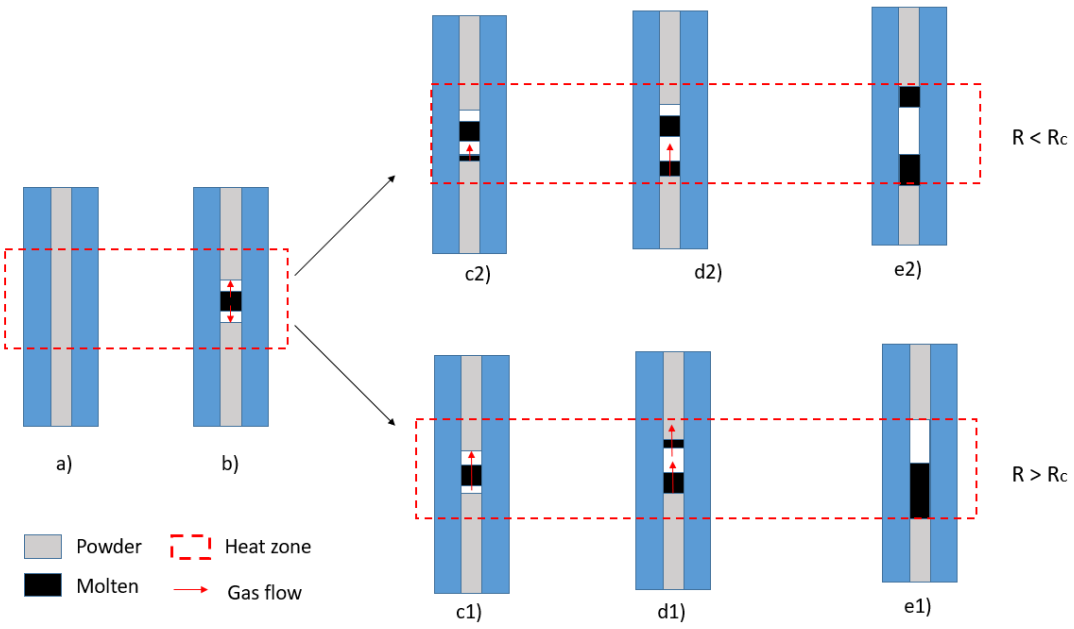

Fig. 2-13 Flow of molten pool tube with diameter above and below critical radius.

2.5.2 Melting of Silicon Powder in Glass Preform

With powder-in-tube method, it seems that the formation of air bubbles is inevitable as the fill factor of Si powder ranging from 20-30 mesh averages at about 0.6 (comparing the weight of same volume of powder silicon to bulk silicon). We would infer that air bubble will be trapped at the hottest region of the preform during heating

doi:10.6342/NTU202204042

as the Taylor bubble cannot flow upwards in our 2 mm inner diameter (1 mm radius) preform. The critical radius for Taylor bubbles in silicon fluid is calculated to be 4.9 mm. To test for our inference, silicon powder is melted inside the glass preform with inner diameter of 2 mm and 7mm while still preserving the geometry of the preform to make sure that the experiment is not affected by neck forming process. Our drawing furnace is used as a heat source at a lower temperature that melts the silicon powder but does not soften the glass preform which occurs at measured temperature of around 1200 °C. From this, we know that the temperature measured by thermocouple differ is lower than the actual maximum preform temperature by about 200 °C. The preform with filled silicon powder is inserted into the furnace and placed in the furnace for 900 s for the preform to reach steady state temperature and for the silicon to melt. After that, the furnace temperature is slightly lowered for the silicon to slowly solidifies before taking out from the furnace. This is to prevent rapid change of temperature in molten silicon where a quick change in phase will crack the glass preform.

With the 2mm preform, a void can be seen between the two section of silicon (Fig. 2-14(a)). To make sure that the void occurs at the hottest point where the position of the neck would be, we use a higher temperature of 1600 °C for the preform to slightly deform and form a slight indent to mark the position of the neck. When the length of the region with temperature high enough to melt silicon increases, silicon along the preform forms a few clusters with air pocket between them. However, we can see that largest void is still the position near the neck of the preform (Fig. 2-14(b)). With more silicon cluster, the flow of molten silicon would be slightly different from the process in Fig. 2-14 (c2)-(e2). There would be more possibility for cluster to form at the neck hence we sometimes can still successfully draw SCF.

doi:10.6342/NTU202204042

Although the critical radius is calculated at 4.9 mm (diameter 9.8 mm), we still tested preform with inner diameter of 6 mm first because we need to modify our furnace for tube with inner diameter of 9.8 mm to fit in. A higher temperature of 1600 °C is used to melt the silicon because we want to observe the formation of multiple silicon cluster. Most of the silicon molten actually flow to the bottom melt region (Fig. 2-15(a)). However, the newly melted silicon at the top takes a long time of 2 hours to flow down (Fig. 2-15(b)) which means the rising velocity of the Taylor bubble is still very slow. The initial molten silicon can flow down because Bretherton's critical radius only holds true for laminar flow assumption [45]. At the start of the melting process, the melting is still at a transient state, the flow of molten is probably more turbulent especially for larger tube [46]. By breaking the silicon cluster, we can see that some small air bubbles inside. This will not cause large void at the neck of the preform but would probably affect the quality of SCF. Further investigation to completely eliminate them needed to be done (Fig. 2-16).

Both of this experiment is too simple and incomplete to fully the characterized the flow of melting powder in the tube, which itself is very complex and not explored in literature yet. However, we can still conclude that tube diameter directly influences the flow and distribution of air bubble in the molten zone.

doi:10.6342/NTU202204042

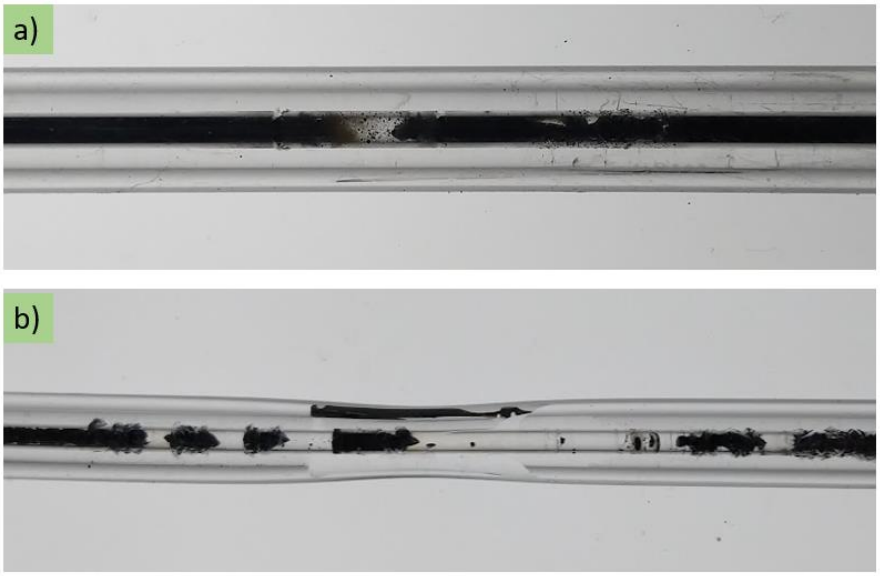

Fig. 2-14 Silicon powder heated in preform at (a) 1200 °C (b) 1600 °C

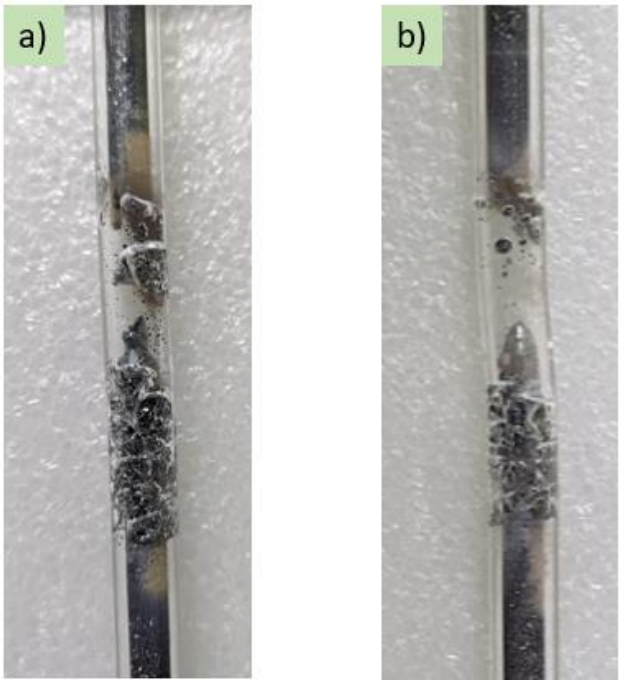

Fig. 2-15 Silicon powder in preform with large diameter. Heating time (a) 30 min (b) 120 min

doi:10.6342/NTU202204042

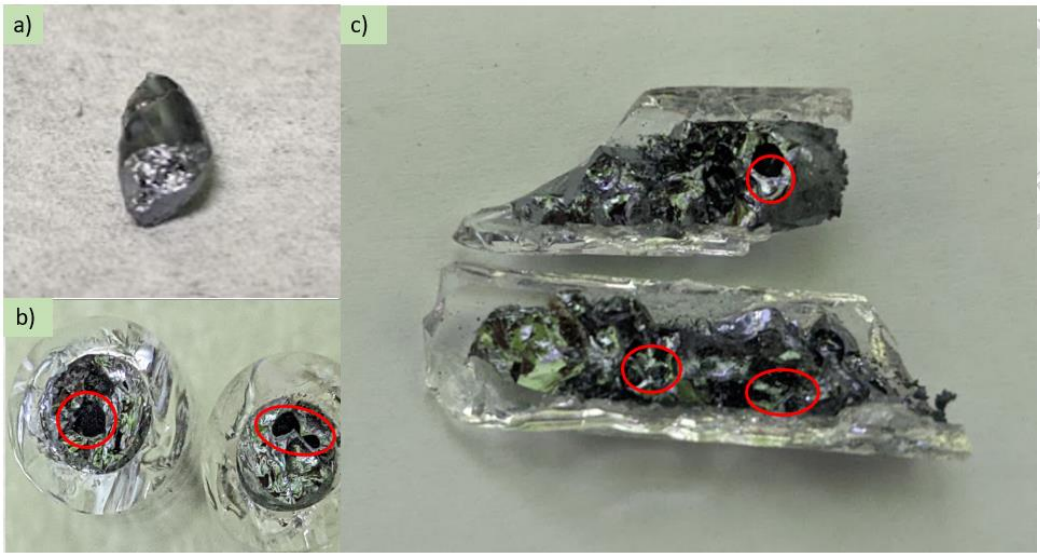

Fig. 2-16 (a) Silicon powder solidifies into chunk (b)-(c) Small air bubbles still exist in silicon chunk

doi:10.6342/NTU202204042

2.6 New Optical Fiber Drawing Process and Equipment

2.6.1 Automated Fiber Drawing System

The core and cladding diameter of the SCF is dictated by many factors, including the drawing speed and feeding speed d, the temperature distribution of the preform, the outer and inner diameter of the preform and the material of the core and cladding [41]. As our SCF drawing process was manually done, we cannot control the core and cladding diameter of the SCF because it is not possible to control and maintain the drawing speed during the fiber drawing process with hands. There are numerous reasons for precisely controlling the fiber geometry:

1. Matching the cladding diameter of our SCF to the cladding diameter of standard fiber (125 μm) so SCF is compatibility with standard fiber processing equipment such as splicer and holder to ensure good quality of splicing between SCF and standard glass fiber.
2. Matching the mode size of the fundamental mode in SCF to the single mode in SMF for single mode transmission in SCF.
3. Controlling the effective index of modes in SCF in the design of fiber sensor

Therefore, it is essential for us to have an automated drawing system. Using this system, we can also explore the possibilities that we can increase the success rate regardless of the outcome of Fl.

Fig. 2-17 is a commercially used fiber drawing system. This type of drawing system usually consists of an automated wheel that spools the fiber (Spooling wheel). It also acts as a drawing mechanism (Fig. 2-17). However, such drawing mechanism is not suitable for our application because SCF could not be wrapped around the spooling wheel without breaking at diameter around 20-30 μm. This is due to the SCF large

doi:10.6342/NTU202204042

bending radius and fragile nature. Therefore, we need an alternative drawing method which consist of two wheels clamping on the fiber, one wheel is motorized while the other is free spinning (Fig. 2-18). The motorized wheel provides drawing motion while the free spinning wheel provides tangential force acting on the fiber. This is to ensure that the friction force between the fiber and clamping wheels are large enough so that there is no slippage between the fiber and surface of the wheel. At this condition, the drawing speed is equal to the tangential speed of the wheel.

A geared brushless DC motor is used in our automated drawing system. The rotational speed of the motor is directly proportional to the voltage provided. With a drawing wheel of circumference of 200 mm diameter directly driven, the drawing speed versus the voltage is shown in Fig. 2-19. The motor with rated torque at 0.2 Nm can provide up to 6.6 N of drawing force through our drawing wheel. By measuring the weight of the preform that pulls the fiber in the initial stage of the drawing process and fall out of the furnace, we can calculate the maximum possible tension of the fiber in the later drawing process. The tension is calculated to be 0.25 N, 4% of the rated force of our automated system. The fluctuation in tension during the drawing process, using a conservative estimation of 25%, would be 1% of the rated output of the automated system, and is small enough to not cause significant rotating speed variation (Fig. 2-20).

doi:10.6342/NTU202204042

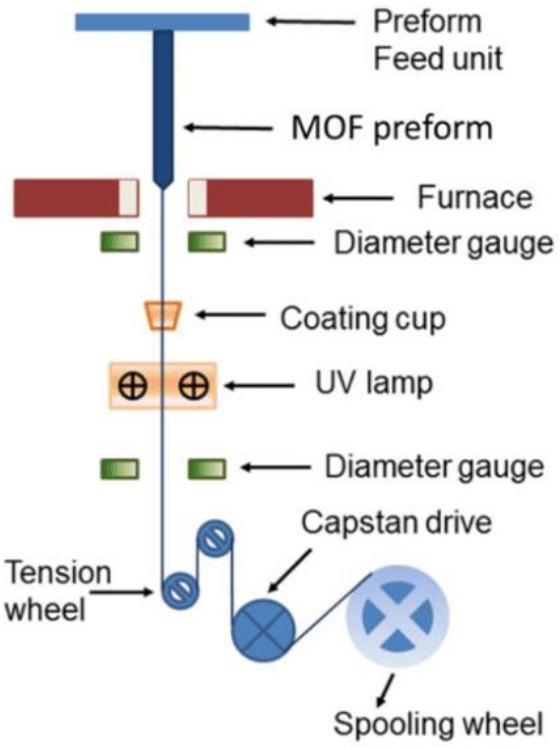

Fig. 2-17 Commercial drawing tower [28]

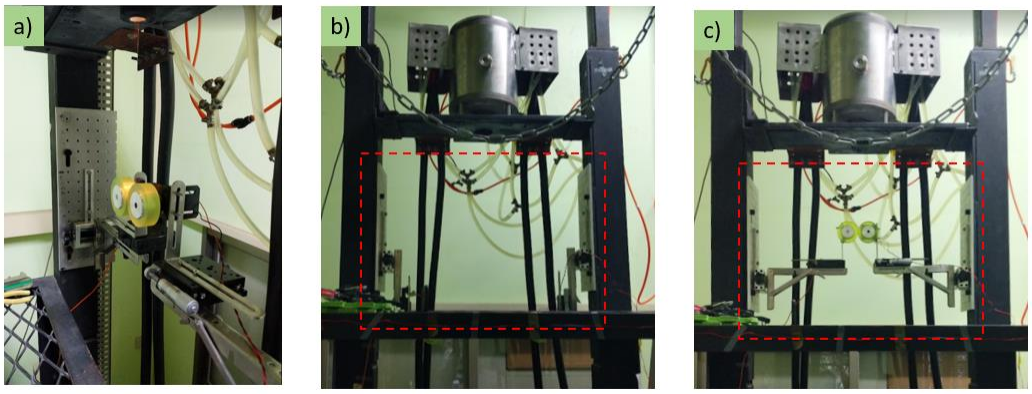

Fig. 2-18 (a) Drawing wheel (b) Drawing wheel retracted for preform to fall through (c) Drawing wheel employed

doi:10.6342/NTU202204042

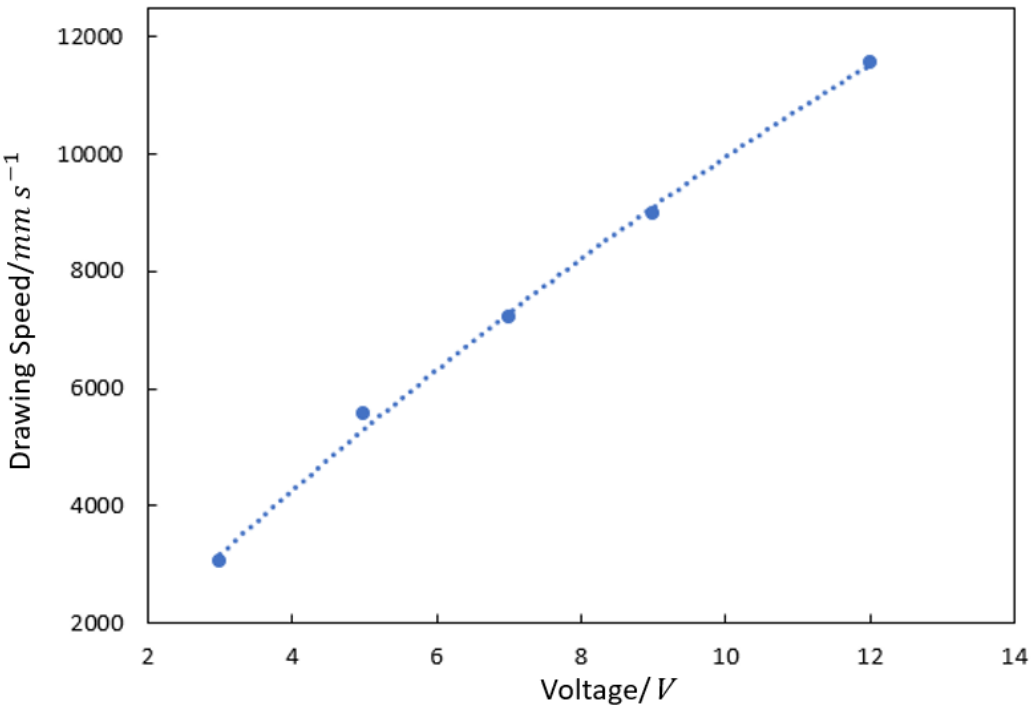

Fig. 2-19 Supplied voltage and drawing speed

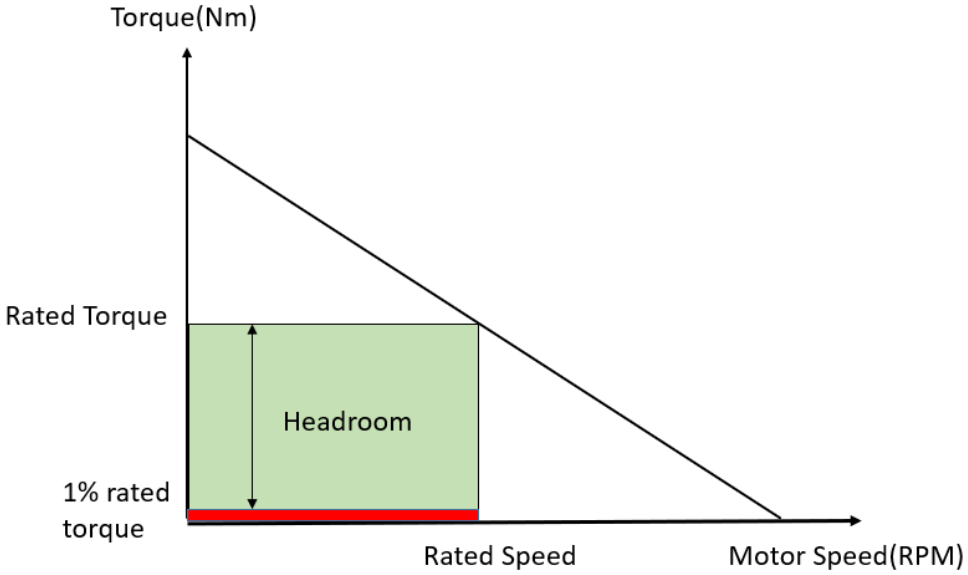

Fig. 2-20 Drawing tension vs rated torque of motor

The procedure for drawing fiber in this system is similar to that in section 2.2.1 just that the manual hand-drawn process is substitute by automated drawing by drawing wheel. At first, the drawing wheel is retracted to let the falling preform pass through

doi:10.6342/NTU202204042

(Fig. 2-18(b)). After the fiber connecting the preform is cut-off, the drawing wheel is deployed and the dangling fiber is clamped with both wheels and the clamping pressure is monitored to ensure no slippage and no breakage (Fig. 2-18(c)). The motor is than engaged and the drawing process is started.

We tested our automated system initially by drawing unfilled preform because a pure glass fiber has smaller bending radius and not as fragile as an SCF. It would provide larger tolerance for breakage. The results are shown in table. A very consistent result was achieved and meters long of air core glass fiber can be drawn. When changing the drawing speed of motor, the cladding and core diameter of the glass fiber needs about 5 min of time to reach stable value. A detail analysis of the diameter during transient period was not carried out because we do not have equipment for monitoring the cladding and core diameter of the fiber during the drawing process. All fiber geometry measurements were done after the drawing process with a microscope. Through this experiment, we have proved that we can now control and maintain the geometry of our fiber (Table 2-6).

To test if we can increase the success rate of drawing SCF regardless of the outcome of Fl, preform filled with silicon powder is drawn with this system. Through multiple testing, the phenomenon where the fiber always breaks at the edge between filled core and unfilled core was observed. Now, the fiber breaks easily if noncontinuous core section occurs which pretty much occurs at every single drawing (Fig. 2-21). Therefore, we will need to solve the problem of air bubbles to ensure continues silicon core before using this system to control the geometry of the fiber.

doi:10.6342/NTU202204042

Preform Outer Diameter/ mm	Preform Inner Diameter/ mm	Feeding Speed/ mm s^{-1}	Drawing Speed/ mm s^{-1} (Motor voltage)	Cladding Diameter/ μm (±5)	Core Diameter/ μm (±5)
10	3	0.0072	5555(5V)	125	15
10	3	0.0072	4305 (4V)	150	20
10	3	0.0072	3055 (3V)	175	25

Table 2-6 Results of fiber drawing with different feeding and drawing speed

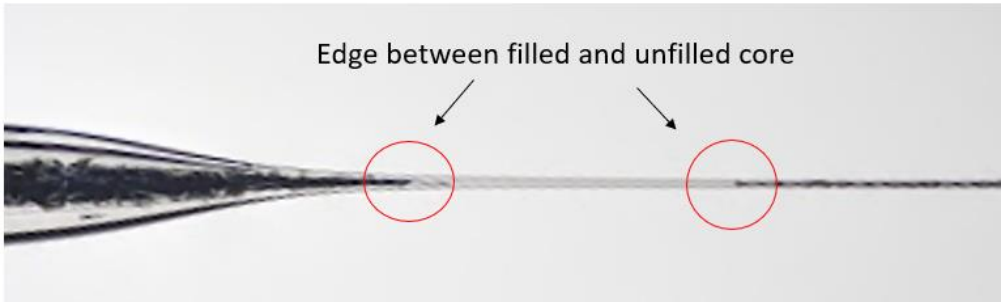

Fig. 2-21 Noncontinuous core section in preform

doi:10.6342/NTU202204042

2.6.2 Two-Stage Drawing Process

From Section 2.4, air bubbles trapped between molten silicon will cause high possibility of air pocket forming at the neck of preform which results in failure of drawing SCF. With some insights from the solder powder melting experiment in 2.4.1, we discover that tube diameter is a factor that determines if the air bubble can get trapped inside the preform. We will therefore need to increase the inner diameter of the preform. Due to the limitation of the preform outer diameter by the furnace width, the inner diameter of the preform will also be limited as the core/cladding dimension depends on the ratio of inner and outer diameter of the preform as well. Therefore, we need to use a two-stage method to draw a preform with a high inner to outer diameter ratio to an intermediate preform first. Then, the intermediate preform would be inserted into another glass tube so that the inner to outer diameter ratio is decreased to a value suitable for a final draw into optical fibers (Fig. 2-22). This process was recommended by expert for use in drawing chalcogenide glass fiber using granulated glass filling. They also recommended applying vacuum which is also used in powder in tube method for glass fiber during preform consolidification [47].

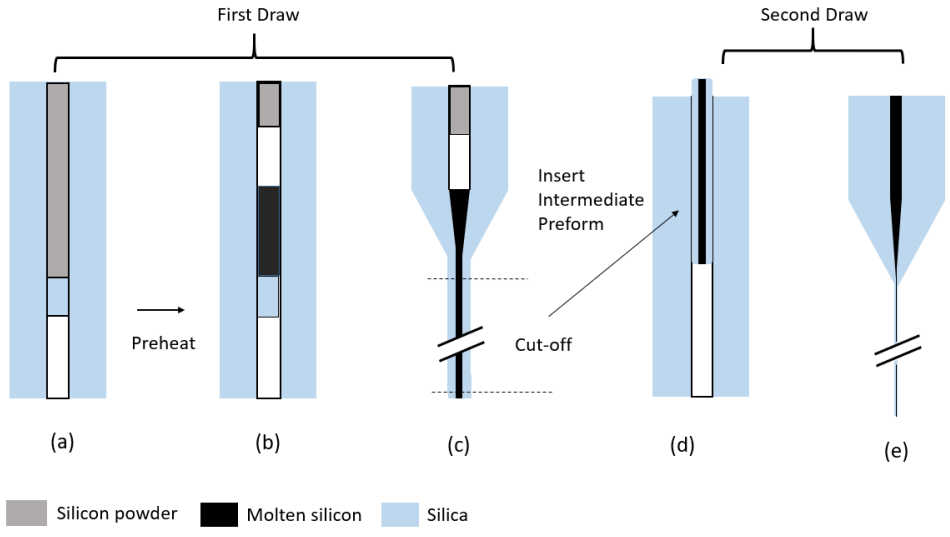

doi:10.6342/NTU202204042

Fig. 2-22 Two stage preform drawing process

2.6.3 Preform Drawing system

The main difference of this 2-stage drawing system from the previous set-up is the introduction of a lower pulling arm, tension sensor with computer automated speed control system. In our old set-up, the lower part of the preform is pulled by its own weight (free fall) to form a neck. It is a constant force system variable velocity system. We will not be able to produce long uniform diameter intermediate preform using this method as the diameter of the is a function of feeding and drawing speed. When the system is not in used for drawing, we can keep both arms stationary so that they can act as a holder for our preforms in the furnace. Our fiber drawing furnace can be used to heat up preforms with different core materials inside it as the preform can now stay for longer periods in the furnace. We can then study the fluid properties of these materials at very high temperature and the behavior of them in tube structures.

The upper and lower drawing arms consist of a stepper motor (57HBP56AL4-TF8A, 1.8°, 1.2Nm) driven linear stages with 4mm pitch of length 30cm and 60cm respectively (Fig. 2-23). The stepper motors are driven by a DM542 micro-step driver. The control system for the motors includes an Arduino Uno board controlled using MATLAB GUI which send signals to the other two Arduino Uno board that generate PWM signal to micro-step driver of the upper and lower arm. These Arduino boards communicate with each other using I^2C and the Arduino board connected to the computer serves as the “master” and the other two Arduino serve as the “slave” and generate PWM signal according to command from the “master” (Fig. 2-24). There is a slight difference between the calculated speed and actual speed of linear stage which we will need to consider if we want a precise control if the geometry of the intermediate preforms (Fig. 2-19).

doi:10.6342/NTU202204042

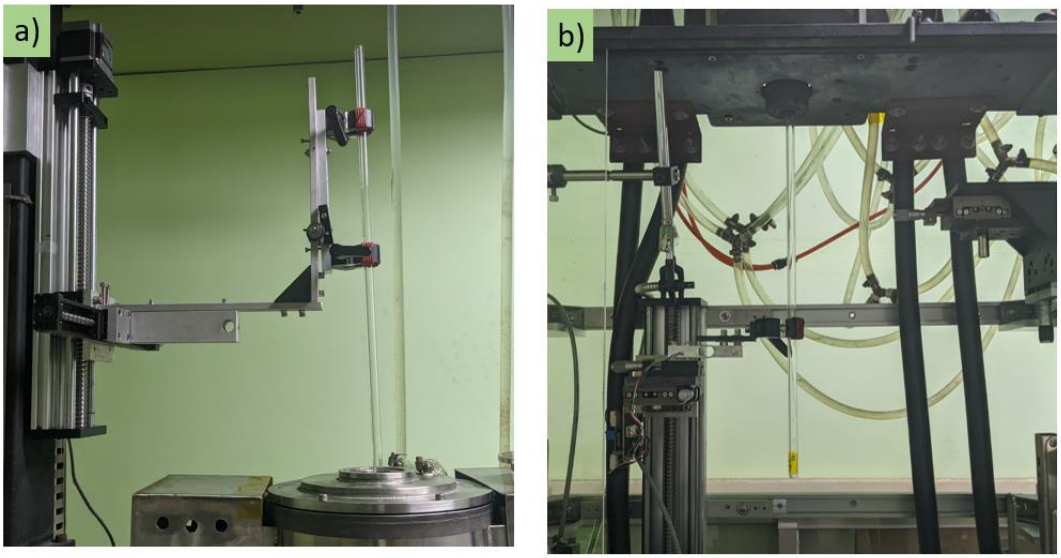

Fig. 2-23 Upper and lower arm of two stage preform drawing system

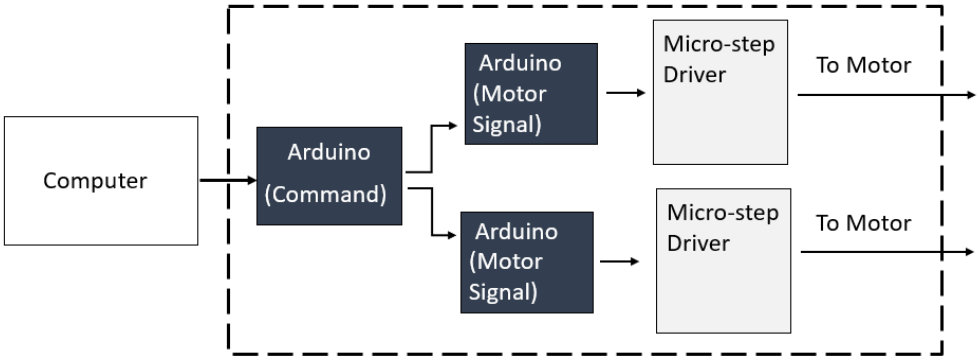

Fig. 2-24 Control system block diagram

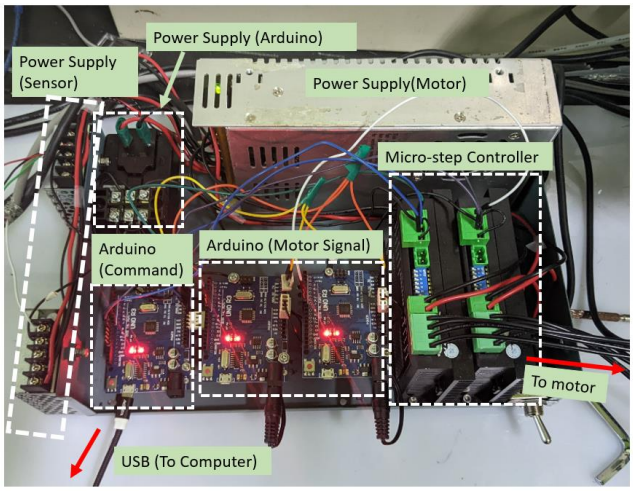

Fig. 2-25 Control box for housing components

doi:10.6342/NTU202204042

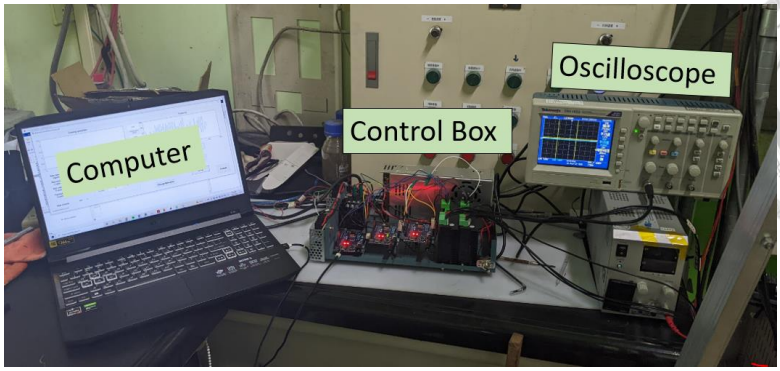

Fig. 2-26 Complete control system for two stage preform drawing system

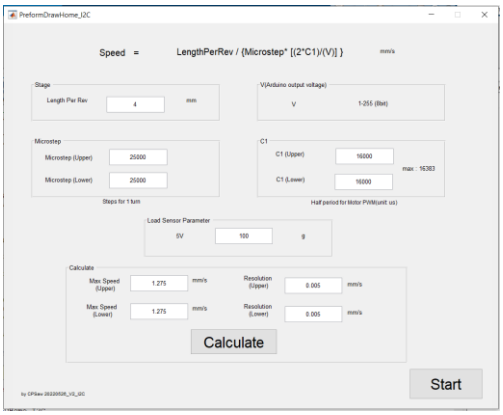

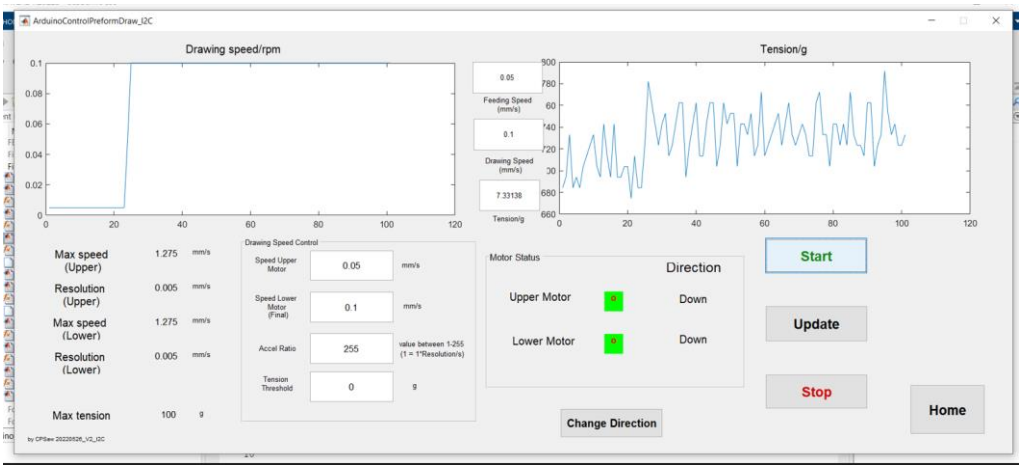

Fig. 2-27 MATLAB GUI for controlling the two stage preform drawing system

doi:10.6342/NTU202204042

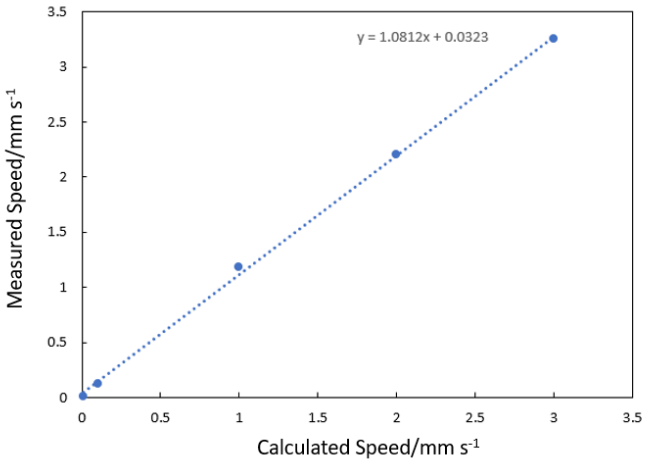

Fig. 2-28 Calculated speed vs actual speed

On the lower drawing arm, there is a tension sensor to monitor the tension of the preform during the drawing process (Fig. 2-29(a)). The tension sensor is a 1 Kg load cell and the signal is amplified by a CT33 amplifier module with an AD620 amplifier chip (Fig. 2-29(b)). The load cell functions by changing its shape slightly to the force applied to it, the change in shape is detected by the strain gauge and converted to electrical signal. The signal can be both positive and negative depending on the direction of the force applied to it. The CT33 module can then amplify both positive and negative signals produce by the strain gauge, and the signal is read by a multimeter(oscilloscope). We can also use the central zero-point calibration so that we can zero out the weight of the clamp that is attached on the loadcell.

This tension sensor serves two important purpose. The first one is to identify the heating time before starting the drawing process. When the preform is first inserted into the drawing furnace, some time is needed for the whole structure to reach the softening temperature of silica. If we started drawing too soon, there will be part of the structure still in brittle state, the preform will possibly crack or break off entirely. We identify this heating period by monitoring the signal from the loadcell. Before clamping the

doi:10.6342/NTU202204042

lower part of the preform after it is first inserted into the furnace, a negative load is slightly applied on the load cell before clamping the lower part of the preform. Before the preform softens thoroughly, the load cell's signal will remain negative. As the preform softens, the preform will slightly elongate. Its weight will also contribute to the downward force on the load cell and the signal will change from negative to positive. The second use of the tension sensor is to monitor the tension in the preform during the drawing process. If the tension is too high, the feeding and drawing speed might to too high and stress can build up in the silica. Adjustment such as lowering the speed or increasing the furnace temperature can be made to lower the tension. Fig. 2-30 shows the tension in the preform during preheat time recorded by the tension sensor.

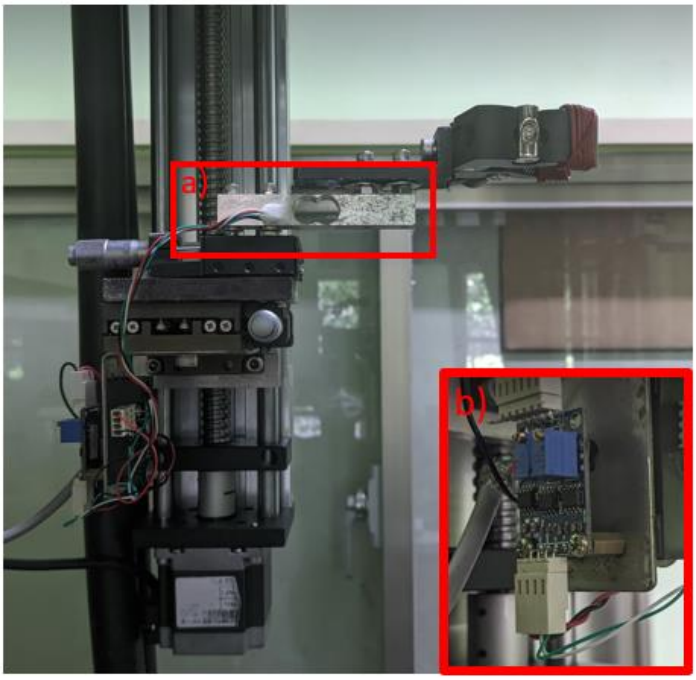

Fig. 2-29 (a)Load cell + clamp (b) Circuit for amplifying signal

doi:10.6342/NTU202204042

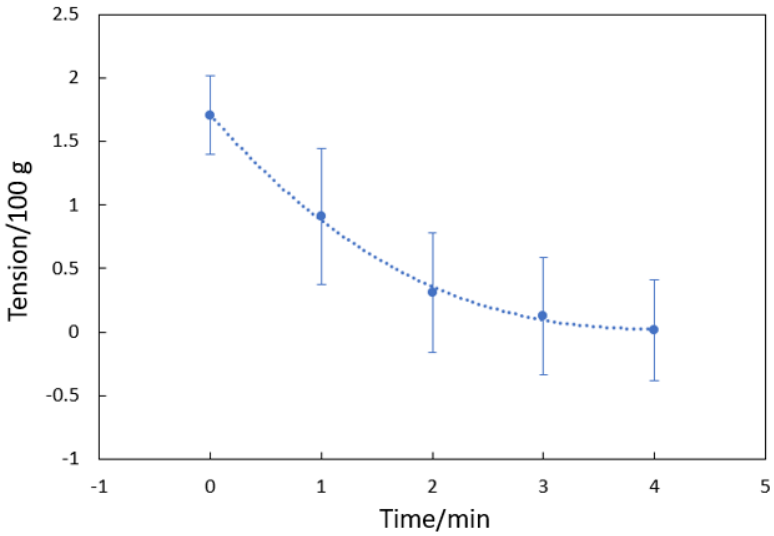

Fig. 2-30 Signal of load cell versus preheat time

2.6.4 Results

The intermediate preform system is first tested using an unfilled glass preform. Using a feeding speed of 0.0125 mm s^{-1} and a drawing speed of 0.375 mm s^{-1}, an intermediate preform with outer diameter of 6 mm and inner diameter of 1.8 mm is drawn from a preform with outer diameter of 10mm and inner diameter of 6 mm (Fig 2-31(a)). The hollow glass preform is drawn at 1897 K for 5400 s. The length of the intermediate preform is 135 mm. The intermediate preform is than insert into another preform as a preparation for the second stage drawing (Fig. 2-31(b)). A preform filled with silicon powder is tested for first stage drawing using similar parameters. Before filling in the silicon powder, the glass preform is first drawn for 300 s to form a small indent. A short length glass is inserted in the glass preform to seal the preform (Fig. 2-31(c)). The preform filled with silicon powder is than draw at 1942 K after a preheat time of 1 hour for the silicon to melt and flow down the preform. An intermediate preform with silicon core is drawn and the cross section shows that the silicon inside is indeed a whole solid structure (Fig. 2-31-(d)). As from section, we know that with an

doi:10.6342/NTU202204042

inner diameter of 6 mm, there will still be small air bubbles in the silicon core so we did not proceed to the second stage of the drawing. This system is also used to carry out all the experiments in this section.

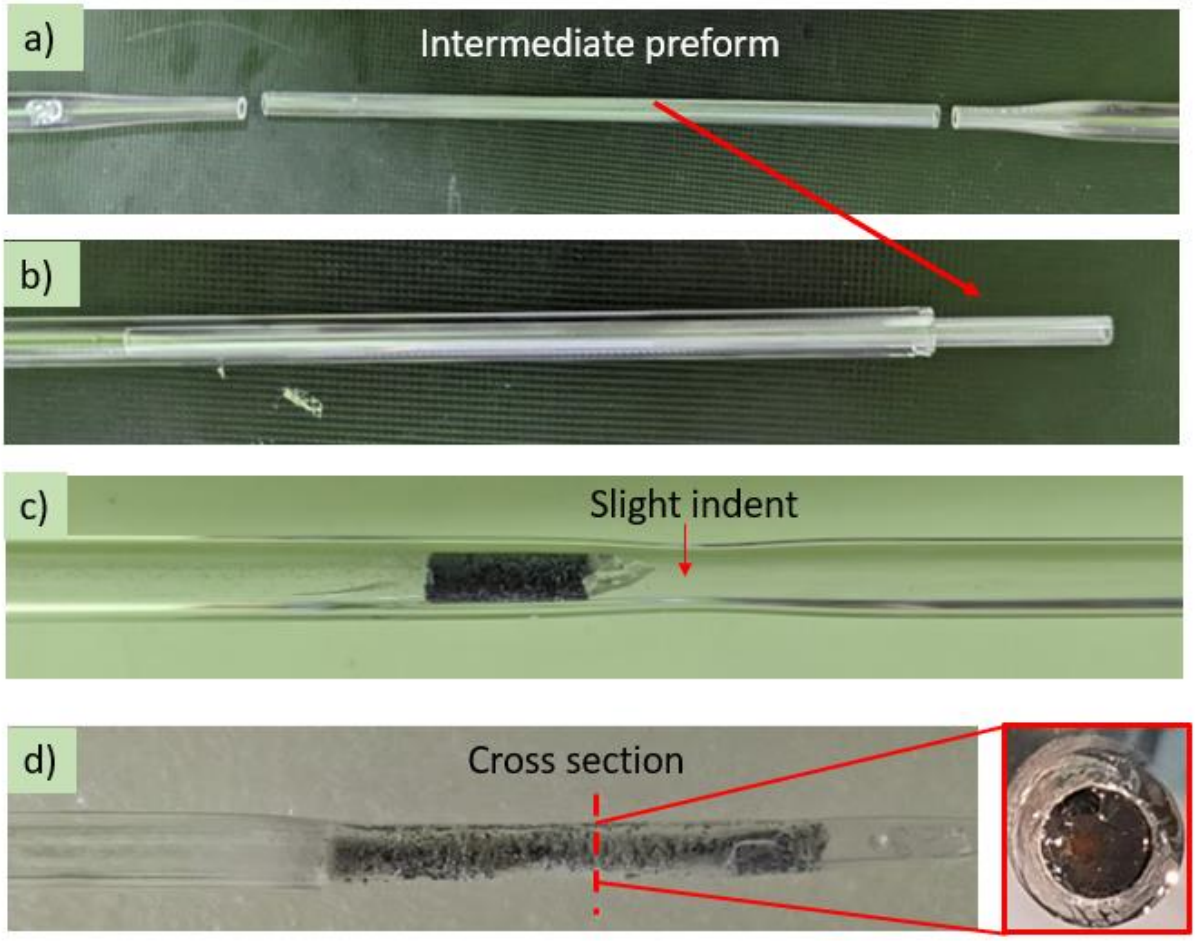

Fig 2-31 (a) Intermediate preform drawn from unfiled preform (b) Intermedium preform inserted into another preform (c) Slight indent in preform so silicon powder can (d) Intermediate preform drawn with silicon filled preform (Inset) Solid core but still with holes

doi:10.6342/NTU202204042

2.7 Thermal Modelling of Drawing Furnace and Preform with COMSOL Multiphysics

Fiber drawing is large part a thermodynamic and fluid dynamic process. A lot of outcome during the fiber drawing process is related to temperature of the preform. For example, the core and cladding diameter of the fiber depends on the neck shape of the preform which is a function of temperature distribution during the drawing process [38]. The temperature during drawing can also affects the stress accumulation in the fiber which can cause structure weakness [48-49]. Therefore, an understanding of the temperature distribution of the preform in the furnace and how to manipulate it is important. As it is hard to directly measure the temperature of the preform inside an enclosed furnace, an easier method is to do thermal modelling as demonstrated by other research that involves high temperature furnace [50-51].

In section 2.3.2, we also discovered that there is thermal inconsistency throughout our experiment. Through thermal modelling, we can study how different components in the furnace influenced the temperature distribution so that we know how tight the tolerance we need to control for each furnace parameters. The effects of wear and tear of the component on the temperature distribution can be studied as well and can be useful for maintaining the furnace at good working condition.

Of all the commercial simulation software, COMSOL Multiphysics is chosen as our tool for thermal modelling. The primary reason is that it has seamless integration between different physics phenomena such as heat transfer and fluid flow and we can always continue to develop the model into more complex system that consist of a lot of other physics process. For example, we can combine this thermal model with the dynamic process of neck formation during fiber drawing by modelling the melting of

doi:10.6342/NTU202204042

preform. Besides, a lot of the supportive information about COMSOL is available online so we can easily learn from these sources.

2.7.1 Geometry and Material Constants

The geometry of our furnace is built using a 2D axis symmetry model (Fig. 2-32). The dimensions and components of the furnace model is based on the drawings in Fig. 2-33. In the middle of our furnace model, a silica preform of with 10 mm diameter is included so we can directly study the temperature of preform in the furnace. The copper electrode is not included in the model as it is plane symmetry and will impede the gas flow in our model if it is modelled as an axis symmetry object. Due to its position further away from the high heat zone at the center of the furnace, its effect on the preform temperature distribution is less significant and it can be strategically excluded from our model.

All of the material constants used in our model are from the material library in COMSOL Ver. 5.5 as all of the materials parameters provided to us by the manufacturers are single temperature parameter measured at 297 K. For our high temperature furnace model, this type of parameter would not be very accurate. The graphite heating element and center graphite tube is made from IGS-743 isostatic graphite fabricates for us by Central Carbon Co. The material of the graphite insulation tube is unknown to us. These components are modeled using material constants of Graphite 7087 instead. The graphite felt insulation and N_2 gas are modeled with material constants of Graphite Felt and N_2 from material library respectively while the silica preform is modeled using material constants of Corning glass.

doi:10.6342/NTU202204042

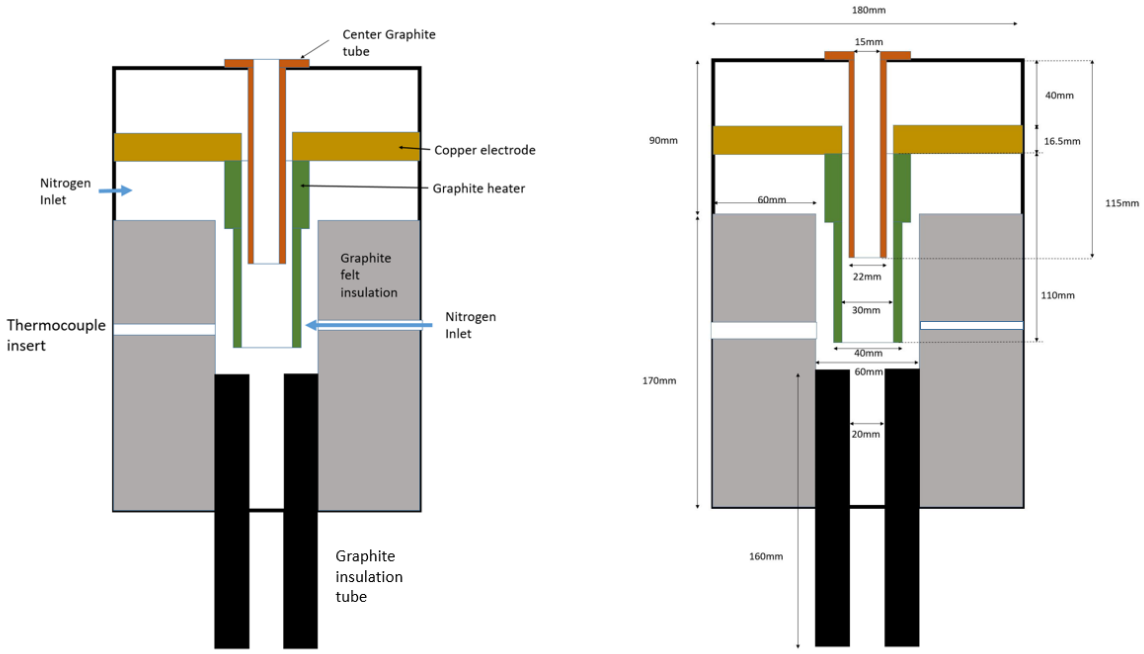

Fig. 2-32 Drawings and dimension of furnace

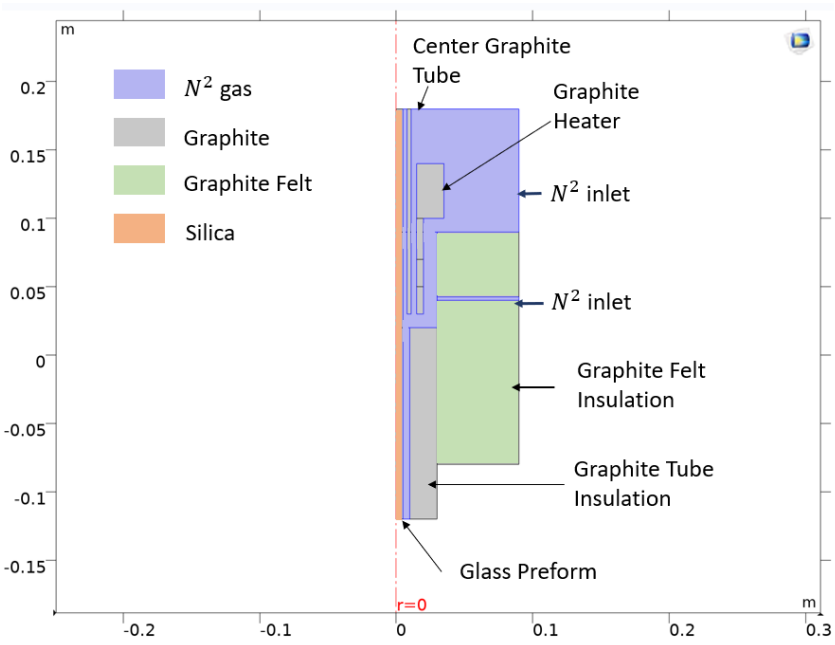

Fig. 2-33 Geometry and material of different parts in the fiber drawing furnace

doi:10.6342/NTU202204042

2.7.2 Thermal Model and Governing Equations

Heat transfer in the furnace is modeled using 3 processes which are heat conduction in solid and fluid, surface-to-surface radiation and forced convection by gas in the form of turbulent laminar flow. In the solid and gas region, conduction is governed by the Eq. (2.2) and Eq. (2.3) respectively [52]:

$$\rho C_p \frac{\partial T}{\partial t} + \nabla \cdot \mathbf{q} = Q_{\mathrm{ted}} + Q \tag{2.2}$$

$$\rho C_p \left(\frac{\partial T}{\partial t} + \mathbf{u} \cdot \nabla T \right) + \nabla \cdot \mathbf{q} = Q_{\mathrm{vd}} + Q_p + Q \tag{2.3}$$

$$\mathbf{q} = -\kappa \nabla T \tag{2.4}$$

where ρ is the density, Cp is the specific heat capacity at constant pressure, T is the absolute temperature, u is the velocity vector, q is the heat flux by conduction, Q contains heat sources, Q_{ted} is the thermoelastic damping, Q_{vd} is the viscous dissipation in the fluid, Q_p is the work done by pressure change in the fluid, κ is the effective thermal conductivity.

Besides conduction, energy transfer through radiation becomes significant due to the high temperature inside the furnace. The inner walls of the whole furnace are all model as gray and diffusive bodies and the heat transfer by radiation by these surfaces is governed by the Eq. (2.5) [52]

$$q = (1 - \rho_s) G - J \tag{2.5}$$

where q is the net radiation heat flux (energy), G is to irradiation (incoming radiation) and J is the radiosity (outgoing radiation flux), ρ_s is the specular reflectivity. The radiosity can then be expressed as:

doi:10.6342/NTU202204042

$$J = \rho_d G + \varepsilon n^2 \sigma T \tag{2.6}$$

where ρ_d is the diffuse reflectivity, ε is the emissivity, n is the refractive index, σ is the Stefan's constant and T is the temperature. The first term in the equation is the diffuse reflection of irradiation and the second term is the power radiated according to Stefan-Boltzmann Law.

In our furnace, N_2 gas is flowed into all empty spaces of furnace to eliminate oxygen. This flow of nitrogen is the source of forced convection inside the furnace. It is modelled as laminar flow instead of turbulent flow in the entire furnace because in the center part of the furnace and around the preform, the space between walls are narrow. Therefore, it is sufficient to make this assumption as fluid flow near the walls are generally laminar. The flow of the compressible gas is governed by the continuity equation Eq (2.7) and momentum equation Eq (2.8) [53]:

$$\frac{\partial \rho}{\partial t} + \nabla \cdot (\rho \mathbf{u}) = 0 \tag{2.7}$$

$$\rho \frac{\partial \mathbf{u}}{\partial t} + \rho \mathbf{u} \cdot \nabla \mathbf{u} = -\nabla p + \nabla \cdot \left(\mu(\nabla \mathbf{u} + (\nabla \mathbf{u})^T) - \frac{2}{3}\mu(\nabla \cdot \mathbf{u})\mathbf{I} \right) + \mathbf{F} \tag{2.8}$$

where ρ is the density, **u** is the velocity vector, p is pressure, μ is the dynamic viscosity, **F** is the volume force vector, T is the absolute temperature and **I** is the identity tensor.

To include the change in temperature of N_2 gas, effects of non-isothermal flow in our forced convection system is achieved by coupling the physics model of laminar flow and to heat transfer in fluid by solving Eq. (2.3) and Eq. (2.8) together in the gas region. All three heat transfer processes are than coupled together under Multiphysics function in COMSOL.

doi:10.6342/NTU202204042

2.7.3 Boundary Conditions

The heat source in our furnace is a graphite heater. As the heater is not axis symmetry, we cannot model them in our 2D axis symmetry model. To imitate the effects of the real heater, heat source in our model is divided into four sections according to the different section in our heater (Fig. 2-34). Temperature distribution of the simplified heat source model is than compared to a 3D thermal model of graphite heating element simulated using electrical heating physics. Using a 3D model for the whole furnace takes too much time and memory as the volume of the furnace is much larger and there are more physics to be solved in the whole furnace.

Each section in the graphite heater is assigned a different heat flow rate due to the difference in resistance and number of current paths (Fig. 2-34). The heat flow rate, Q is calculated based on resistive heating power. The power per unit length, P_0 can be calculated based on the current, I resistance per unit length, R. R in turn can be express as the resistivity per unit length, ρ and cross section area, A. The total power produce by each region is a product of current paths, length of the region, L and P_0 Eq. (2.11).

$$\mathrm{Q} = \frac{P_T}{V} \tag{2.9}$$

$$P_0 = I^2 R = I^2 \frac{\rho}{A} \tag{2.10}$$

$$P_T = P_0 \times n \times L \tag{2.11}$$

The normalized total power the flow into each section is calculated. The total power is than found using iteration method, while keeping the ratio of total power in each section similar to the ratio of normalized calculated total power in each section. This is because we don't know the exact current flowing through heater and the

doi:10.6342/NTU202204042

resistivity of the heater. The sets of value where preform temperature reached around 2000 K is chosen as a reference and can be found in Table 2-7.

The outer wall of the furnace is set to a constant temperature of 297 K to mimic the water-cooling system around the furnace. In our experiment, we use a continues open loop flow of water and monitor the input and output temperature of the water. The temperature of the inflow and out flow always maintains within 0.5 K of room temperature. Two inlet and two outlet of nitrogen gas is also built on the outer wall of furnace. The inlet is characterized and inflow rate between 5-7 LPM which is the actual flow rate used in our N_2 gas system. The outlet is modelled as a constant pressure surface of 1 atm to mimic openings expose directly to open area (Fig.2-35).

Region	Current paths, n	Area, A /mm^2	Length, L/mm	Calculated total power, P_T (Normalized)	Total power used in simulation, $\frac{P_T}{W}$
Hat	2	376	45	1	40
Upper	2	94	30	2.67	106
Middle	4	40	20	8.33	333
Lower	12	16	20	62.5	2500

Table 2.7 Calculation of total power in different section of graphite heater

doi:10.6342/NTU202204042

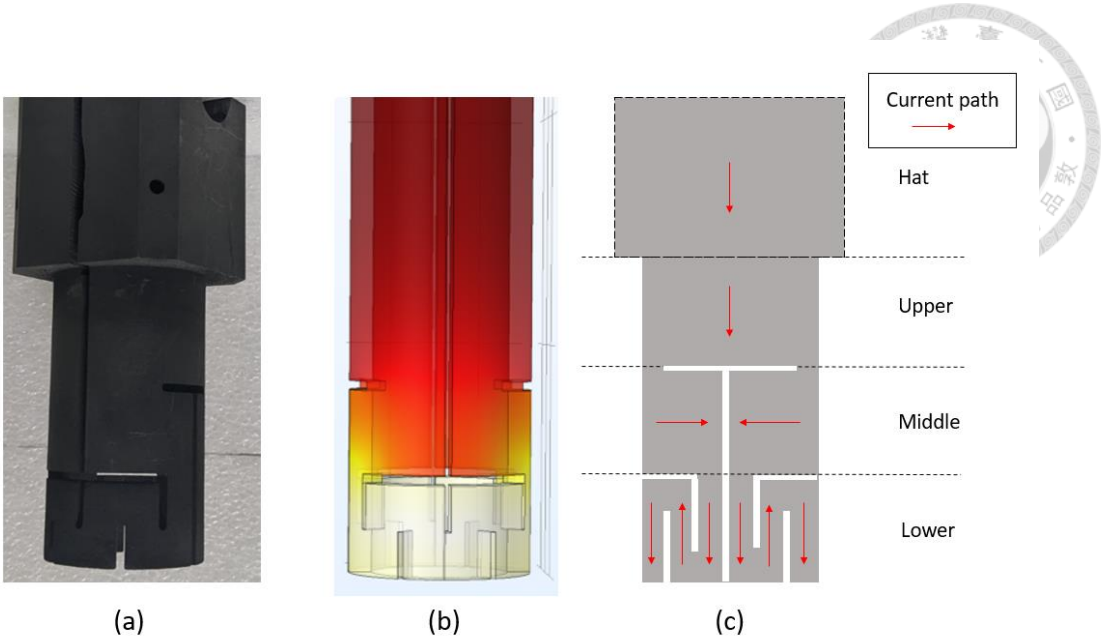

Fig. 2-34 (a) Graphite heater (b) Graphite heater drawn in COMSOL (c) Current paths along the graphite heater

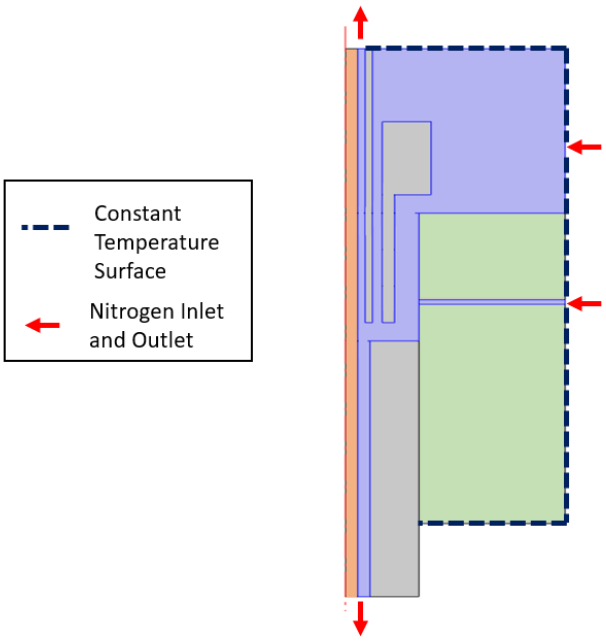

Fig. 2-35 Constant temperature surface and N^2gas inlet and outlet in the furnace.

doi:10.6342/NTU202204042

2.7.4 Results

2.7.4.1 Temperature Distribution

The temperature plot shown in this section is the steady state temperature which occurs about 300 s from start at an initial temperature of 297 K. The preform is modeled as a solid that does not change shape even above softening point. So, this thermal model simulates the time period where the preform had just heat up above softening point but yet to start deforming in real situation.

Fig. 2-36 shows the temperature distribution inside our optical fiber drawing furnace. The highest temperature zone occurs around the lower part of the graphite heater due to high power deliver to that area via the graphite heater. Fig 2-37 shows the temperature along the surface of the preform which is the temperature measured along the black solid arrow line. The area with peak temperature is just beside the lower part of the graphite. Further away from the lower part of the graphite in both directions, the temperature falls off. The temperature gradient is steeper at the lower side of the furnace because there is no heating element in the area.

To compare the temperature distribution of the graphite heater between the 3D electric heating model and the simpler 2D axis symmetry heat source model, the temperature along the surface of both models are plotted in Fig. 2-38 and Fig. 2-39 respectively. Both models show temperature 2 time higher in the lower region of the heater compared to the hat region of the heater. In the 3D model, the temperature gradient between the lower region and middle region is much steeper compared to the 2D model. This is because in the 3D model, only heat transfer within solid is simulated so less heat can transfer between the lower and middle part of the heater due to the airgap between both region them. In the 2D model, heat is transfer via conduction,

doi:10.6342/NTU202204042

convection and radiation, even with less contact area between the lower and middle region of the heater, more heat can be transfer which result in a milder temperature gradient. Other than that, the 2D model is a good representation of the 3D model.

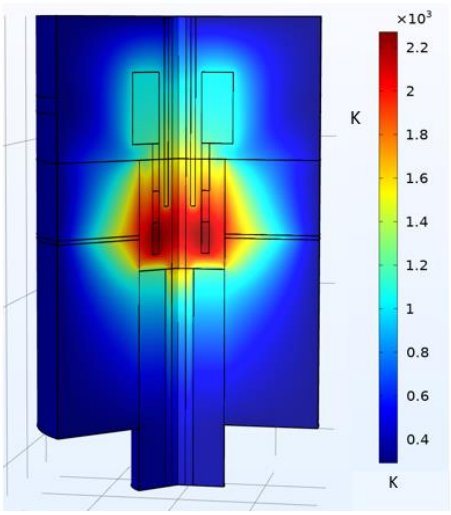

Fig. 2-36 Temeprature distribution in the fiber drawing furnace.

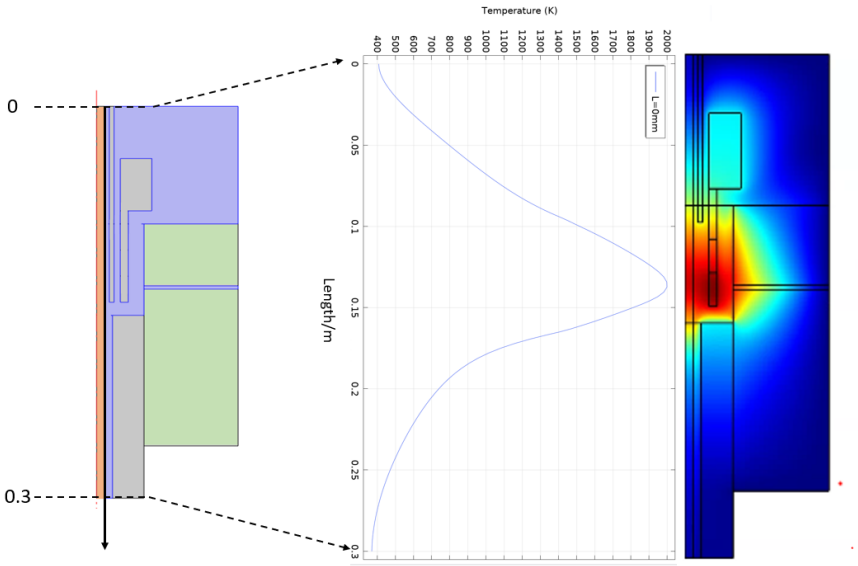

Fig. 2-37 Temperature distribution along the preform axial axis

doi:10.6342/NTU202204042

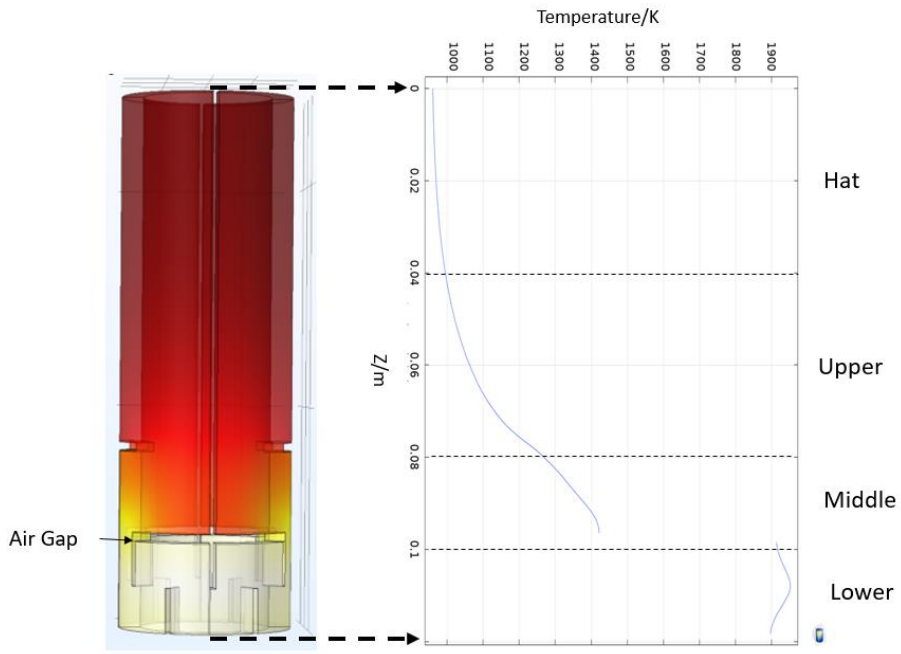

Fig. 2-38 Temperature along the surface of graphite heater modelled using resistive heating method

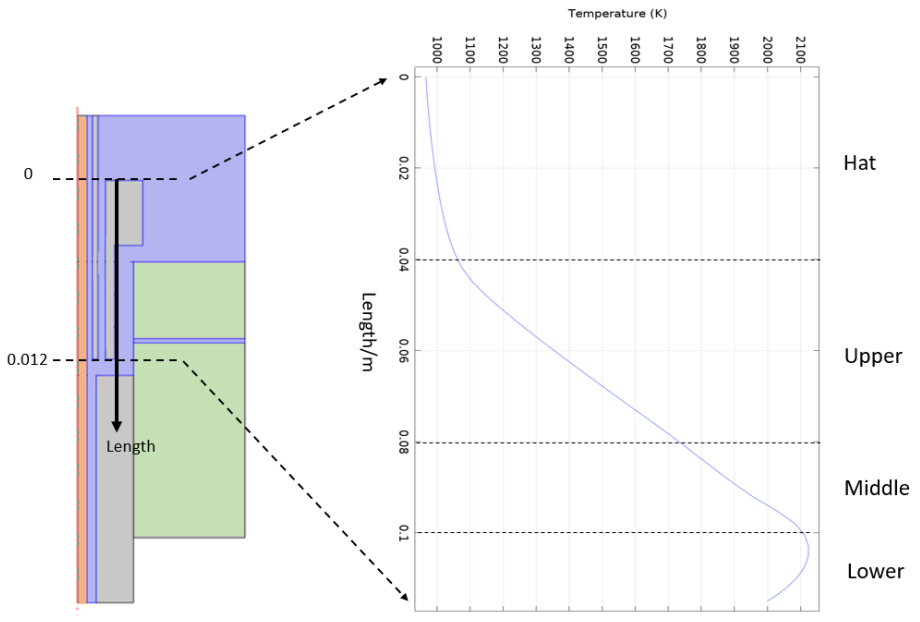

Fig. 2-39 Temperature along the surface of graphite heater modelled using heat flux method

doi:10.6342/NTU202204042

2.7.4.2 Effect of Components on Temperature Distribution

In this section, we will be exploring how the change in geometry and position of components in the furnace affect the temperature distribution of the preform. This is to investigate how the wear and tear that occur in the furnace and maintenance difference causes temperature inconsistency as mentioned in section 2.4.

Center tube length

The function of the center tube length is to prevent the preform from directly touching the graphite heater and the cap on the tube is to prevent N_2 gas from flowing out (Fig. 2-2). Our main interest is in the effect of tube length on the temperature distribution in the furnace as over time, the center tube disintegrates and the length of the tube shortens. We will denote L as the length difference the position of the bottom of the graphite heater to the position of the bottom of the when installed in the furnace (Fig. 2-40). When L= 0, the bottom of the center tube is at the same position as the bottom of the graphite heater.

When L increases from 0 mm to 10 mm, the maximum temperature of the preform drops from 1940 K to 1920 K. However, when L increases from 10 mm to 50 mm, the maximum temperature increases and reach a plateau when L = 20 mm with temperature of around 2000 K. The max temperature against L is plotted in Fig. 2-41, we can see that the difference between the lowest and highest temperature is about 80 K. This phenomenon can be explained by the convection and radiation heat transfer difference between different length of L. Between L < 20 mm and L > 20 mm, we can see that the radiation absorbed by the by preform when L > 20 mm is higher. This is because the radiation from the highest temperature region of graphite heater, the lower region directly hits the preform. If L < 20 mm, the radiation from the lower region of

doi:10.6342/NTU202204042

the heater is blocked by the longer center graphite tube (Fig. 2-42). As for the dropped in temperature between $0 < L \leq 10$ mm, this can be explained by the lack of convection at the region with no center graphite tube as can be seen from the air velocity plot (Fig. 2-43). the effect is compensated by more heat radiation transfer as L increases and therefore the temperature increases again after L >10 mm.

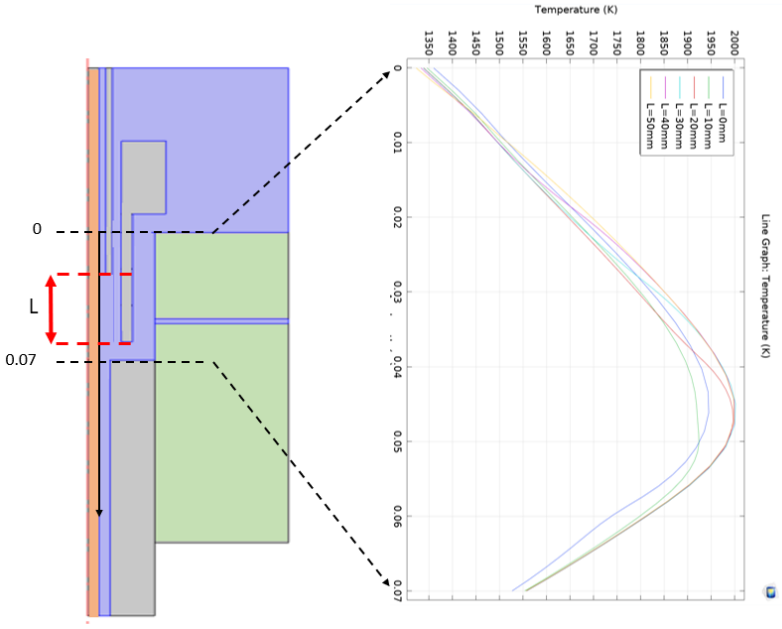

Fig. 2-40 Temperature distribution along the preform axial axis

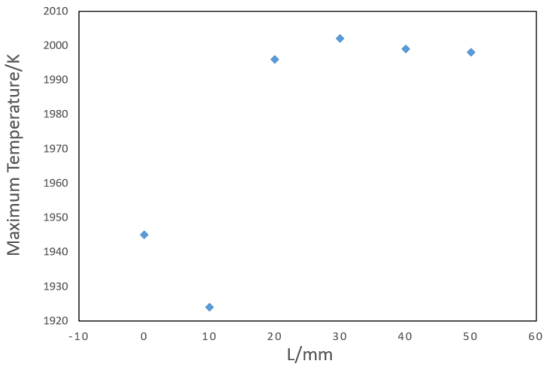

Fig. 2-41 Maximum temperaure at the surface of preform for different graphite tube length.

doi:10.6342/NTU202204042

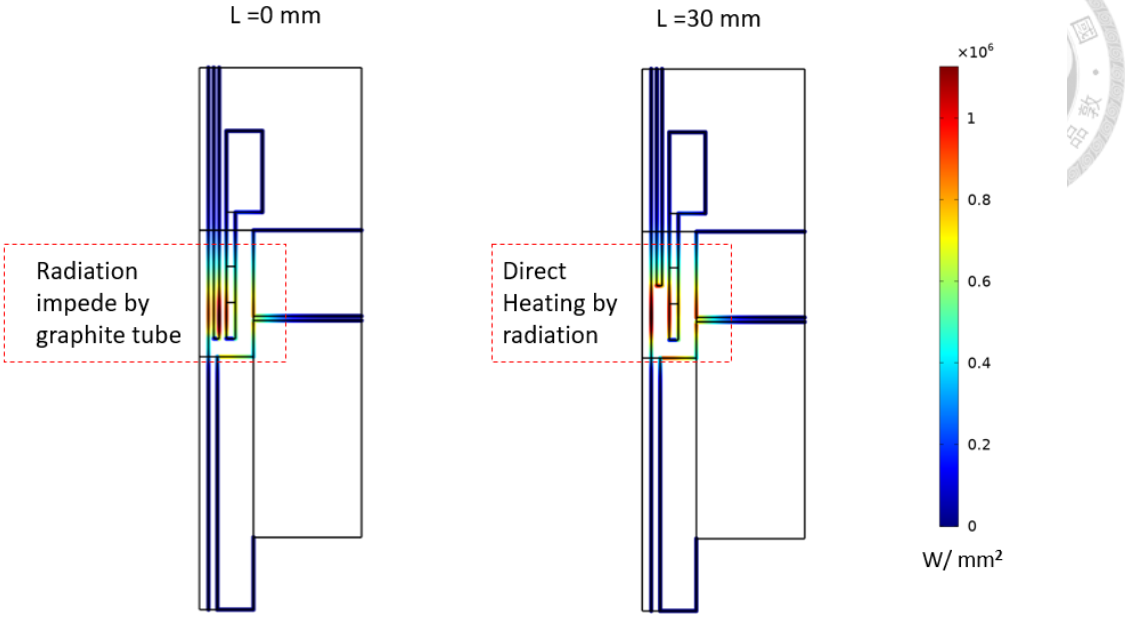

Fig. 2-42 Power absorb through radiation by preform and furnace surfaces for different central graphite tube length.

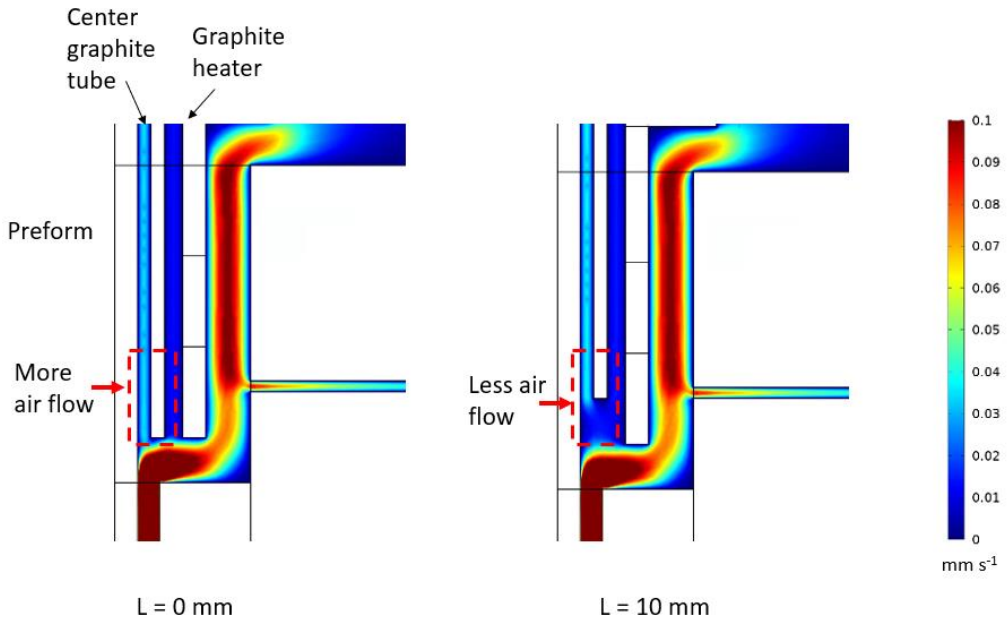

Fig. 2-43 Flow rate in the furnace with different length of central graphite tube.

doi:10.6342/NTU202204042

Thermocouple position

The thermocouple in the furnace is inserted from the side of the furnace passing through the graphite felt. The position for insertion is just beside the N_2 gas inlet. The tip of the thermocouple which is the measuring point is embedded inside the felt. Therefore, the measured temperature by the thermocouple is not the real temperature of the preform but the temperature of the graphite felt at the measuring. From Fig. 2-44, the temperature inside the graphite felt along the N_2 gas inlet horizontally was plotted at different supplied power to the lower region of the graphite heater. We can see the temperature of the graphite felt lowers moving away from the graphite heater at all power. On the other hand, at the same position, temperature is higher if the power is higher. Similarly, the temperature of the preform increases as power increases (Fig. 2-45). As the furnace system has a feedback system to keep the measured temperature at constant temperature, if the thermocouple is placed further away from the graphite heater, more power is supplied to the graphite heater to keep the thermocouple to register the same measured temperature. This would result in higher real temperature even if the thermocouple measured the same temperature. For each 100 W increase in supplied power, the temperature of the preform increase by about 40 K at the maximum temperature point (Fig. 2-45). As the thermocouple move further away by 1 mm, the supplied power need to increase by 100 W to maintain the temperature measured by the thermocouple if its initial position is within 10 mm from the inner side of the graphite felt insulation (Fig.2-44). Therefore, for each 1 mm fluctuation in the thermocouple position, the real maximum temperature of the preform fluctuates by 40 K.

doi:10.6342/NTU202204042

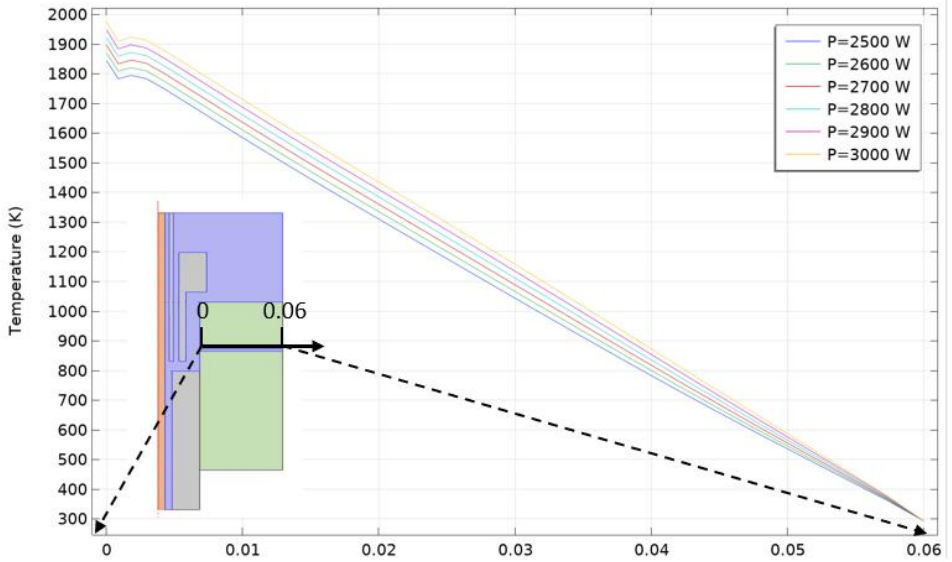

Fig. 2-44 Temperature distribution along the insert tunnel for thermocouple at different graphite heater power.

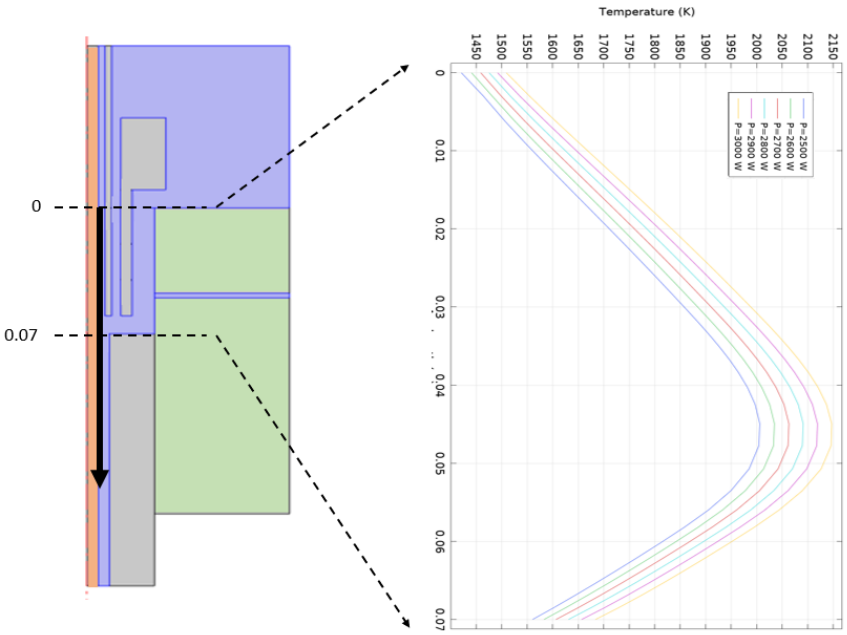

Fig. 2-45 Temperature distribution along the preform axial axis at different graphite heater power.

doi:10.6342/NTU202204042

Graphite Felt Insulation

The graphite felt insulation's function is to isolate the high temperature in the furnace from the outside environment. As it is close to graphite heater, the graphite felt insulation disintegrates particularly near the middle and lower region of the graphite heater, forming a large indent in the wall of the insulation layer. The temperature distribution of both the furnace with perfect and disintegrated graphite felt insulation layer is plotted in Fig 2-46. The high temperature zone in the furnace with disintegrated layers spreads out and the overall temperature is lower compared to the perfect furnace. The temperature along the axis of the preform is plotted in Fig. 2-47 with different D, the depth of the indent in the insulation wall. As D increases, the preforms overall temperature dropped. The area with largest temperature change is near the highest temperature region with the maximum temperature dropping by about 50 K for each 10 mm increase in D.

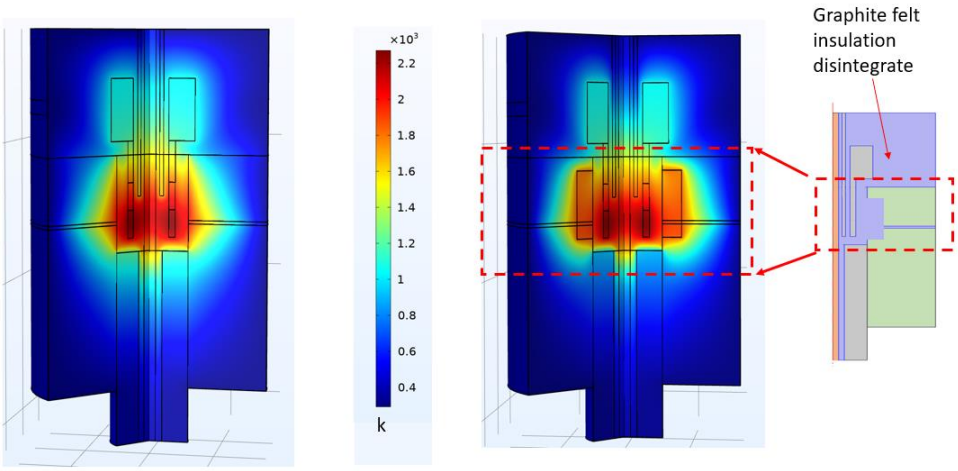

Fig. 2-46 Temperature distribution in the furnace when the graphite felt insulation is (Left) perfect (Right) disintegrated.

doi:10.6342/NTU202204042

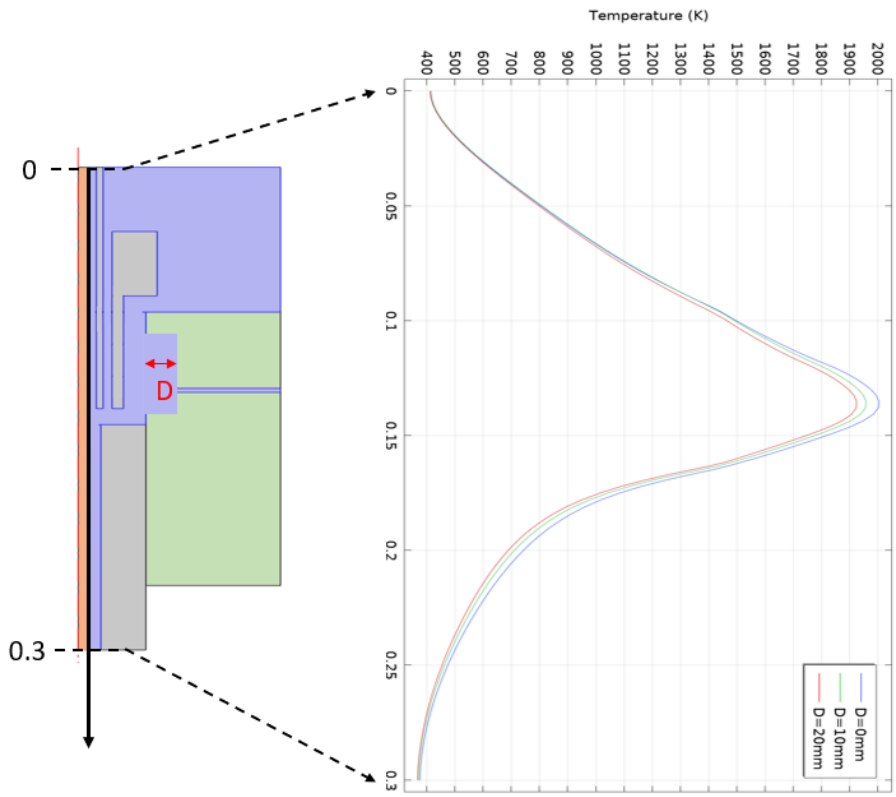

Fig. 2-47 Temperature along the prefrom axial axis at different graphite insulation indent depth, D.

doi:10.6342/NTU202204042

Flow rate

The forced convection in the furnace is facilitated by the flow of high pressure N_2 gas. The flow rate of the gas can be easily controlled via the gauges on the gas cylinder. Therefore, we are interested to see if this parameter can be used to change the temperature distribution of the preform. In Fig. 2-48, the temperature distribution of the preform is plotted with flow rate ranging from 3 LPS to 7 LPS. For all flow rate, the temperature distribution at steady state remains nearly the same in the highest temperature region. Only in the lower part of the preform, where temperature difference can be seen, with lower temperature for higher flow rate. This is probably due to higher velocity at the lower part of the furnace.

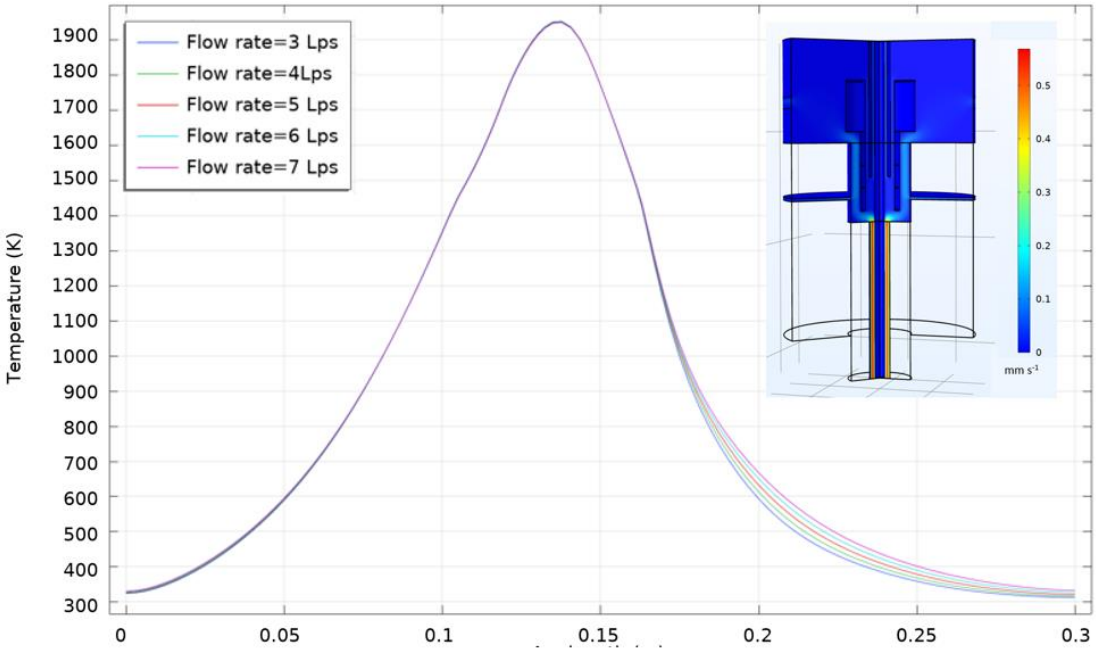

Fig. 2-48 Temperature along the prefrom axial temperature at different N^2 gas flow rate.

doi:10.6342/NTU202204042

2.7.5 Experiment Verification

We cannot directly measure the temperature of the preform as mentioned in the thermocouple section. Instead we have to use an indirect method such as the falling time of the preform to predict the relative temperature between preforms. In this section, the falling time of an unfilled glass preform is used as an indicator for maxim temperature in the furnace for greater consistency compared to filled preform. A faster falling time is generally correlates to higher temperature of preform because of the lower viscosity of the glass preform, that provides lower tension against the pulling force of the gravity. Therefore, the mean drawing speed will be faster hence lower falling time.

Thermocouple position

The falling time of the preform is plotted against different measure temperature at different thermocouple position. The edge of the graphite felt insulation is used as the reference line to define the position of the thermocouple. The distance of the tip of the thermocouple from the edge of the insulation wall is denoted d (Fig. 2-49). From Fig. 2-50, we can see that as the measured temperature (by thermocouple) increases, the falling time decreases for all thermocouple position. This confirms the correlation between high temperature and low falling time.

Again from Fig. 2-50, we can see that as the thermocouple is closer to the graphite heater, the falling time increases. This indicates that as the thermocouple is further away from the graphite heater, real temperature of the preform is higher even with when the measured temperature shows similar value. This agrees with our simulation that more power is needed to keep the measured temperature at a constant when the thermocouple is further away from the graphite heater, which result in higher temperature. When d is near 0, the temperature difference between d is larger, probably due to tip of the thermocouple being directly heated by the radiation of the graphite

doi:10.6342/NTU202204042

heater. This is because the tip is not shielded from the insulation wall when it is near the edge of the insulation wall. When the tip of thermocouple is further into the insulation wall where it is not subjected to direct radiation heating, the temperature on the tip will be closer to the temperature of the insulation wall. This radiation effect is not considered in the simulation therefore the temperature at the tip of the thermocouple at d near 0 might be higher than that in the simulation.

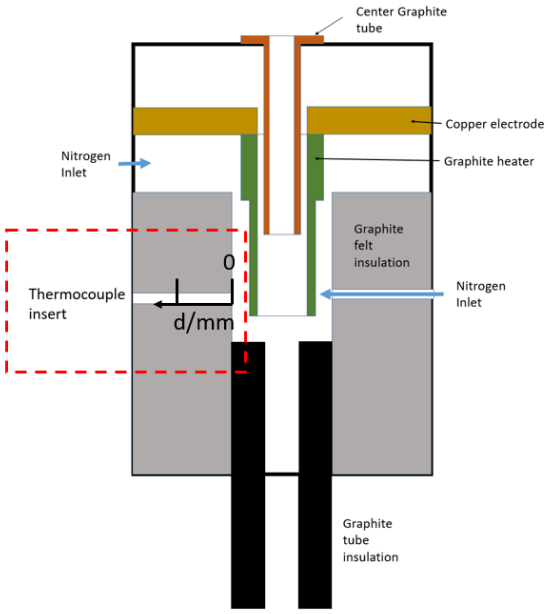

Fig. 2-49 Thermocouple insert.

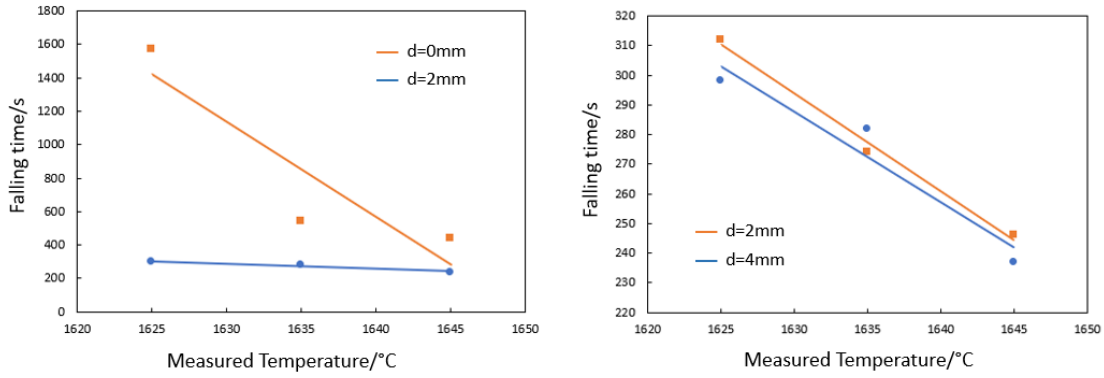

Fig. 2-50 Falling time for different thermocouple insert depth.

doi:10.6342/NTU202204042

New Central Graphite Tube and Graphite Felt

After our furnace was sent for refurbished, two components that shows big difference before and after refurbished is the central graphite tube and the graphite felt. From Fig. 2-51, the old and new graphite tube is placed side by side for comparison and length between them is instantly noticeable, with a 30 mm difference between them. In the old furnace, there is a considerably area of graphite felt that had disintegrated (Fig. 2-52(a)) compared to the new furnace (Fig. 2-452(b)). The tip of the thermocouple is even visible. To verify the effect of center graphite tube length on the temperature of the preform, we fabricated a new shorter center graphite tube and compared the falling time of preform in the new furnace that using the longer center graphite tube. Using the notation L from section 2.6.4.2, the mean and standard deviation of falling time is tabulated. We can clearly see the temperature difference between the two length through the difference in falling time as predicted in the simulation (Table 2-8).

Falling time/s	L = 0 mm	L = 30 mm
Mean	2244	1139
S.D.	916	175

Table 2-8 Falling time for two different length of central graphite tube.

On the other hand, in the data set CP&Paul_1, we can see that the temperature of the furnace does not reach 1645 °C even though the furnace is always set to 1645 °C. This is probably due to electrical system of the furnace cannot provide enough power to heat up the furnace to the set temperature as the heat energy is spread to a larger region as seen in the thermal modeling.

doi:10.6342/NTU202204042

Fig. 2-51 Longer vs shorter central graphite tube.

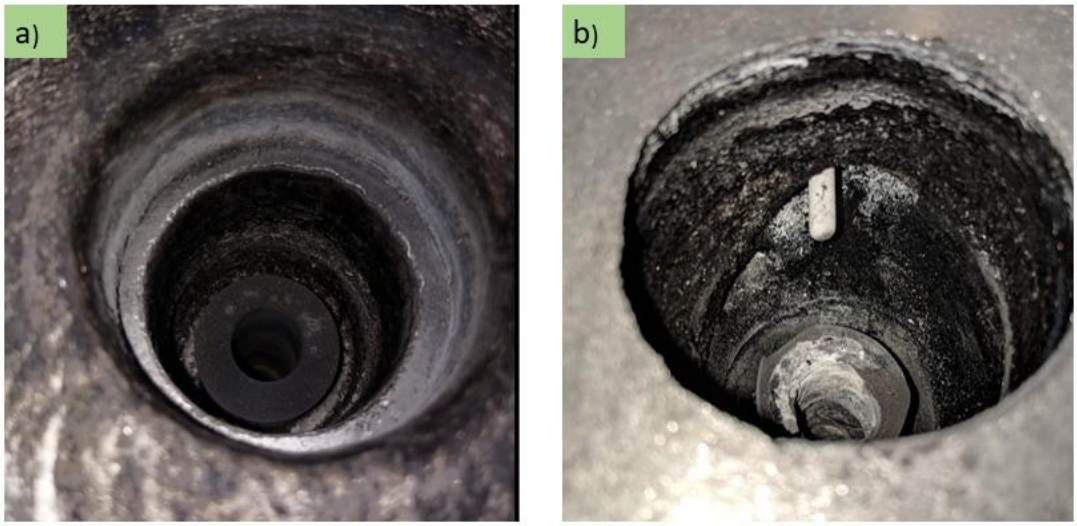

Fig. 2-52 (Left) New graphite insulation layer (Right) Disintegrated graphite insulation layer

doi:10.6342/NTU202204042

2.8 Summary

In this chapter, we have found the main cause for the empty core problem in our SCF production which causes not only low yield but also mechanical problems during drawing process. Some possible solutions including new process to the empty core problem have been suggested although further investigation needs to confirm our results. In the process, we have also built several automated systems that can greatly aid in the production of SCF with precision. Lastly, with the help of thermal modelling with COMSOL, we have gain better understanding of our furnace and validated them experimentally. Using the same modelling method, further investigation on the thermal and fluid behavior in the preform during fiber drawing process might provide more insight for the solutions to the fiber drawing problems we are facing now.

doi:10.6342/NTU202204042

Chapter 3 Improving Quality of SCF

3.1 CO2 Laser Annealing of SCF

3.1.1 Introduction

In the melt growth recrystallization process, a heat source such as laser, or a graphite heating source is used to heat the material to be recrystallize to its melting temperature. The heat source is than removed from the location such as moving the heat source to a different position or turning the heat source off. When the melt pool cools down, it will solidify. The edge between the molten and solid material is called the phase front. At the phase front where solidification occurs, there are a few interesting phenomena such as nucleation and crystal growth that happened during solidification process. The crystal structure of the solid formed will be determined by these phenomena [54].

Some of the important factors that will influence the melt growth recrystallization process are temperature gradient, ∇T across the phase front and the moving speed of the phase front, v_{phase} [55-57]. The multiplication of both the parameters forms the cooling rate at each point, $\frac{dT}{dt}$ of the phase front.

$$\frac{dT}{dt} = \nabla T \times v_{phase} \tag{3.1}$$

By controlling the factors above, crystal structure of the newly formed solid can be controlled. Therefore, thermal modelling of melt growth processes such as laser annealing of thin semiconductor film [58] and Czochralski method for wafer production [59] had been carried out to find ways to better control these factors.

doi:10.6342/NTU202204042

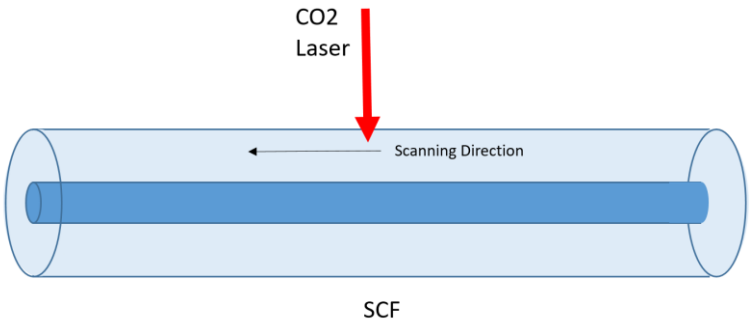

Fig. 3-1 CO2 laser annealing of SCF

In CO2 laser annealing of SCF, CO2 laser is used as heat source to melt the silicon core and polycrystalline core is recrystallized into single crystal or large grain polycrystalline structure. The laser is scanned along the axial axis of the fiber so the phase front move along the axial axis and new recrystallized structure is formed behind the phase front (Fig. 3-1). The whole length of silicon core in SCF can be transformed into a new crystal structure after laser scanning the whole fiber. Due to the relative new research in laser annealing of semiconductor fibers, no work on thermal modelling of SCF using CO2 laser have been reported. Therefore, we decided to carry out the modelling ourselves to better understand how do the annealing parameters such as laser beam size, power, scanning speed and fiber geometry influence the temperature profile during annealing to better control the recrystallization process. Findings from the thermal modelling is verified experimentally using a new set-up we built for the annealing experiment.

doi:10.6342/NTU202204042

3.1.2 Thermal Simulation of CO2 Laser Annealing Process

3.1.2.1 Geometry and Material

The geometry of SCF is built using a finite length 2D plane symmetry model (Fig. 3-3). The core diameter, d_{core} and cladding diameter, d_{clad} is part of the variable and range from 10 to 20 μm for d_{core} and 125 to 175 μm for d_{clad}. The length of the SCF is 10 mm with infinite element domain at both ends of the SCF to simulate an infinitely long fiber, The materials used in this model are solid fused silica, solid silicon and liquid silicon. As the laser annealing process is a melt growth process, the silicon core is modelled as a two-phase material and the set of parameters for modelling silicon changes depending on its temperature. The latent heat of fusion during the transition from solid into liquid above melting temperature is considered as well. The parameters used in this model are source from reference or directly from COMSOL's material library as listed in Table 3-1. The parameters used are mainly for heat flow physics which are thermal conductivity, density, heat capacity at constant pressure surface emissivity and latent heat of fusion.

doi:10.6342/NTU202204042

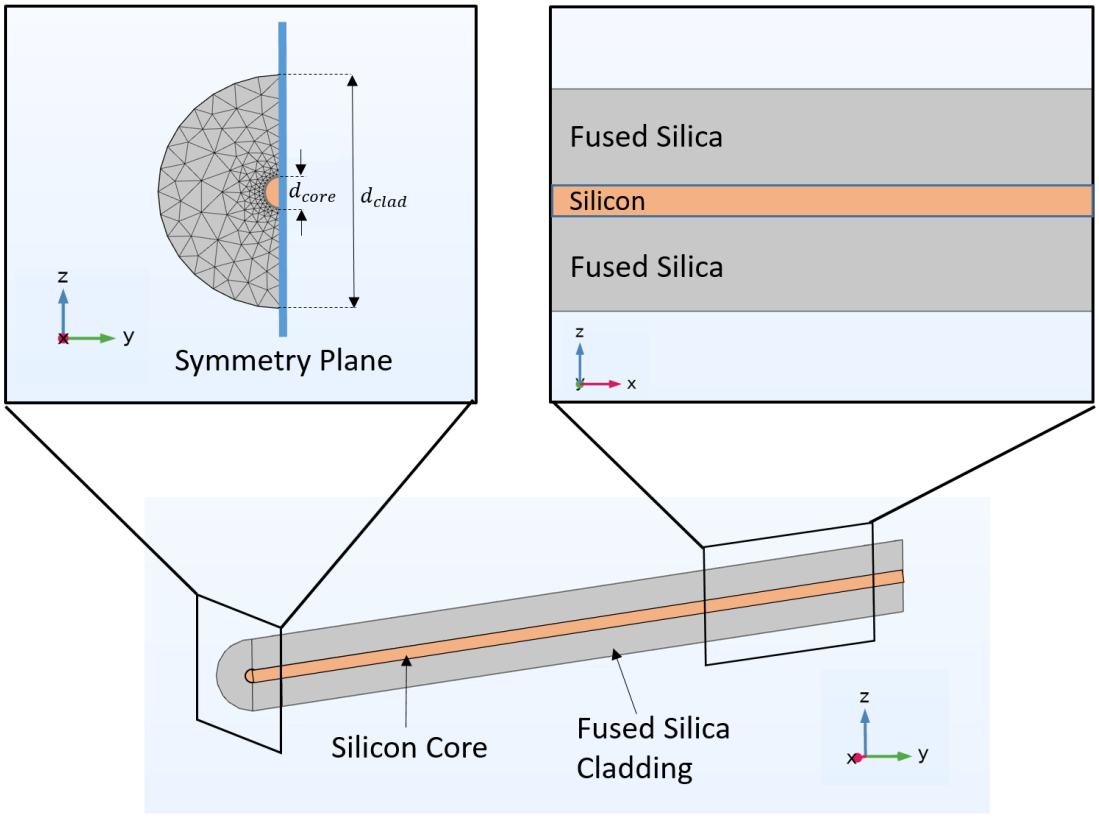

Fig. 3-2 The geometry and material used in COMSOL thermal modelling.

Silicon	Solid	Thermal Conductivity	[60]
		Density	COMSOL
		Heat capacity at constant pressure	[61]
		Surface emissivity	[62]
		Latent Heat of fusion	[63]
Silicon	Liquid	Thermal Conductivity	[64]
		Density	[64]
		Heat capacity at constant pressure	[64]
		Surface emissivity	[65]

doi:10.6342/NTU202204042

Fused Silica	Solid	Thermal Conductivity	[66]
		Density	COMSOL
		Heat capacity at constant pressure	[67]
		Surface emissivity	[68]

Table 3-1 List of material parameters and their reference.

3.1.1.2 Thermal Model: Governing Equations and Boundary Conditions

In our CO2 laser annealing model, four forms of heat transfer are considered. These include heat conduction between solid fused silica, solid and liquid silicon, surface radiation from both the surface of the fused silica cladding and silicon core, heat convection due to air circulation around the fiber and absorption of CO2 laser power through the cladding. However, convection in the liquid silicon is not considered as the volume of liquid silicon is so small for convection effect to take place.

The equations for heat conduction and surface radiation are same as those elaborated in section 2.6.2, which are from Eq. (2.2) to Eq. (2.6). The heat convection due to air circulation is modeled as heat flux, Q flowing out from the surface of the fiber [43].

$$Q = h(T - T_{ext}) \tag{3.2}$$

where h is the heat conduction coefficient, T is the temperature of the surface, T_{ext} is the ambient temperature. Due to small size of the fiber, the heat convection coefficient is less dependent on the thermal conductivity of the fiber but on the geometry of the

doi:10.6342/NTU202204042

fiber [69]. A value of 65 W $m^{-2}k^{-1}$ is used for all dimension of fiber in our simulation (Fig. 3-2).

The CO2 laser is modeled as a parallel radiative beam with Gaussian distribution. The intensity, $I(r)$ can be expressed as [53]:

$$I(r) = \frac{2P_o}{\pi w_o^2} e^{\frac{-2r^2}{w_o^2}} \tag{3.3}$$

where w_o is the beam radius and P_o is the power of the CO2 laser beam.

The absorption coefficient of fused silica cladding on CO2 laser (wavelength 10.6 μm) is $6 \times 10^4\ m^{-1}$ while silicon does not absorb at this wavelength. The laser is modeled to scan the SCF at constant speed, v_{phase} axially along the SCF. All the physics are than coupled together through the multi-physics solver and a time dependent solution is obtained. The solution reached steady-state at about 0.5 s into the simulation. Therefore, all results are based on solution at 1 s.

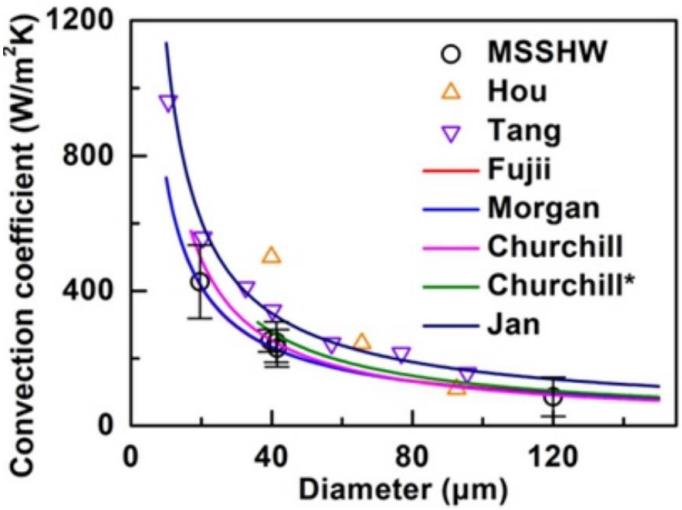

Fig. 3-3 Convection coefficient for wire at micron size. The coefficient is dependent on geometry rather than thermal conductivity of wire material [69].

doi:10.6342/NTU202204042

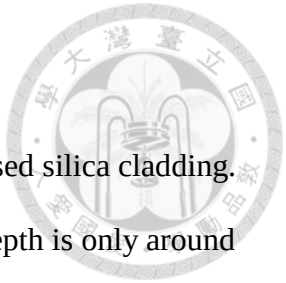

3.1.1.3 Results

Fig. 3-3 shows the intensity of the laser as it penetrates the fused silica cladding. Due to the high absorption of fused silica cladding, the penetration depth is only around 20 μm. Fig. 3-4 shows the temperature distribution inside the cladding and core when CO2 laser is scanned across the SCF axially. Because the heat of CO2 laser is speeded from the edge of the cladding to the core, the temperature in the core is more diffused. The axial plane across the silicon core is basically isothermal compared to the silicon core annealed using the 488nm laser where the surface facing the laser has higher temperature (Fig. 3-6). The inset in Fig 3-5 shows the temperature along the axial axis of the silicon core. The side where the laser is moving towards has larger temperature gradient and the opposite side has lower temperature gradient, forming a tail like temperature distribution. Fig. 3-7 shows the phase of silicon core during annealing which is dependent on its temperature.

As the speed of scanning increases, peak temperature of the silicon core decreases while the length of heated region expands (Fig. 3-9). The temperature gradient along the axial axis is plotted in Fig. 3-9. The gradient at the side where the laser scan towards increases with scanning speed while the gradient at the opposite decreases. By multiplying the temperature gradient with the scanning speed, we can calculate the cooling rate at every point in the silicon core.

Cooling rate at the phase front is key for large grain size after recrystallization in SCF [16]. Therefore, our effort is focused on how laser beam radius, w_o, laser power, P_o, cladding diameter, d_{clad} core diameter, d_{core} and scanning speed, v_{phase} influence the cooling rate at the phase front. The phase front behind the laser during scanning is our area of interest as it is the place where solidification and recrystallization occurs.

doi:10.6342/NTU202204042

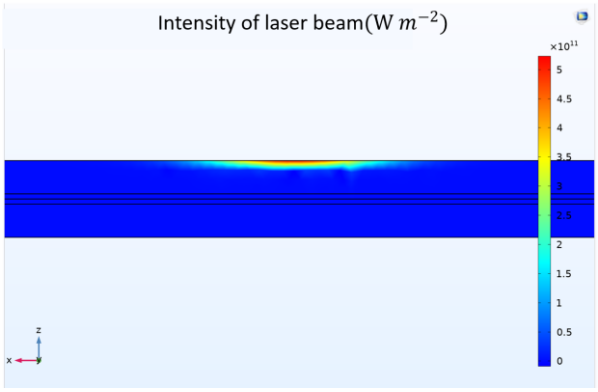

Fig. 3-4 Intensity of laser beam passing through fused silica cladding.

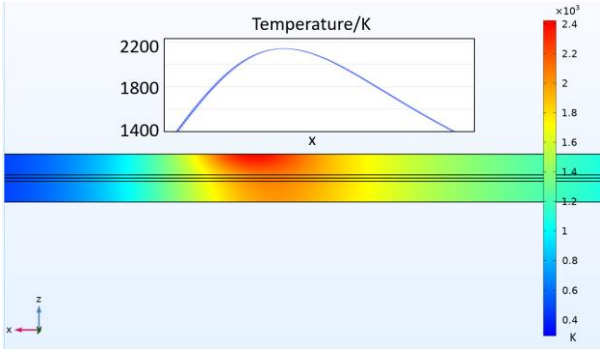

Fig. 3-5 Temperature distribution of fused silica cladding and silicon core when CO2 laser is scanned axially on the SCF. (Inset) Temperature along the axial axis of silicon core.

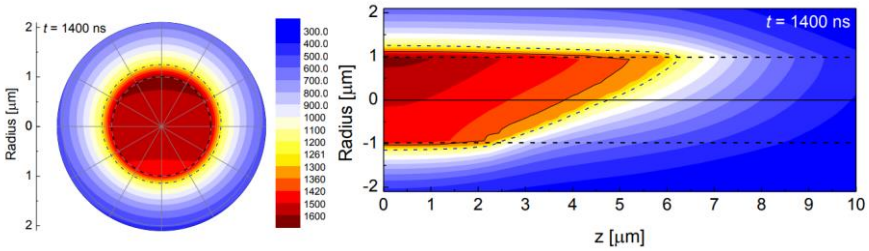

Fig. 3-6 Temperature distribution of fused silica cladding and phase of silicon core. Above melting point, solid silicon (Black) changes to liquid silicon (White).

doi:10.6342/NTU202204042

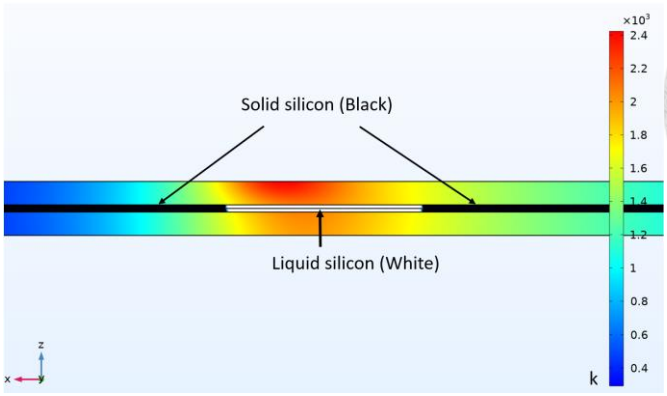

Fig. 3-7 Temperature distribution of fused silica cladding and phase of silicon core. Above melting point, solid silicon (Black) changes to liquid silicon (White).

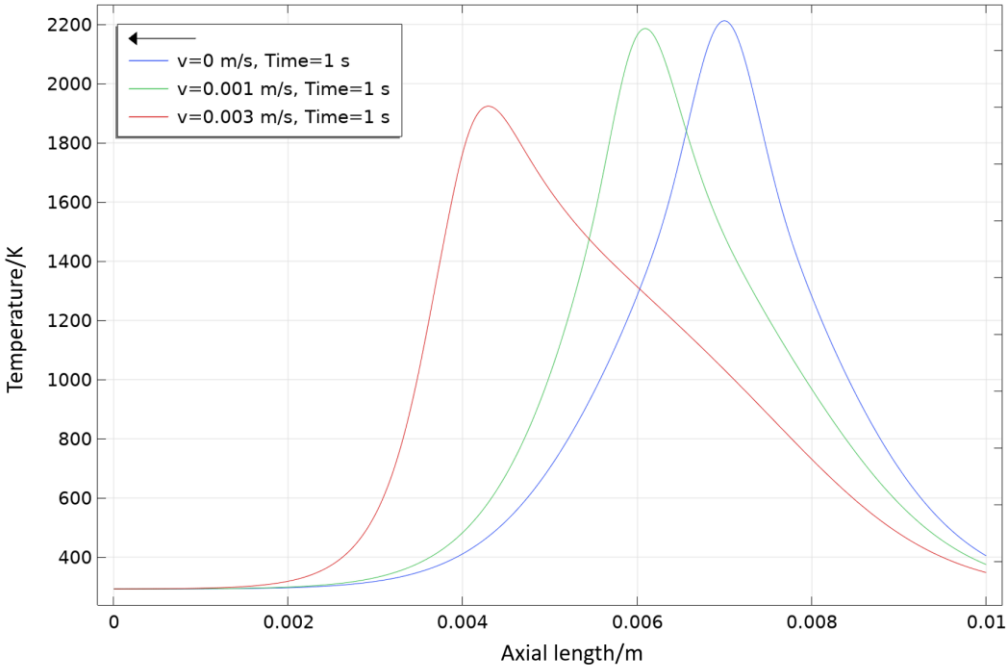

Fig. 3-8 Temperature along the axial axis of silicon core at different laser scanning speed. Laser scans towards the left as shown in the arrow in the legend.

doi:10.6342/NTU202204042

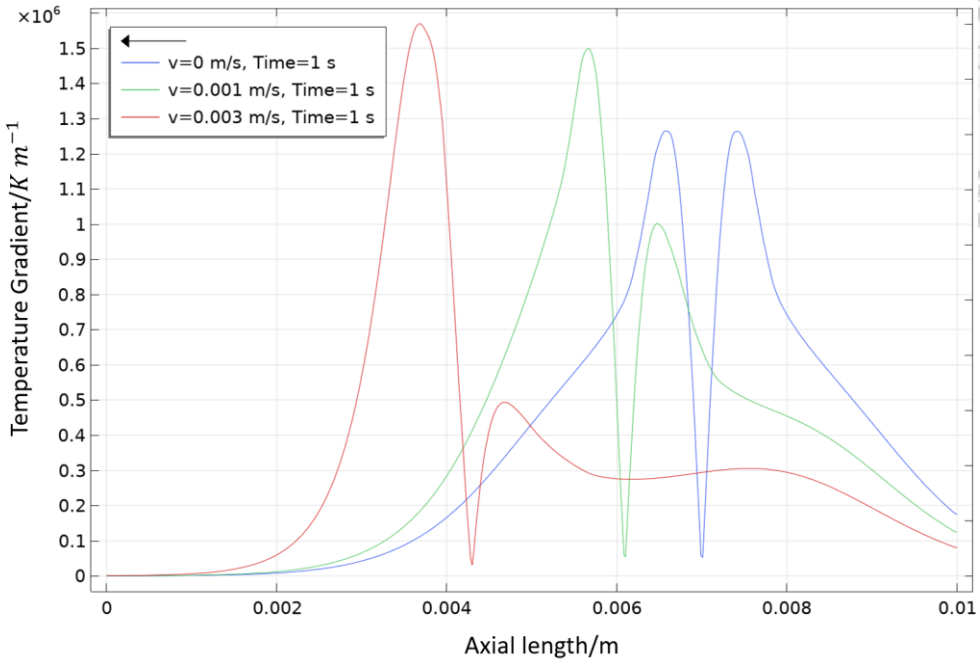

Fig. 3-9 Temperature gradient along the axial axis of silicon core at different laser scanning speed. Laser scans towards the left as shown in the arrow in the legend.

Power

Fig. 3-10 and Fig. 3-11 shows the cooling rate at different scan speed at different laser power for two beam radiuses. Cooling rate is only affected by laser power at higher scan speed. At lower scan speed, the cooling rate is pretty much the same for laser power between 3-9W. The effect is more obvious for larger beam radius.

Beam radius

Fig. 3-12 shows the cooling rate for different beam radiuses. Very surprisingly, the beam radius does not affect the cooling rate very much. Maybe this is because the heat is spread from the cladding to the core and the heat flux from the hot spot is diffused out and the effect of the boundary of the laser becomes less obvious.

doi:10.6342/NTU202204042

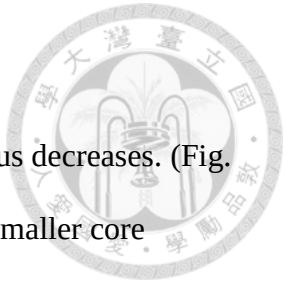

Cladding and core diameter

Cooling rate increases when the cladding radius and core radius decreases. (Fig. 3-13 & Fig. 3-14). The magnitude of the increase in cooling rate for smaller core diameter is less than for smaller cladding diameter. Also, for smaller core diameter, the increase in cooling rate is similar for all scanning speed while for smaller cladding diameter, the increase in cooling rate is more evident for high scan speed.

Constant peak temperature

Fig. 3-15 explores a combination of annealing parameters that produce the same peak temperature. It seems that the cooling rate is different for different combination although all of them produces the same peak temperature. Therefore, peak temperature is not an indicator for cooling rate.

Temperature distribution at same cooling rate

Fig. 3-16 shows the temperature distribution during annealing with 3 different parameters but same cooling rate. We can see that the temperature distribution is quite different where SCF annealed using highest power (9 W) and smallest radius (250 μm) laser has highest peak temperature and largest melt pool length. Laser with similar power but larger radius produces lower peak temperature and smaller melt pool length while laser with lower power and smaller radius produce peak temperature just enough to melt a very short length of silicon.

Conclusion

From all results above we can see that the scan speed is the most crucial factor in changing the cooling rate. However, the effect of scan speed in increasing cooling rate slightly plateau at high scan speed. Although we can achieve same cooling rate for

doi:10.6342/NTU202204042

many different combinations of parameters, there are also other factors to be considered such as the melt region length and peak temperature in the melt region. For longer length of liquid with lower viscosity, the effect of Rayleigh Instability increases and the stream of liquid will break down into shorter length of liquid. This effect can be seen in term of droplet formation and cladding deformation when the temperature is very high (Fig. 3-17). This is due to the fact that the viscosity of the glass and silicon decreases at higher temperature. Therefore, if temperature gradient or temperature does not play a role in grain size during recrystallization (investigation is needed), using a smaller laser beam radius at lower power while scanning at high speed is desirable for high cooling rate and high structure integrity of the SCF.

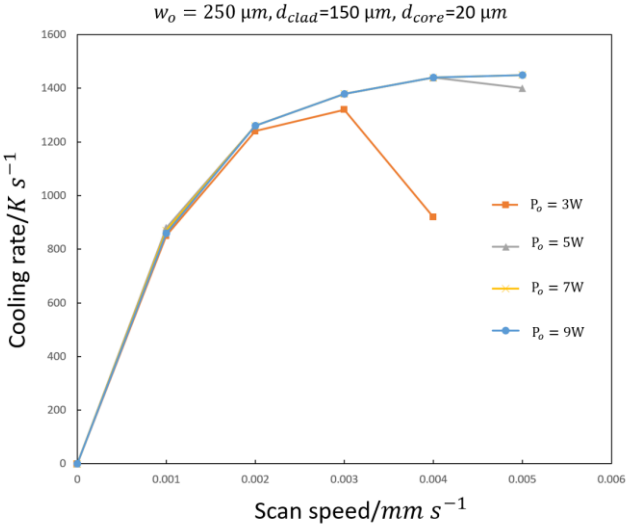

Fig. 3-10 Cooling rate versus scan speed for different laser power, P_o for $w_o = 250\ \mu m$.

doi:10.6342/NTU202204042

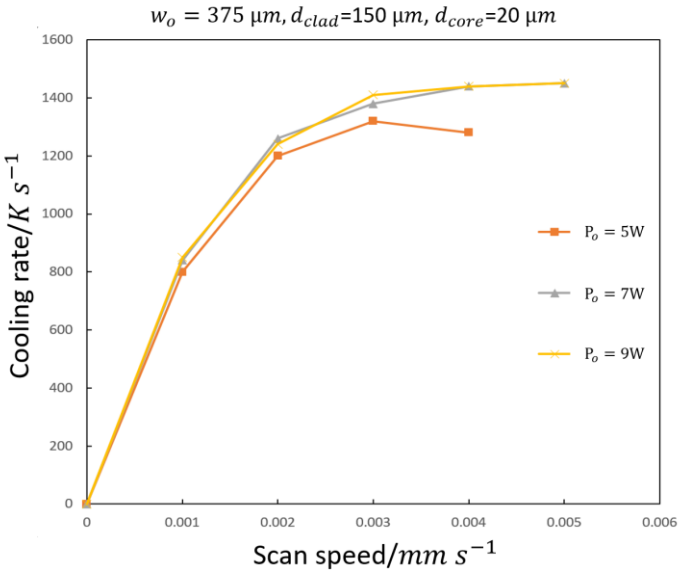

Fig. 3-11 Cooling rate versus scan speed for different power , P_o for $w_o = 375\ \mu m$.

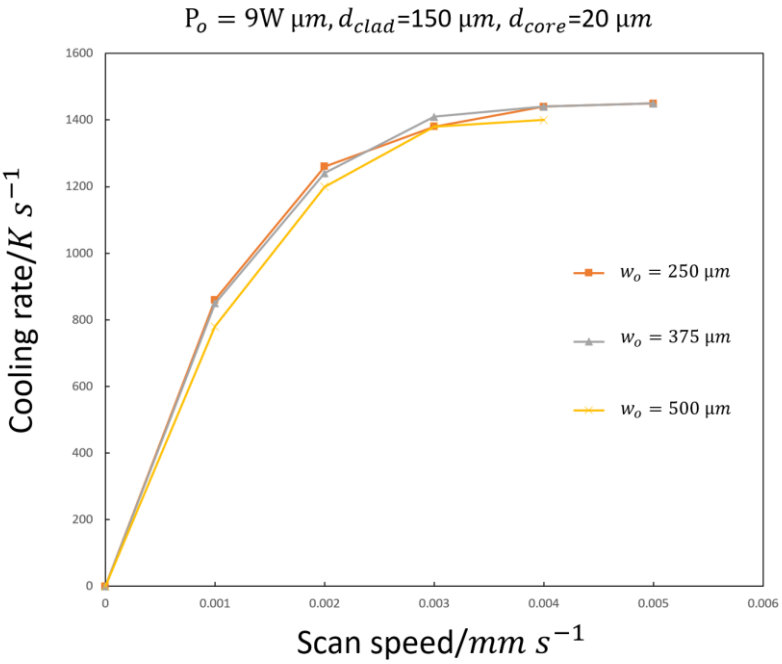

Fig. 3-12 Cooling rate versus scan speed for different beam radius, w_o.

doi:10.6342/NTU202204042

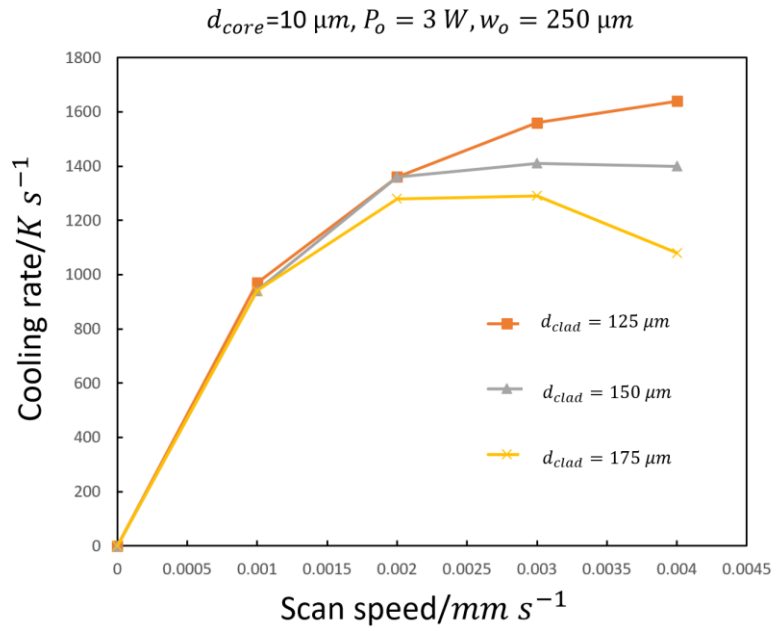

Fig. 3-13 Cooling rate versus scan speed for different cladding diameter, d_{clad}

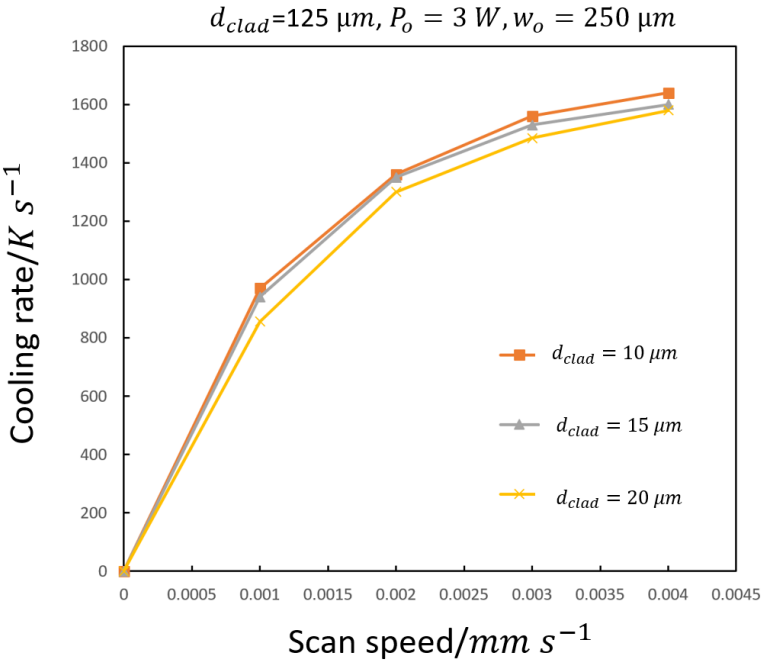

Fig. 3-14 Cooling rate versus scan speed for different core diameter, d_{core}.

doi:10.6342/NTU202204042

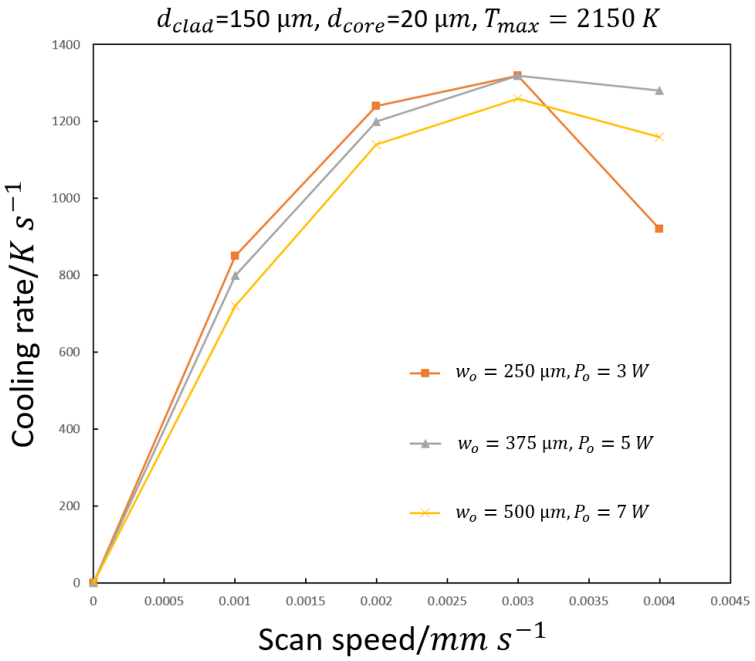

Fig. 3-15 Cooling rate versus scan speed at different condition with same peak temperature.

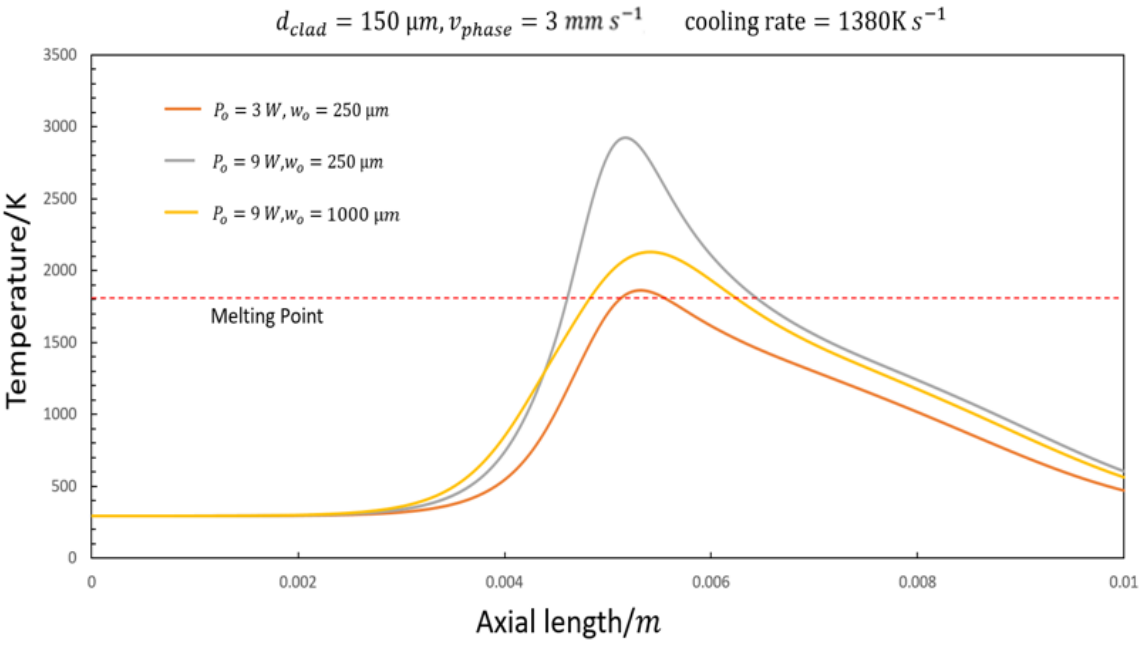

Fig. 3-16 Temperature distribution at different annealing conditions with same cooling rate.

doi:10.6342/NTU202204042

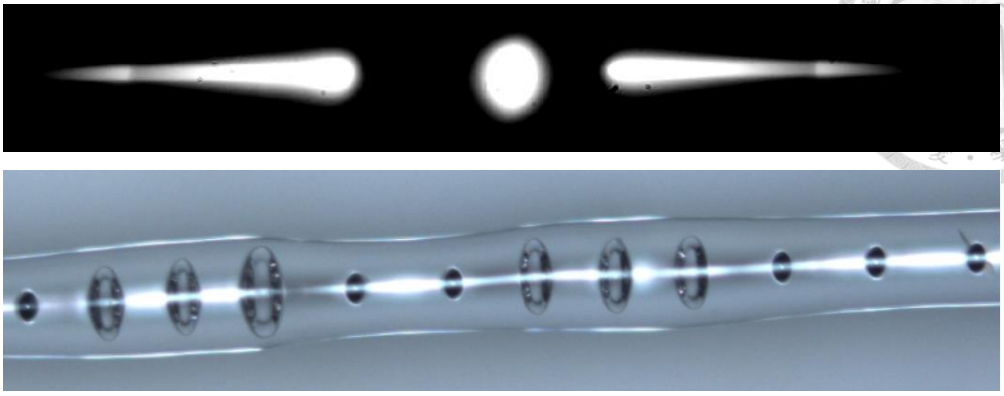

Fig. 3-17 (Top)Breakup of silicon core in to droplets due to Rayleigh Instability.

(Bottom) Change in shape of fused silica cladding when laser power is too high.

doi:10.6342/NTU202204042

3.1.3 CO2 Laser Annealing Experiment

3.1.3.1 Previous Set-up

Previously, our lab had chosen to use CO2 annealing method to improve the quality of our fiber. A 10W PWM laser (Synrad 48-1W) with a focal length of 10mm is used as our source. It is paired with a motorized stage to move the SCF along the focal point of the CO2 laser beam. The fiber is aligned to the center of the CO2 laser beam by using an alignment red laser that shares a beam path with the CO2 laser. The alignment is done with eyes which result in misalignment of SCF from the center of the CO2 laser beam. This would cause a change in power absorbed by the SCF. Also, due to the short focal length of the lens in our system, a slight change of position along the laser beam axis would also cause a change in the absorbed power as well. Both of these would causes changes in SCF's temperature distribution

3.1.3.2 New Set-up

In the new laser annealing set-up, the same CO2 laser with lens of 101 mm focal length is used instead. Improvement on the fiber aligning system and temperature monitoring system is done to better understand the annealing process. As we need to keep the fiber at the center of the laser beam and at fixed distance from the focal point during the laser, a two-axis aligning system is needed. An optical microscope is used for this application. The depth of focus is used to align the fiber to the laser beam center while the normal vision is used to align the fiber at a fix distance from the laser's focal point. The focal point of the microscope is aligned with the center of the laser beam so that if the SCF is aligned to the focus point of the microscope, it is aligned with the center of the laser beam as well. A MATLAB GUI is written to help align the fiber (Fig. 3-18). The

doi:10.6342/NTU202204042

sharpness of focus is detected through the contrast at the edge. A figure to indicate high contrast is shown on the Focus bar in the GUI, where higher figure indicates higher contrast. A line is place in the middle of the GUI screen. Before annealing, we need to check that when the SCF translate, the middle of the core must always cuts through the line so that the moving SCF is always at a fixed distance from the laser's focus point. If not, a 4-axis micro stage system is used to realign the SCF. The whole system is shown in Fig. 3-19. This same microscope is used as a temperature monitoring system as well and the theory behind it will be discussed in the next section.

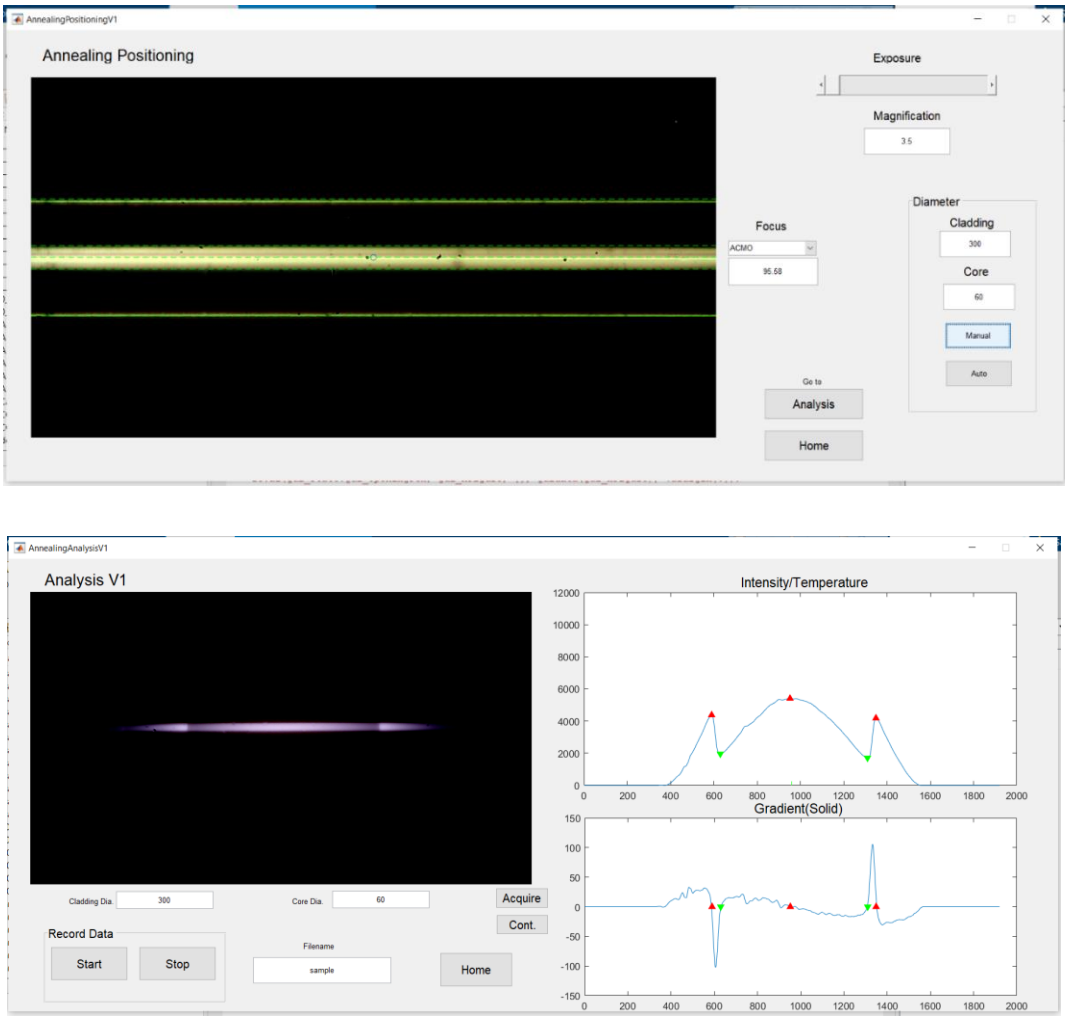

Fig. 3-18 (Above) MATLAB GUI for aligning fiber. (Below) MATLAB GUI for monitoring temperature through radiation power.

doi:10.6342/NTU202204042

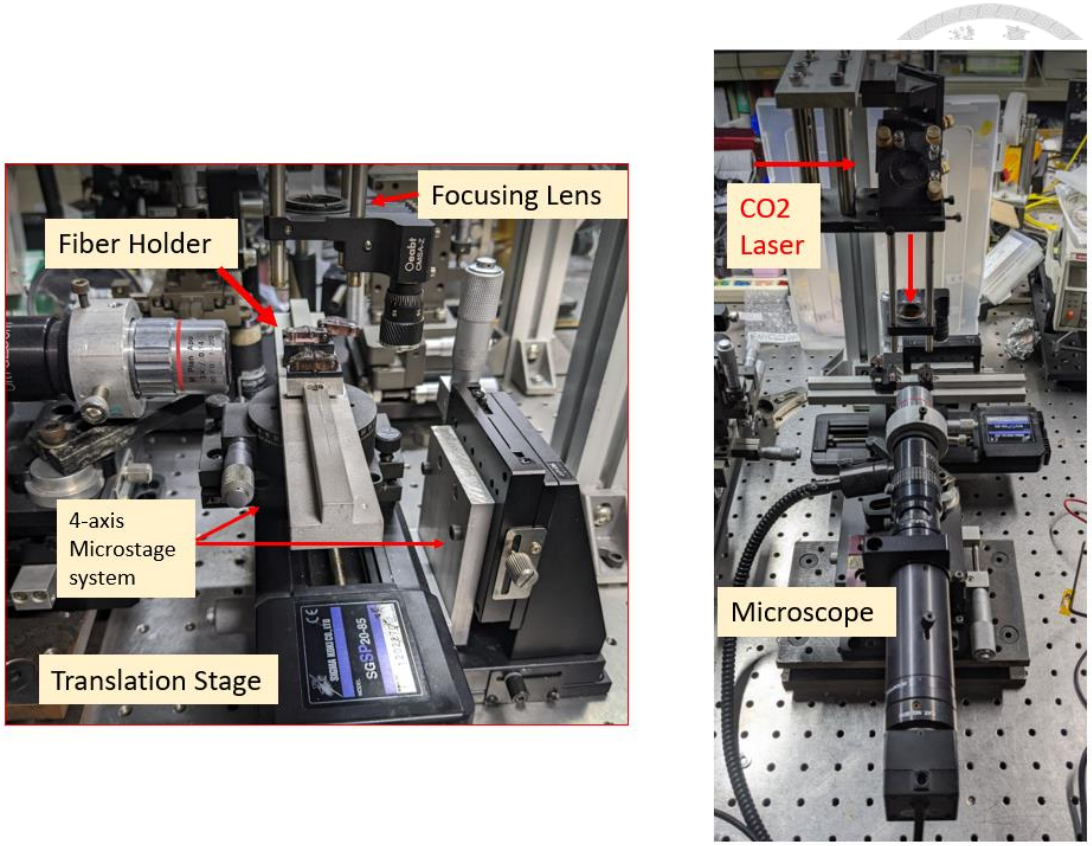

Fig. 3-19 CO2 Laser Annealing Set-up

3.1.2.3 Temperature Monitoring

The temperature monitoring method used here is proposed by Nealy's group [16] which monitors the power of black-body radiation from the silicon core along the axis of SCF using a visible camera at the end of the microscope. As the cladding of SCF is transparent at the visible region (near zero absorptivity), the radiation emitted from the silicon core can be transmitted through the cladding and then captured by the camera. The radiation measured using the camera, although passed through the cladding is purely from the silicon core as according to Kirchhoff's law of thermal radiation, the emissivity is equal to the absorptivity at a given wavelength. Therefore, the cladding does not emit radiation at visible region and does not contribute to the radiation

doi:10.6342/NTU202204042

captured by the camera. The measured power of the radiation is then converted into temperature value based on Planck's law.

According to Planck's law, a black body with temperature T emits electromagnetic radiation with spectral radiance, *B* which describes the spectral emissive power per unit area, per unit solid angle, per unit wavelength:

$$B_\lambda(\lambda, T) = \frac{2hc^2}{\lambda^5} \frac{1}{\exp\left(\frac{hc}{\lambda k_B T}\right) - 1} \tag{3.3}$$

where k_B is the Boltzmann constant, *h* is the Planck constant, *c* is the speed of light in the medium and λ is the wavelength of radiation. As we are using a visible camera to measure the radiation from the silicon core, the power measured by each pixel is equal to the surface emissivity multiply by the spectral radiance integrated over a spectrum of visible wavelength, called the band radiance, $B(T)$

$$B(T) = \int B_\lambda(\lambda, T) d\lambda \tag{3.4}$$

and then integrated over the solid angle, Ω and area captured by each pixel in the camera, P1 (Fig. 3-20). Ω is equal to the field of view of the camera system, so not all radiation is captured by the sensor. Although the temperature across the plane in the silicon core normal to the core's axial axis, S is constant as shown in the thermal modeling, the power measured at different area along surface of the plane, for example P1 verses P2 is different. This is because the angle of surface in each area is different. As a surface can only radiates in the forward direction, at area with large angle difference between the surface's normal vector and the camera sensor's normal vector such as at P2, less power can be captured by the sensor as the intersection of the light emission cone of the surface and light receiving cone of the sensor decreases (Fig. 3-

doi:10.6342/NTU202204042

21). The radiation from the silicon core captured by the camera is shown in Fig. 3-22 and the edge of silicon core can be seen darker than the center region. As we are only interested in the axial distribution of the temperature, the power capture along the x-axis of the silicon core which is from plane with same temperature is integrated into a single value to get a power versus Z axis graph (Fig. 3-22). Through this method, we can also lower the noise of the data by averaging them out.

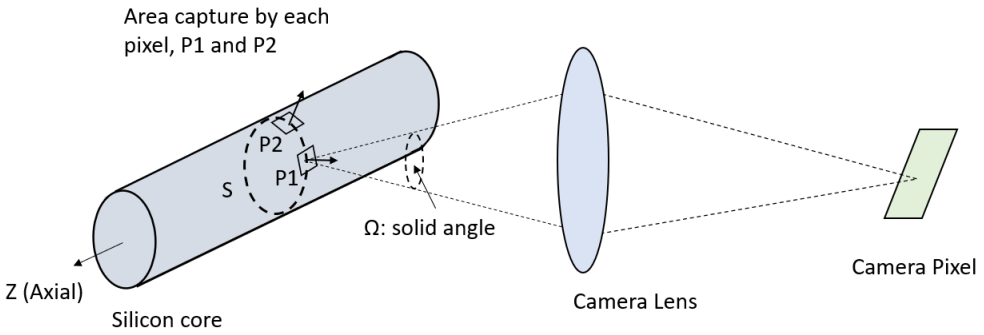

Fig. 3-20 Radiation from the silicon core captured by camera pixel.

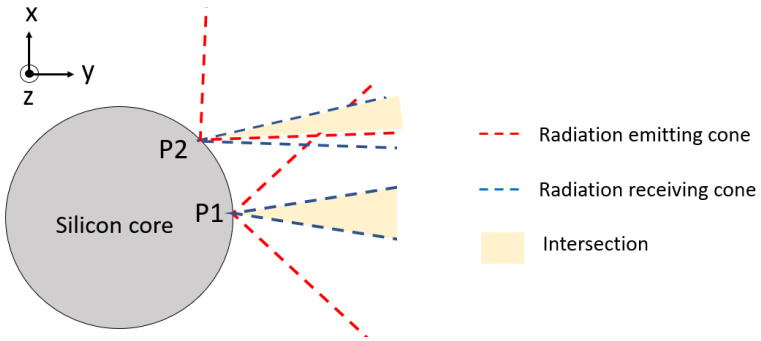

Fig. 3-21 Amount of radiation depends of the intersection of emission light cone from silicon and receiving light cone from the camera pixel.

doi:10.6342/NTU202204042

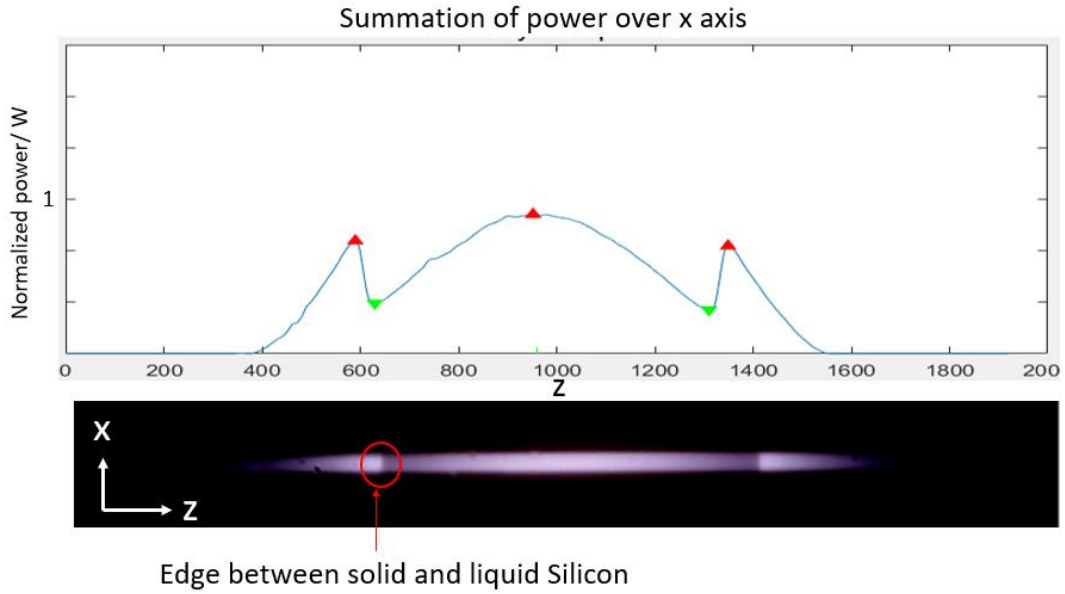

Fig. 3-22 (Bottom) Image of the radiation of the silicon captured by the camera. (Above) Summation of power along x-axis.

With A being the area along the surface of S-plane at the side of the camera, Ω the solid angle of the radiation captured by the camera, ε the surface emissivity of silicon, the power along the z-axis can be expressed as:

$$P(Z) = \varepsilon \int_{\Omega} \int_{A} \int_{475\ nm}^{600\ nm} B_{\lambda}(\lambda, T_1) d\lambda\ dA\ d\Omega \tag{3.5}$$

$$= \varepsilon \int_{\Omega} \int_{A} B(T_1) dA\ d\Omega$$

The wavelength spectrum for band radiance in our experiment is assumed to be from 475 nm to 600 nm based on the responsivity curve of the sensor as only the power measurements form the green filtered pixel in the color camera is used (Fig. 3-23).

To convert the power into temperature, reference point is needed where we know the power $P(Z_1)$ and the temperature, T_1 at that position, Z_1. To find the

doi:10.6342/NTU202204042

temperature, T_2 at the other position Z_2, we can substitute both sets of values into Eq. (3.5) and compare them together. We will get a ratio of power at both positions as ratio between the integration of band radiance at both points. However, as the S plane at every point on the z axis of the silicon core has the same geometry, A and Ω will be the same. We can therefore eliminate the integration from Eq. (3.5) making the ratio of power at both points the ratio of band radiance at the temperature at both points:

$$\frac{P(Z_1)}{P(Z_2)} = \frac{\varepsilon_1 \int_\Omega \int_A B(T_1) dA\, d\Omega}{\varepsilon_2 \int_\Omega \int_A B(T_2) dA\, d\Omega} = \frac{\varepsilon_1 B(T_1)}{\varepsilon_2 B(T_2)} \qquad (3.6)$$

Due to the difference in surface emissivity of solid and liquid silicon, a clear dark line can be seen at the edge of the molten silicon (Fig. 3-22). As we know the melting point of silicon is 1688 K, we can use the power measured at the edge of the molten silicon region as reference and using Eq. (3.6) to deduce the temperature at other points. The calculated band radiance B(T) for temperature between 1200 K to 2000 K for black body (emissivity = 1) between 475 nm and 600 nm can be obtained from the website (www.spectralcalc.com) and is shown in Fig. 3-24 (Left). The inverse of B(T) is shown in Fig. 3-24 (Right) where T is expressed as a polynomial of $\ln\big(B(T)\big)$ Eq. (3.7).

$$T = 0.3088 * [\ln(B(T))]^3 + 3.461 * [\ln(B(T))]^2 + 69.75 * \ln\big(B(T)\big) + 1340 \qquad (3.7)$$

doi:10.6342/NTU202204042

The total power measured by the camera at the pure solid region, P_1 and pure liquid region P_l is given by:

$$P_m(T) = a\varepsilon_s B(T) \quad (3.8a)$$

$$P_l(T) = a\varepsilon_l B(T) \quad (3.8b)$$

Where ε_s is the surface emissivity of solid silicon, ε_l is the surface emissivity of liquid silicon, a is the efficiency of the camera. At the region with solid and liquid mixture, we do not know the surface emissivity. However, it is in this region where solidification occur and we want to find the temperature gradient there. Assuming P1, edge of solid region has temperature of 1687 K, we can find a. With information about a, we can find B(T) at other point in the pure liquid and pure solid region Eq (3.9) and Eq. (3.10). B(T) can then be convert to temperature using Eq. (3.7). The temperature gradient at mixed solid liquid region is the average of the temperature gradient at P1 and P2. This is based on the assumption that the temperature curve is differentiable and continuous along all region.

$$\mathrm{a} = \frac{P1}{\varepsilon_s B(1687\ K)} \quad (3.9)$$

$$B(T) = \frac{P}{a\varepsilon_s} \quad \text{(Pure solid region)} \quad (3.10a)$$

$$B(T) = \frac{P}{a\varepsilon_l} \quad \text{(Pure liquid region)} \quad (3.10b)$$

doi:10.6342/NTU202204042

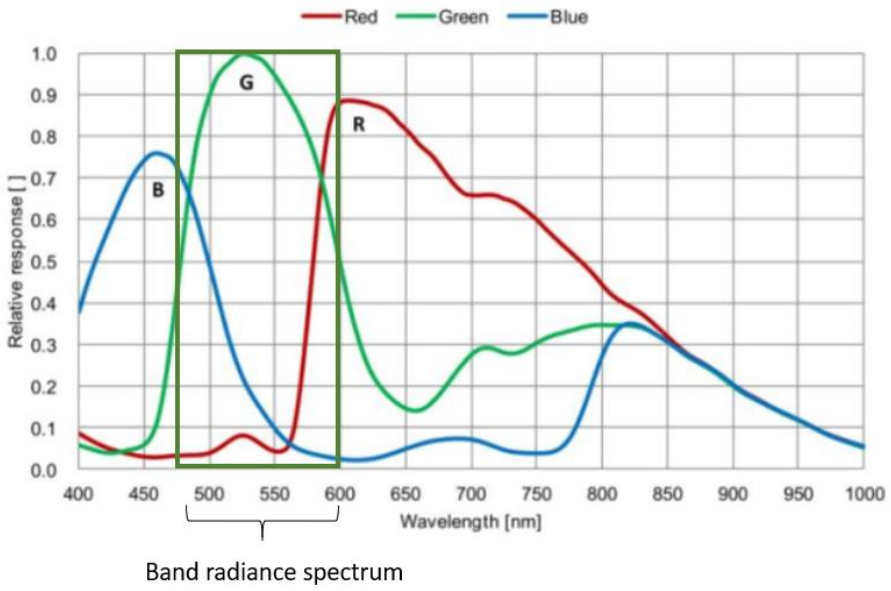

Fig. 3-23 Responsivity of sensor.

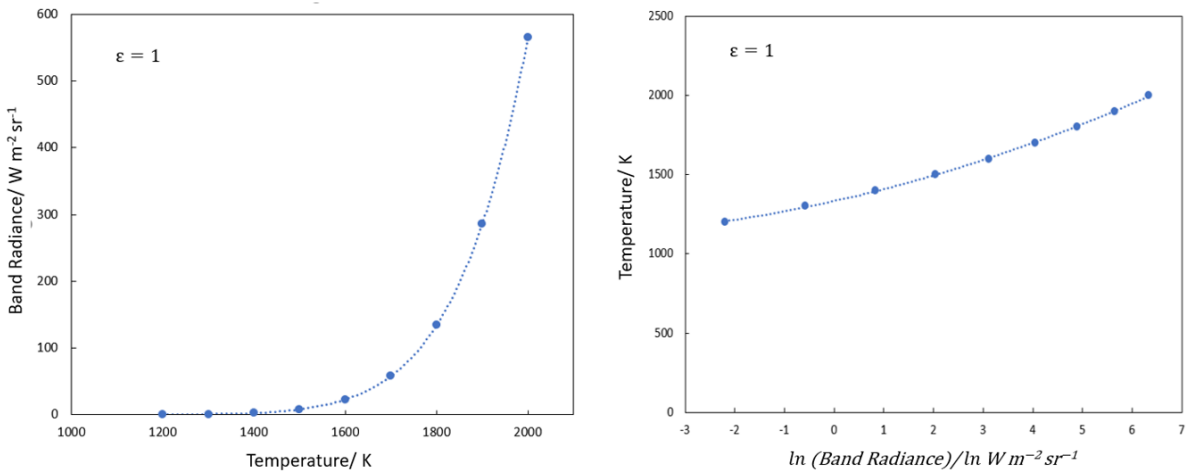

Fig. 3-24 (Left) Band radiance against the blackbody temperature. (Right) Temperature against $\ln(B(T))$.

doi:10.6342/NTU202204042

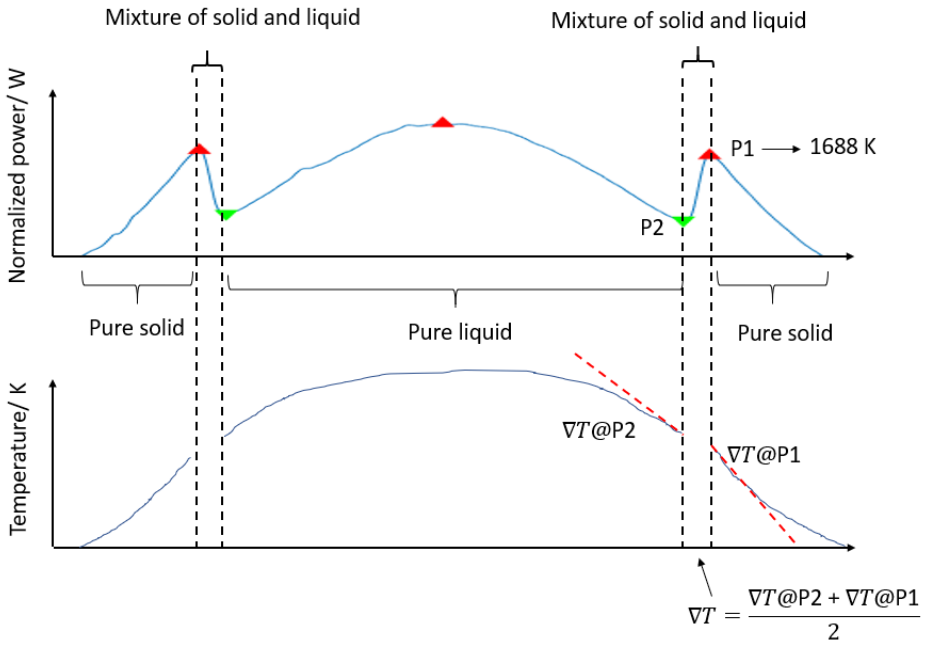

Fig. 3-25 (Above) Identifying the phase of silicon based on radiation characteristics. (Below) Finding temperature gradient at the mix solid liquid region.

3.1.2.4 Results

Fig. 3-25 shows the conversion between radiation power to temperature. Note that this way of temperature conversion is only accurate near the edge of phase front because we only know the temperature near the phase front. Thus, the surface emissivity we use would be accurate only in that small temperature region as surface emissivity changes with temperature. We do not have enough information to calculate the true peak temperature. In all the experiments, laser power of 1.5 W, laser beam radius of 400 μm, scan speed of 1.5 mm s^{-1}, core diameter of 30 μm, cladding diameter of 150 μm is used if not otherwise stated. Generally, the experiment results agree with the trend shown in the thermal modeling result. The cooling rate shows greatest increase with increase in scan speed (Fig. 3-27). The increase of laser power also increases the cooling rate (Fig. 3-28). On the other hand, increase in cladding and core diameter

doi:10.6342/NTU202204042

causes a decrease in cooling rate (Fig. 3-29 & Fig. 3-20). The cooling rate calculated is similar in magnitude but slightly lower than those calculated using the thermal modeling. However, the laser power used in the experiment is quite low (1.5W) and at this power level, the silicon core does not melt in the thermal model. Some possible explanation is that the material parameters are sourced from paper and not tested using our own material. More experiment is needed to calibrate our thermal model with the experimnet. All in all, the thermal model can still provide a direction for tuning the annealing parameters.

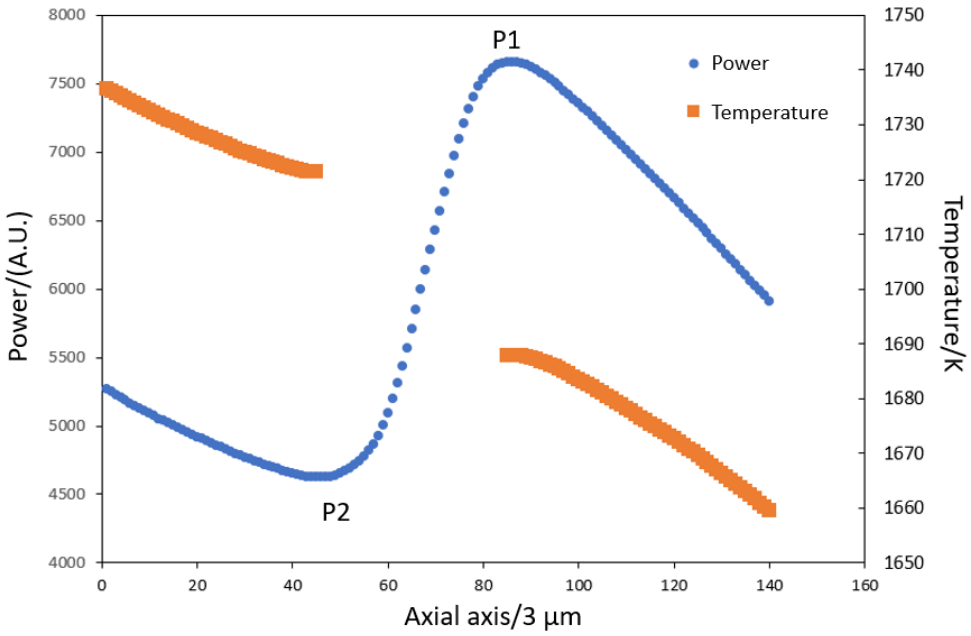

Fig. 3-26 (Left Axis) Radiation power at the phase front. (Right Axis) Conversion of radiation power to temperature based on method in section 3.1.2.3

doi:10.6342/NTU202204042

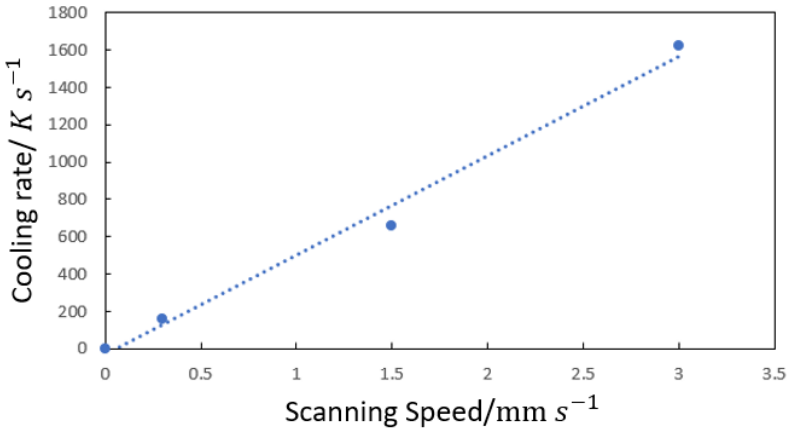

Fig. 3-27 Cooling rate against scan speed.

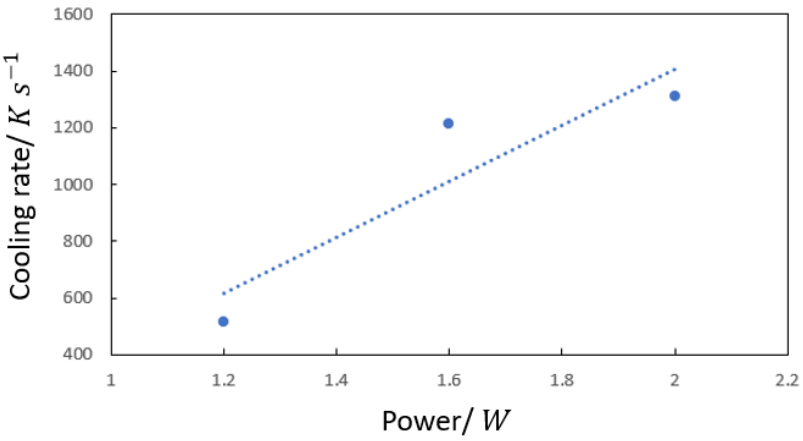

Fig. 3-28 Cooling rate against laser power.

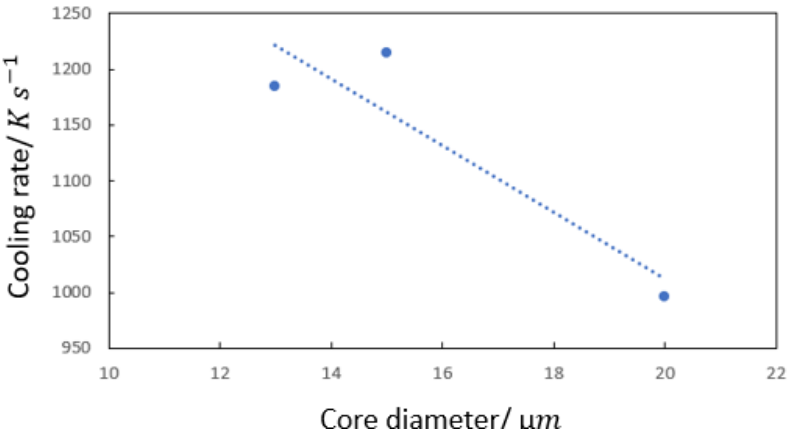

Fig. 3-29 Cooling rate against core diameter

doi:10.6342/NTU202204042

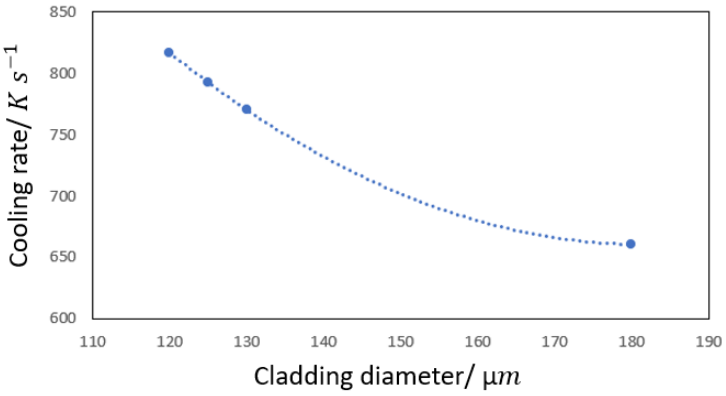

Fig. 3-30 Cooling rate against laser cladding diameter

doi:10.6342/NTU202204042

3.2 Single Mode Coupling and Transmission in Multimode SCF

3.2.1 Introduction

Due to the high refractive index of silicon, SCF with core diameter more than 380 nm shows multimode behavior. However, single mode transmission in multimode SCF is highly desirable. For non-linear use, lower mode is a better option as lower mode has high mode confinement and higher energy density to induce non-linear effects. Also, lower mode in smaller core fiber has energy higher density than same mode in larger core. Therefore, some groups use taper to reduce core size to induce non-linear effect [7]. For sensing purpose wise, optical modes in larger core have smaller evanescent field and would not be suitable for sensing purpose. Similar to non-linear usage, a taper can be used to reduce the core volume for better sensing performance. Generally, lower mode has larger critical tapering angle and therefore the whole fiber component can be design to be shorter if most energy travels in lower mode [70]. Furthermore, lower mode also has lower transmission loss [71]. Based on the advantage listed above, it seems that single mode coupling and transmission is highly desirable even in multimode SCF.

3.2.2 Single Mode Coupling

Due to the mode field difference between SMF and SCF, to couple light to single mode SCF requires a lens system [7]. Due to the small core size requirement for single mode SCF, there are no groups that are able to directly draw single mode SCF. So, we propose a method to directly splice a SMF to SCF, but still maintaining single mode propagation in SCF using mode matching [26] and central launching method [25].

doi:10.6342/NTU202204042

Mode matching method involves launching light with beam diameter similar to the mode of a fiber, as most of the light energy will couple to this mode and higher modes are not excited. As for central launching method, it involves matching the central axis of the single mode fiber to the axis of multimode fiber even though their core size don't match [25]. Based on these two methods, we will need to fabricate SCF with core diameter such that its fundamental mode matches the mode size of SMF. Fig. 3-31 shows the plot of mode coupling coefficient between fundamental mode of different core size and mode of an SMF (Corning SM-28) using central launching method. The optical power reflected from the edge of SMF and SCF is about 0.17, so for SCF with 15 μm core diameter, the coupling efficiency of 0.79 means most power is transmitted from the SMF to fundamental mode in SCF and only 4% of the power is coupled to higher mode. The coupling efficiency against mismatch between axis of SMF and SCF is plotted in Fig. 3-32. Even up to 2 um axis mismatches, the coupling efficiency is still at 0.68. It seems that single mode launching of SCF using SMF is viable with high tolerance if the core diameter of SCF is optimized.

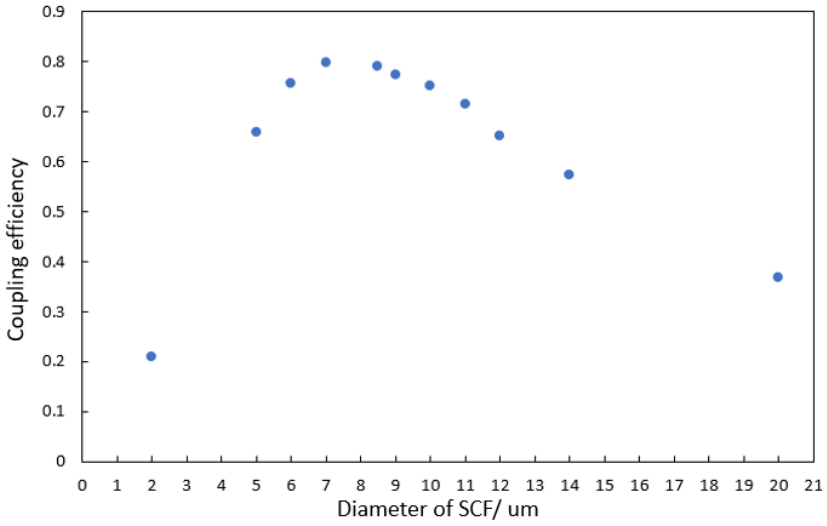

Fig. 3-31 Coupling efficiency of misaligned SCF with various core diameter to SMF

doi:10.6342/NTU202204042

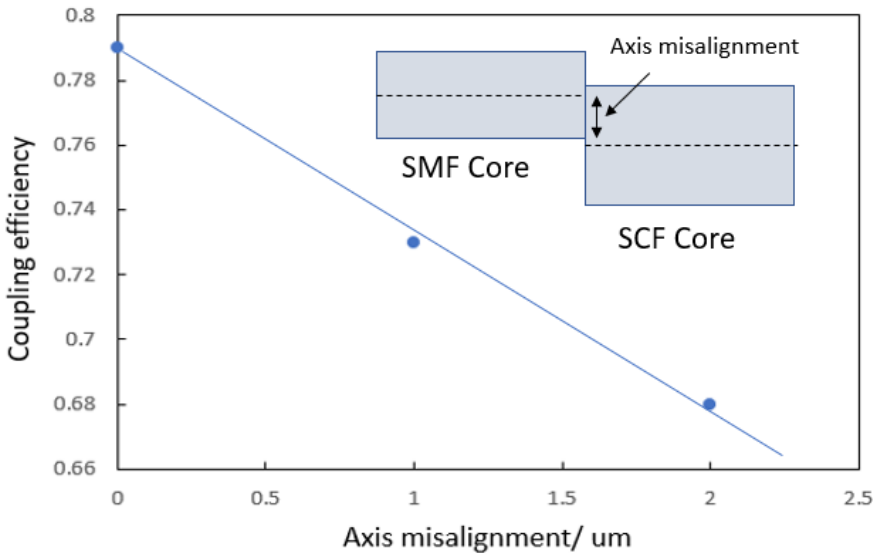

Fig. 3-32 Coupling efficiency of misaligned SCF with core diameter of 15 um and SMF

3.2.3 Mode Decomposition Algorithm

From previous section, we have discussed about our proposed method for coupling light into SCF which is the direct splicing of SMF with a mode matched SCF. In this chapter, we will implement an algorithm to monitor the mode in our SCF to accurately implement single mode coupling between SMF and SCF which convert this problem into linear equations and solve it with Moore-Penrose inverse matrix [72].

A few mode decomposition methods were published such as Gerchberg–Saxton technique [73], stochastic parallel gradient descent, [74]. Most of the methods need the intensity and phase information of the output except for the method proposed in [72] which only requires intensity information. Not only is the set-up required for this method simpler, due to the non-iterative nature of the algorithm, it is faster than other mode decomposition method if the mode number is kept reasonably small. This condition can be meet in our case if we are using single mode coupling method. Using a

doi:10.6342/NTU202204042

quicker mode decomposition method, each iteration of the fiber alignment can be done in a shorter amount of time speeding up the whole process of splicing.

3.2.3.1 Theory

The total transverse electric field in a fiber can be written as a summation of eigenmodes, E_n.

$$E(x,y) = \sum_n C_n E_n(x,y) \tag{3.11}$$

$$C_n = A_n\left(e^{i\varphi_n}\right) \tag{3.12}$$

where C_n is the complex coefficient of each eigenmode.

$C_n$contains a magnitude component, A_n and a phase component φ_n because the phase constant for all eigenmodes are different. After travelling for a distance along the fiber, all the eigenmodes will have phase difference between them at the output of the fiber.

The near field intensity, $\mathrm{I}(x,y)$ at the output of the fiber is the absolute value of the transverse electric field:

$$\begin{aligned} \mathrm{I}(x,y) &= \langle |E(x,y)|^2 \rangle \\ &= \sum_i \sum_j C_i C_j^* \, E_i(x,y) E_j(x,y) \end{aligned} \tag{3.13}$$

Assuming we are capturing the intensity with a camera with $p \times q$ pixels, we can discretize the whole equation by substituting x and y with p and q. $\mathrm{I}(p,q)$ and $E_n(p,q)$ can be arranged into matrix of size m x 1 , $\boldsymbol{I}_{m\times 1}$ and $\boldsymbol{E_{n,m\times 1}}$where $m = p \times q$.

doi:10.6342/NTU202204042

Each element in $\boldsymbol{I}_{m\times 1}$, I^k and each element in $\boldsymbol{E}_{\boldsymbol{n},m\times 1}$, $E_n^{(k)}$ can be map to $\mathrm{I}(p,q)$ and $E(p,q)$using the relation:

$$I^{(k)} = \mathrm{I}(a,b) \tag{3.14}$$

$$E_n^{(k)} = E_n(a,b) \tag{3.15}$$

where $k = (a-1)\times p + b$.

Assuming the fiber has n modes, Eq. (3.14) can be rewritten in the form of

$$I^{(k)} = \sum_{i=1}^{n}\sum_{j=1}^{n} C_i C_j^* E_i^{(k)} E_j^{(k)} \quad , \tag{3.16}$$

$$\mathrm{k} = 1,2,3,\ldots,\mathrm{m}$$

The whole equation can be rearranged into matrix multiplication form so it can be easily solved:

$$\boldsymbol{I}_{m\times 1} = \boldsymbol{T}_{m\times n^2}\boldsymbol{Z}_{n^2\times 1} \tag{3.17}$$

$$\boldsymbol{T} = \begin{pmatrix} E_1^{(1)}E_1^{(1)} & E_1^{(1)}E_2^{(1)} & \ldots & E_1^{(1)}E_n^{(1)} & E_2^{(1)}E_1^{(1)} & \ldots & E_2^{(1)}E_n^{(1)} & \ldots & E_n^{(1)}E_1^{(1)} & \ldots & E_n^{(1)}E_n^{(1)} \\ E_1^{(2)}E_1^{(2)} & & & & & & & & & & \\ \vdots & & & \vdots & & & \vdots & & \vdots & & \vdots \\ E_1^{(m)}E_1^{(m)} & & \ldots & E_1^{(m)}E_n^{(m)} & & \ldots & E_2^{(m)}E_n^{(m)} & \ldots & E_n^{(m)}E_1^{(m)} & \ldots & E_n^{(m)}E_n^{(m)} \end{pmatrix}$$

$$\mathbf{Z}^T = (C_1C_1^* \quad C_1C_2^* \quad \ldots \quad C_1C_n^* \quad C_2C_1^* \quad \ldots \quad C_2C_n^* \quad \ldots \quad C_nC_1^* \quad \ldots \quad C_nC_n^*)$$

From Eq. (3.17), we can see that the mode decomposition problem is now presented as linear equations in matrix form. As we can get $\boldsymbol{T}$ from computer simulation of eigenmodes in fiber and $\boldsymbol{I}$ from measurement, we can solve for **Z** by using the Monroe-Penrose inverse of $\boldsymbol{T}^{-1}$.

$$\boldsymbol{T}^{-1}\boldsymbol{I} = \boldsymbol{Z} \tag{3.18}$$

Knowing $\boldsymbol{Z}$, we can solve the amplitude of each mode based on Eq. (3.19) and Eq. (3.20). Eq. (3.20) is a special case of Eq. (3.19).

doi:10.6342/NTU202204042

$$z^{(k)} = A_a A_b \cos(\varphi_a - \varphi_b), \quad \text{where } k = (a-1) \times p + b \tag{3.19}$$

$$A_k = \sqrt{z^{(k)}}, \quad \text{where } k = 1^2, 2^2, \ldots, n^2 \tag{3.20}$$

As we are only interested in power in each mode, we do not need to solve the phase.

3.2.3.2 Test with Simulation Data

To test for composition of modes in a particular fiber, we need to know the possible modes in the fiber and this can be done with simulation program if we know the geometry and refractive index of the fiber. Our algorithm is tested with a few-mode fiber with 3 modes, the modes are shown in Fig. 3-33(a)-(c). Fig. 3-33(d) shows the combination of three modes with different amplitude for each mode. Fig. 3-33(e)-(f) shows different amount of noise added to Fig. 3-29(d) to test for robustness of the algorithm. At higher signal-to-noise ratio, the algorithm works perfectly where the true and reconstructed amplitude is plotted in Fig. 3-34. For lower signal-to-noise ratio, mode with lower amplitude component is not detected (Fig. 3-34).

doi:10.6342/NTU202204042

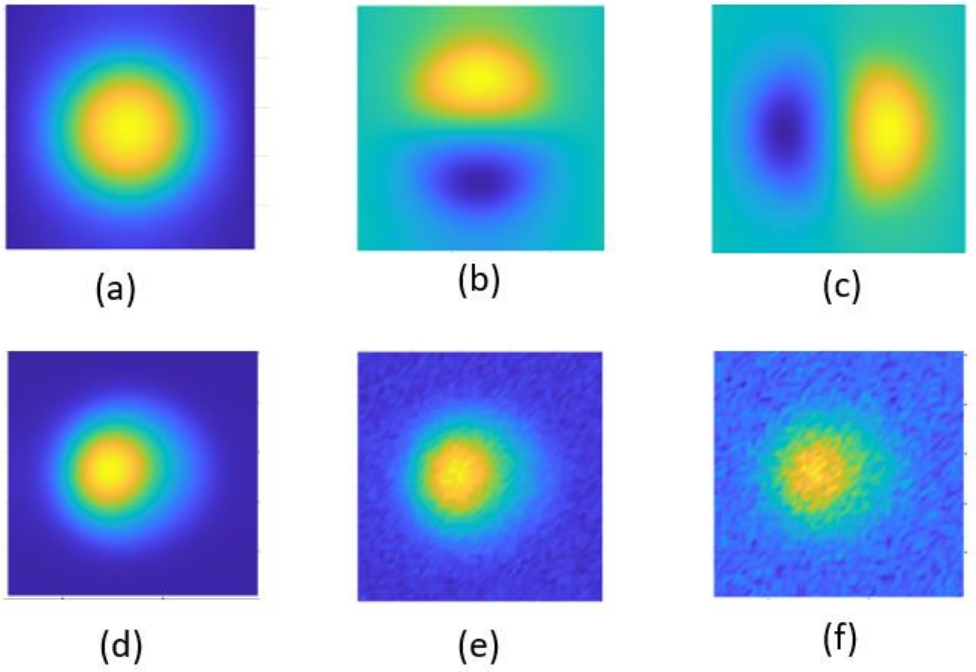

Fig. 3-33 (a)-(c) Electric of optical mode in few-mode fiber. (d) Combination of modes in (a)-(c). (e) 20dB SNR of (d). (f) 10dB SNR of (d).

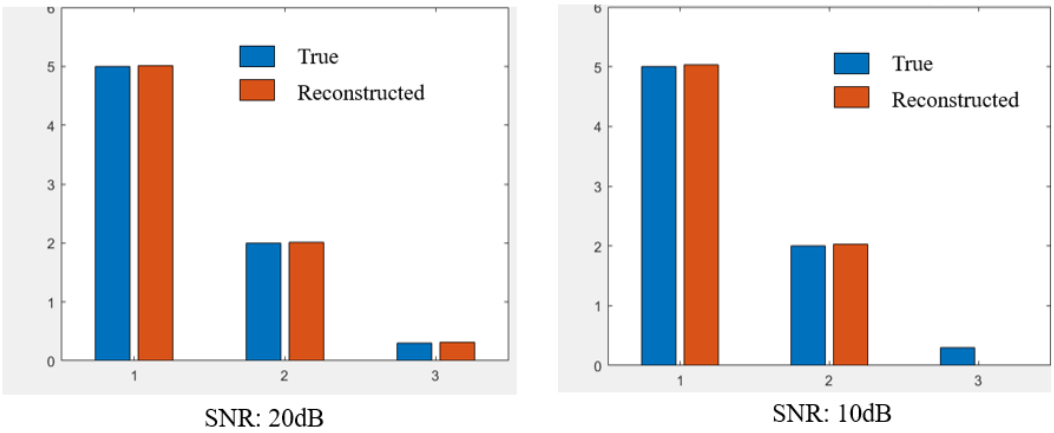

Fig. 3-34 Test result of mode decomposition with noise added

doi:10.6342/NTU202204042

3.2.4 Near Field Measurement of Fiber Modes

To ensure that the alignment between SMF and SCF during coupling process enables single mode coupling and also verify single mode transmission is possible in SMF, we will need to use mode decomposing algorithm to analyze the mode distribution in the output of SCF. The mode decomposing algorithm will only work on near field measurement of the fiber output mode. This is because the far field electromagnetic field is different from the near field after propagating in free space. To measure the near field electric field at the output edge of the fiber, a lens system is needed to focus the light from the output to the IR viewer (Fig. 3-35).

The output mode of two SCF, one with n-type silicon core, the other with intrinsic silicon core is measured. Both SCF have core diameter of 165 μm. A 1550 nm laser is used as source. SCF with large core is chosen so we do not need to use higher power magnification lens system. Higher power magnification will lower intensity and would be harder for the optical field to be detected by the low sensitivity phosphorus florescence-based IR viewer used here.

We found out that the n-type SCF has higher loss than intrinsic from the normalized intensity diagram from the IR viewer SCF (Fig. 3-37). This is due to the larger absorption coefficient of doped silicon compared to intrinsic silicon (Fig. 3-38). To do a near field measurement of SCF with core diameter of 15 μm, a higher sensitivity camera such as InGaAs camera is needed so a higher magnification system can be used to ensure there is enough resolution for mode decomposing to work.

doi:10.6342/NTU202204042

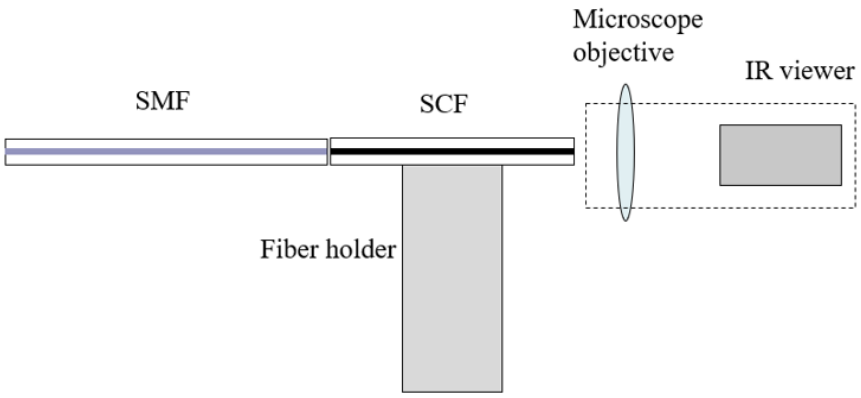

Fig. 3-35 Set-up of near field measurement system

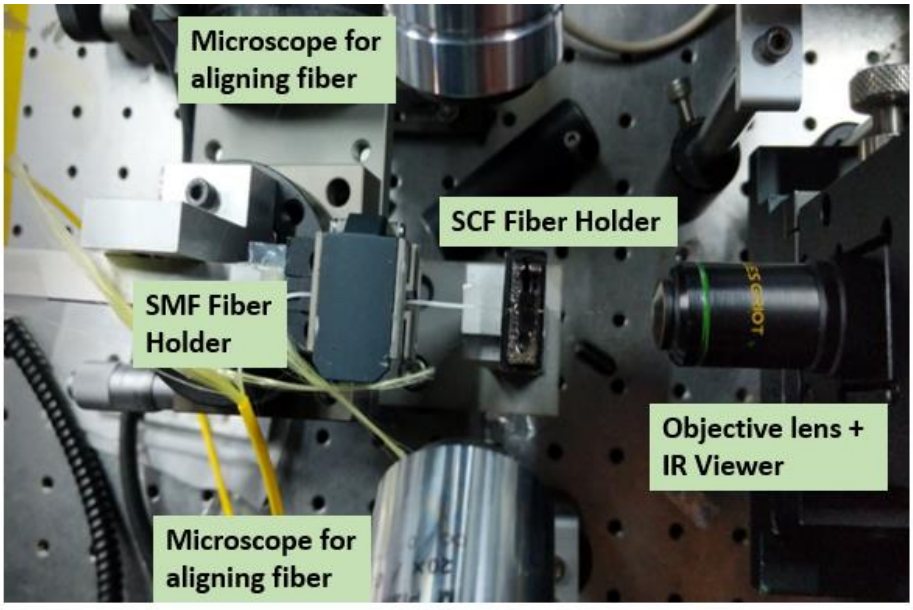

Fig. 3-36 Experiment set-up of near field measurement system

doi:10.6342/NTU202204042

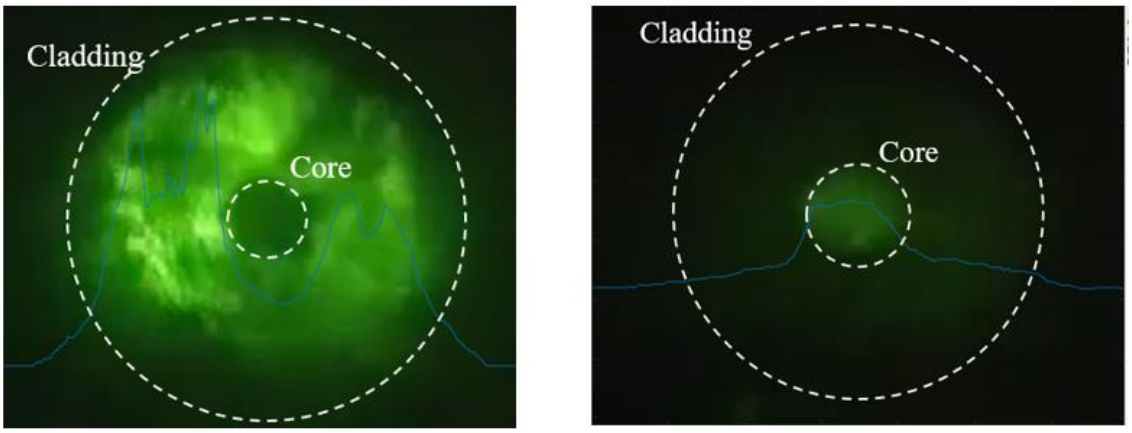

Fig. 3-37 Normalized intensity of (Left) N-type SCF (Right) Intrinsic SCF with core diameter of 165 μm

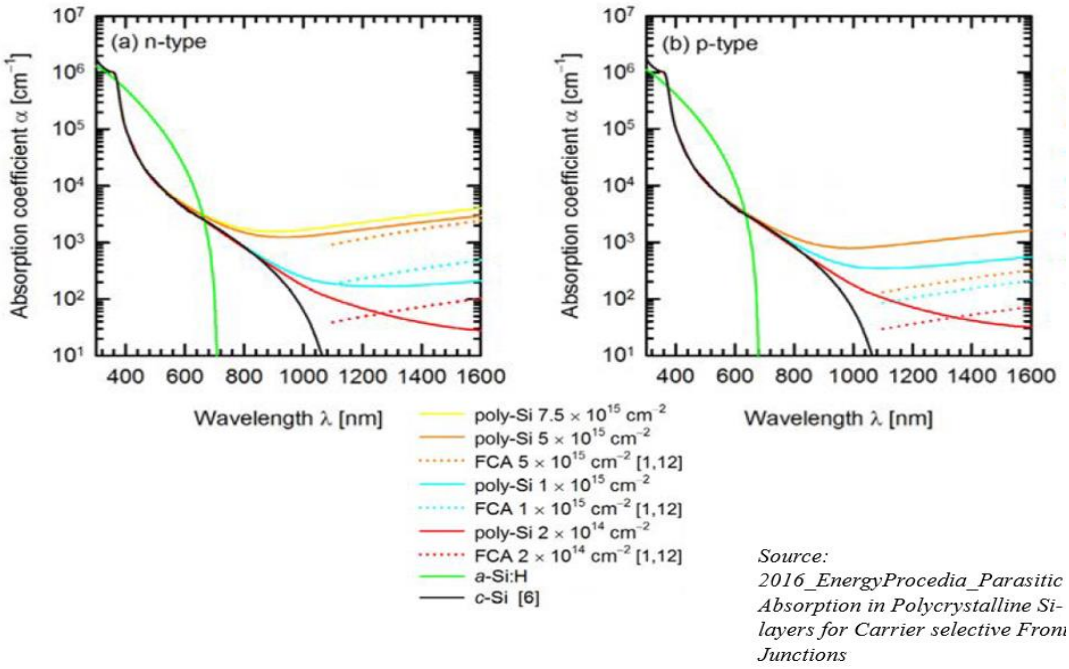

Fig. 3-38 Absorption coefficient of intrinsic vs doped silicon [75]

doi:10.6342/NTU202204042

3.3 Summary

In this chapter, annealing parameters that affect the cooling rate during annealing process is found through thermal simulation and experiment. Using a new annealing set-up which includes an aligning system and a temperature monitoring system, our simulation result is validated with our experiment result. The feasibility of single mode coupling and transmission in multimode SCF using mode matching and central launching method is also investigated. An algorithm is then written to identify the composition of optical modes travelling in a multimode fiber. A near field measurement of the output mode in n-type and intrinsic SCF is done and doped silicon core is found to have higher loss than intrinsic silicon core.

doi:10.6342/NTU202204042

Chapter 4 Design Guidelines for Coupled Waveguide Sensor

4.1 Introduction

In recent years, a lot of RI-index sensors based on wavelength interrogation using different types of sensing methods such as SPR, LRSPR and LMR on both chip and fiber waveguides had been proposed and experimentally tested [29-37]. However, there are no literature, to our knowledge that investigate the effect of various optical properties of the sensor on the performance of a sensor. Some examples of optical properties are effective mode index, gradient of effective mode index, loss in optical modes and they are functions of sensor's geometry and material. With the myriad of possible geometries and materials for designing sensors, it would be inefficient to simulate or fabricate all possible sensors to evaluate their performance for optimization purpose. Therefore, in this chapter, we developed a systemic analysis on how the optical characteristics of each structure in a sensor contributes to the performance of a sensor using Coupled Mode Theory (CMT). Optical simulation such as Eigenmode Expansion Method (EME) and Finite Difference Method (FDE) is used to further validate our findings. In the end, some guidelines for designing and optimizing a sensor is devised.

doi:10.6342/NTU202204042

4.2 Modes in Guided Waves Devices

In this section, we are dealing primarily with guided mode optics. Therefore, we need to understand optical modes propagation in guided mode structures. Optical modes are eigenmode solutions to the Maxwell Equation in an optical structure. The overall electromagnetic field in a guided mode structure $\{\boldsymbol{E}, \boldsymbol{H}\}$ can be written as a linear combination of all the eigenmodes.

$$\boldsymbol{E} = \sum_n C_n(z)\boldsymbol{E_n} \tag{4.1a}$$

$$\boldsymbol{H} = \sum_n C_n(z)\boldsymbol{H_n} \tag{4.1b}$$

where $\boldsymbol{E_n}, \boldsymbol{H_n}$ are eigenmodes in the guided mode structure.

The eigenmodes $\boldsymbol{E_n}, \boldsymbol{H_n}$ can be further separate into a traverse and axial component

$$\boldsymbol{E_n} = \boldsymbol{E_{tn}}(x,y)E_{zn}(x,y)e^{(i\omega t - i\beta z)} \tag{4.2a}$$

$$\boldsymbol{H_n} = \boldsymbol{H_{tn}}(x,y)H_{zn}(x,y)e^{(i\omega t - i\beta z)} \tag{4.2b}$$

where $\boldsymbol{E_{tn}}$ and $\boldsymbol{H_{tn}}$ are transverse field distribution, E_{zn} and H_{zn} are axial field distribution, ω is the frequency and β is the propagation constant for each mode. β can be further expressed as:

$$\beta = \frac{2\pi}{\lambda} N_{eff} \tag{4.3}$$

where N_{eff} is the effective refractive index of the eigenmodes and λ is the wavelength. Both β and N_{eff} can be complex if the eigenmode have loss or gain component.

doi:10.6342/NTU202204042

4.3 Coupled Waveguide Sensor

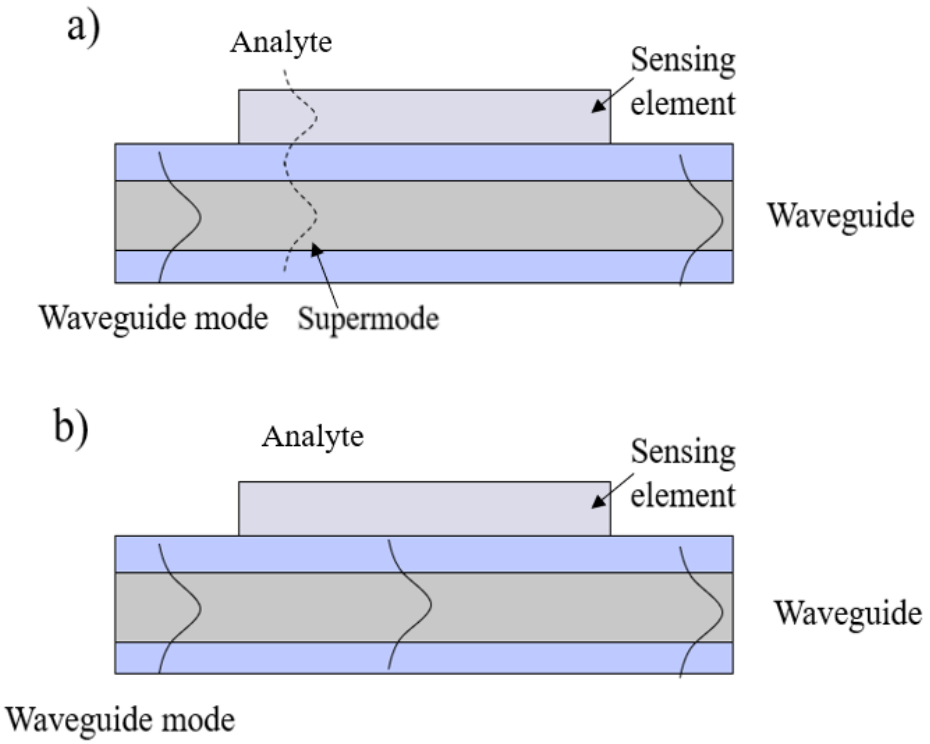

Fig. 4-1 (a) Phase matching condition. (b) No phase matching.

In a coupled waveguide sensor, there are two main components, a waveguide and a sensing element. Both the waveguide and sensing element are guided wave devices and optical power can couple between them at phase matching condition. When light wave travels down the waveguide in certain optical mode, it will encounter the sensing element in the sensor. If the real part of effective refractive index, $N_{eff,r}$ of the waveguide optical mode coincides with the $N_{eff,r}$ of a particular optical mode of the sensing element, phase matching between these two optical modes occurs. Energy will be coupled from the waveguide into the sensing element, forming supermodes (Fig. 4-1(a)). After exiting the sensor region, the supermodes will be coupled back to the waveguide mode causing a change in the transmission power of the waveguide. If no

doi:10.6342/NTU202204042

phase matching between optical modes occur, the waveguide optical mode will travel through the sensor region only slightly perturbed (Fig. 4-1(b)). Transmission of the optical mode will be close to 1.

Fig. 4-2 is a graph depicting the real part of effective refractive index versus wavelength of optical mode in sensing element (black line) and waveguide's optical mode (green line). At the intersection between the two lines, $N_{eff,r}$ of the two optical modes are the same, therefore phase matching between these two optical modes occurs. The optical power at the wavelength where phase matching occurs will see a dip in transmission. At wavelength where no phase matching occurs, the transmission will be close to 1. This phenomenon forms the unique optical spectrum of the sensor (Fig. 4-2 inset). At wavelength close to the phase matching wavelength, power can still couple to the sensing element although at a slower rate compared to phase matching wavelength, which is why the spectrum in the sensor's optical spectrum is not infinitely narrow. The relationship between coupling rate (rate of power flow between waveguide and sensing element) and wavelength will affect the width of the sensor's optical spectrum and can be shown using complex coupled mode theory.

For a wavelength interrogation based refractive index sensor, the information about refractive index (RI) of the analyte is convey through the shift in local minimum of optical spectrum. The sensing element, which is in direct contact with the analyte, experienced a change in $N_{eff,r}$ of optical mode according to the RI of the analyte. In Fig. 4-3, the black line, $N_{eff,r}$ of the sensing element's optical mode shift upwards when the analyte's RI changes from n_s to $(n_s + \delta n_s)$. The intersection point between black and green line ($N_{eff,r}$ of the waveguide's optical mode) changes which

doi:10.6342/NTU202204042

corresponds to the shift in wavelength when phase matching condition occurs. This in turn shows up as a shift in local minimum in the sensor's optical spectrum.

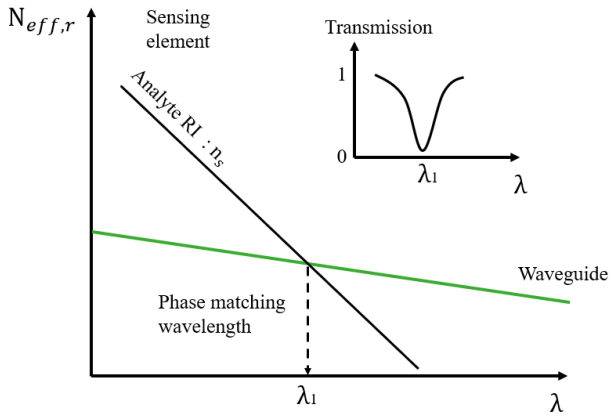

Fig. 4-2 (Black line) Real part of effective index of optical mode of sensing element (Green line) Real part of effective index of waveguide mode (Inset) Optical spectrum of sensor

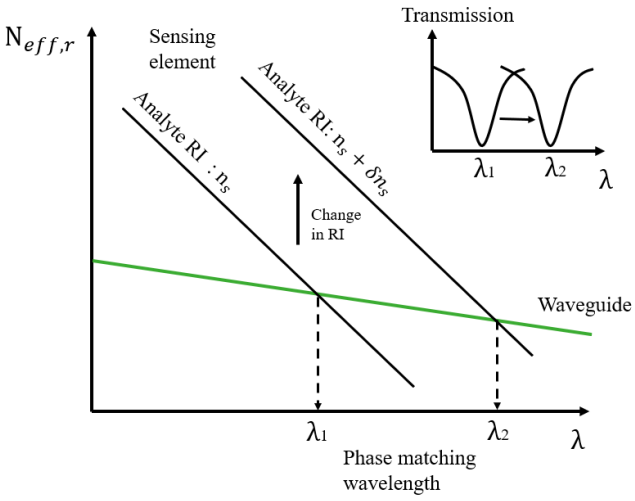

Fig. 4-3 (Black line) Real part of effective index of optical mode of sensing element (Green line) Real part of effective index of waveguide mode (Inset) Optical spectrum of sensor.

doi:10.6342/NTU202204042

4.4 Complex Coupled Mode Theory for Coupled Waveguide Sensor

In the last section, a rough overview of how a coupled waveguide sensor function is discussed. In this section, complex Coupled Mode Theory (CMT) [76] is used for a detail analysis on how power transfer between waveguide and sensing element at phase matching and near phase matching condition so that we can optimize the performance of the sensor. Coupled waveguide sensor is quite similar to a directional coupler in the way power is coupled between two guided wave devices. The difference between a directional coupler and a coupled waveguide sensor is that both waveguide in a directional coupler are lossless waveguides. One the other hand, one of the waveguides, the sensing element in a coupled waveguide sensor is a lossy waveguide. Example of sensing element in coupled waveguide sensors are plasmonic or loss mode resonance waveguides which are both lossy waveguides. Therefore, complex components of the optical modes in the sensing element must be accounted for when using CMT on coupled waveguide sensors.

Although CMT is generally valid for weakly guided devices at weakly coupling conditions, it has shown to work well on predicting the general behavior of waveguide [77-78] and plasmonic waveguide [79-80] directional coupler. With the help of computational techniques such as Finite Difference Element Method (FDE) and Eigenmode Expansion Method (EME) to solved Maxwell Equation numerically, a more accurate result can be obtained and can be used during the final stage of designing a sensor. Nevertheless, CMT serve as a tool to understand the physics behind such device and also provide a guideline for designing them. In our analysis of coupled waveguide

doi:10.6342/NTU202204042

sensors, CMT is used to understand the sensor's behavior and computational/optical simulation methods will be used to validate our findings.

4.4.1 Derivation of Complex Coupled Mode Theory

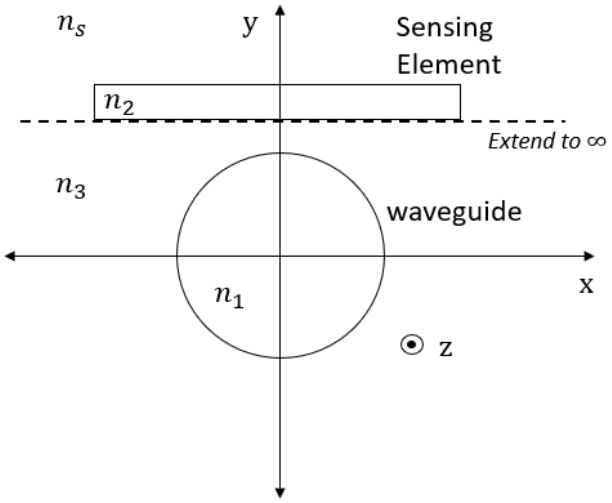

Fig. 4-4 Axial cross-section of an asymmetrical coupled waveguide sensor structure consisting of a round waveguide and a rectangular waveguide as sensing element. Optical mode travel in the z direction.

Fig. 4-4 shows an axial cross-section of an asymmetrical coupled waveguide sensor, with a round waveguide and a rectangular waveguide which act as a sensing element. When the sensing element is placed close enough so that the evanescent wave field of the round waveguide overlaps it, modes in in the sensing element can be excited forming supermodes. For the simplicity of the derivation, we assumed the round waveguide to be single mode, where its field is made up of only one eigenmode $\{\boldsymbol{E_1}, \boldsymbol{H_1}\}$. As for the rectangular waveguide, its electromagnetic field can be written as a summation of eigenmodes assuming it to be multimode in nature

doi:10.6342/NTU202204042

$$\boldsymbol{E_2} = \sum_n B_n(z)\boldsymbol{E_{2n}} \tag{4.4a}$$

$$\boldsymbol{H_2} = \sum_n B_n(z)\boldsymbol{H_{2n}} \tag{4.4b}$$

The overall electromagnetic field of the supermodes can be expressed as a combination of individual eigenmode field in each waveguide. Where A(z) and $B_n(z)$ are amplitude coefficients of each eigenmodes.

$$\boldsymbol{E} = A(z)\boldsymbol{E_1} + \sum_n B_n(z)\boldsymbol{E_{2n}} \tag{4.5a}$$

$$\boldsymbol{H} = A(z)\boldsymbol{H_1} + \sum_n B_n(z)\boldsymbol{H_{2n}} \tag{4.5b}$$

As we are only interested in the wavelength region where one optical mode in the sensing element is at phase matching condition with the optical mode in the round waveguide, we can simplify the overall field to only two eigenmodes as the propagation constant difference between the other eigenmodes in the sensing element and round waveguide is too large for them to contribute in the supermode. The overall electromagnetic field of the supermodes can be simplified to a combination of two individual eigenmode field, $\boldsymbol{E_1}$ and $\boldsymbol{E_2}$. Where A(z) and B(z) are amplitude coefficients of each eigenmodes.

$$\boldsymbol{E} = A(z)\boldsymbol{E_1} + B(z)\boldsymbol{E_2} \tag{4.6a}$$

$$\boldsymbol{H} = A(z)\boldsymbol{H_1} + B(z)\boldsymbol{H_2} \tag{4.6b}$$

The electromagnetic field equation must satisfy Maxwell's Equation

$$\nabla \times \boldsymbol{E} = -i\omega\mu\boldsymbol{H} \tag{4.7a}$$

$$\nabla \times \boldsymbol{H} = -i\omega\varepsilon\boldsymbol{E} \tag{4.7b}$$

Substituting Eq. (4.6a), Eq. (4.6b) into Eq. (4.7a), Eq. (4.7b), we can get write the amplitude coefficient of each eigenmodes as below. Note that this form of coupled

doi:10.6342/NTU202204042

mode equation is a simplified version where correction to propagation constant of each mode and butt-coupling coefficient between waveguide are neglected. Nevertheless, it is the version used in almost all published works and sufficient for us to understand the physics behind couplers. We will also be using the complex version of CMT which involves using complex propagation constant instead of real propagation constant [76].

$$\frac{dA(z)}{dz} = -i\beta_1 A(z) - i\kappa_{12} B(z) \tag{4.8a}$$

$$\frac{dB(z)}{dz} = -i\beta_2 B(z) - i\kappa_{21} A(z) \tag{4.8b}$$

where β_1 is the propagation constant of eigenmode in round waveguide, β_2 is the propagation constant of the eigenmode in the sensing element, $\kappa_{12}$and κ_{21} are the coupling coefficients between each mode and can be expressed as [76]:

$$\kappa_{mn} = \frac{\omega\varepsilon_0 \iint (n^2 - n_n^2) E_{tn}^* E_{tm} dA}{\iint (E_{tm}^* \times H_{tn} + E_{tm} \times H_{tn}^*) dA} \tag{4.9}$$

where E_{tm} and E_{tn} are transverse electric fields of m and n mode respectively, E_{tm}^* and E_{tn}^* are complex conjugate of transverse electric fields of m and n mode, n is the RI of the whole sensor and n_n is the individual RI of n waveguide. The difference of square between them, $(n^2 - n_n^2)$ is the square of RI in the perturbed region (Fig. 4-5(a)). From, Eq. (4.9), we can see that the coupling coefficient is directly proportional to the summation of the product of E_{tm} and E_{tn} in the perturbed region (Fig. 4-5(b)). If n and m waveguides are closer to each other, the E_{tn} overlapping the perturbed region will be larger and hence the coupling coefficient will be larger.

doi:10.6342/NTU202204042

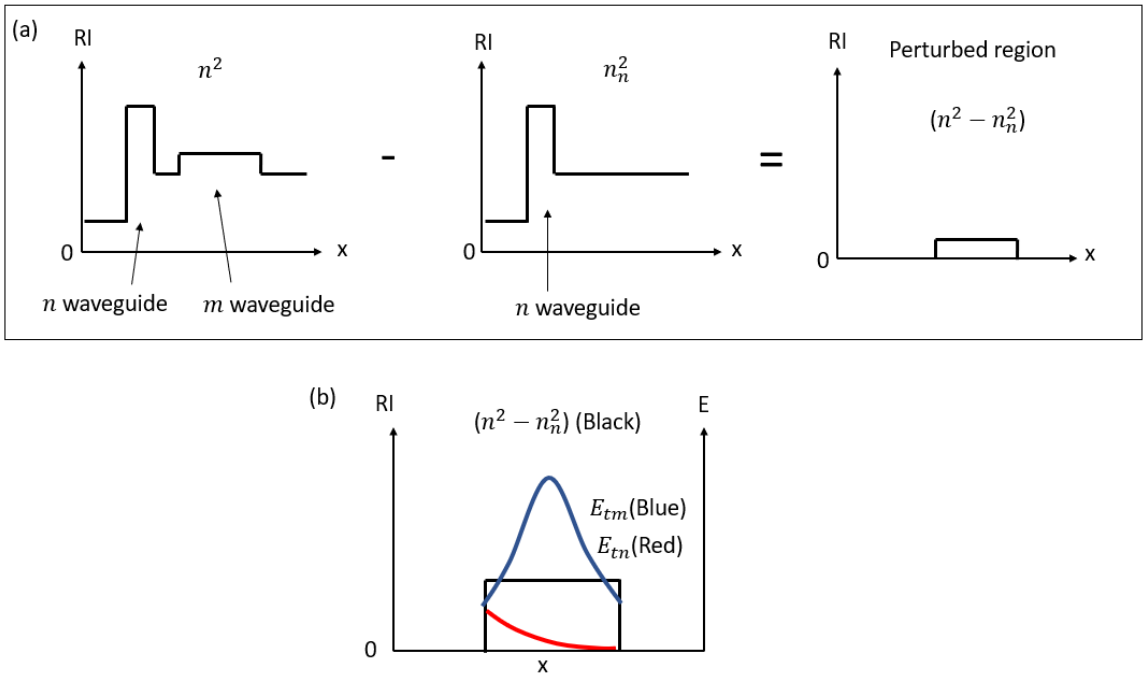

Fig. 4-5 (a) Perturbed Refractive Index (b) E_{tm} and E_{tn} in the perturbed region

To solve Eq. (4.8a) and Eq. (4.8b), we can write the amplitude coefficient $A(z)$ and $B(z)$ as a combination of constant and oscillation term with phase constant β:

$$A(z) = ae^{-i\beta z} \tag{4.10a}$$

$$B(z) = be^{-i\beta z} \tag{4.10b}$$

Substituting Eq. (4.10a), Eq. (4.10b) into Eq. (4.8a), Eq. (4.8b), we get

$$a(\beta - \beta_1) = \kappa_{12} b \tag{4.11a}$$

$$b(\beta - \beta_2) = \kappa_{21} a \tag{4.11b}$$

Solving equations (4.11a) and (4.11b) by combining both equations, we get the quadratic equation

$$\beta^2 - \beta(\beta_1 + \beta_2) + \beta_1\beta_2 - \kappa_{12}\kappa_{21} = 0 \tag{4.12}$$

doi:10.6342/NTU202204042

There are two solutions to β are β_e and β_o, indicating the formation of odd and even modes

$$\beta_{e,o} = \beta_{av} \pm \sqrt{\left(\frac{\Delta\beta}{2}\right)^2 + \kappa^2} \tag{4.13}$$

where $\beta_{av} = \frac{(\beta_1+\beta_2)}{2}$, $\Delta\beta = (\beta_1 - \beta_2)$ and $\kappa = \sqrt{\kappa_{12}\kappa_{21}}$.

The general solution for the coupled mode equations can thus be written as:

$$\mathrm{A(z)} = \left(a_o e^{\delta \mathrm{z}} + a_e e^{-\delta \mathrm{z}}\right) e^{-i\beta_{av} z} \tag{4.14a}$$

$$\mathrm{B(z)} = \left(\frac{\beta_o - \beta_1}{\kappa_{12}} a_o e^{\delta \mathrm{z}} + \frac{\beta_e - \beta_1}{\kappa_{12}} a_e e^{-\delta \mathrm{z}}\right) e^{-i\beta_{av} z} \tag{4.14b}$$

where $\delta = \sqrt{\left(\frac{\Delta\beta}{2}\right)^2 + \kappa^2}$, a_o and a_e are the coefficients for odd and even supermodes respectively.

The equations (4.14a) and (4.14b) is really no different from normal coupled mode theory equation for lossless coupler. However, it is only when substituting the complex propagation constant of lossy sensing element into the equations where we can see the difference between power propagation between a sensor and a coupler.

doi:10.6342/NTU202204042

4.4.2 Power in Coupled Waveguide Sensor

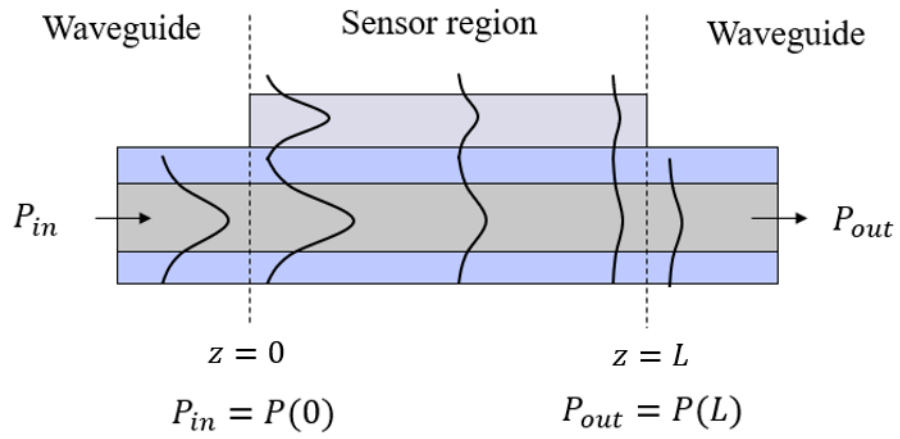

Fig. 4-6 Power of optical mode in waveguide sensor

To obtain the optical spectrum of a coupled waveguide sensor, the power of optical mode in the waveguide, P_{out} over a frequency band is measured. P_{out} is equal to the power in the waveguide (in our case the round waveguide) in a sensor region at the edge of the sensor region, $P(L)$ (Fig. 4-6). Therefore, we need to calculate the power in the waveguide along the sensor axis in the sensor region, $P(L)$. $P(L)$ can be expressed as:

$$P(L) = \frac{|A(L)|^2}{|A(0)|^2} \tag{4.15}$$

Using boundary conditions:

$$a_o + a_e = A(0) = 1 \tag{4.16a}$$

$$b_o + b_e = B(0) = 0 \tag{4.16b}$$

And substituting them into Eq. (4.14a) and (4.14b), we can than expressed $a_o$anda_e in terms of δ and Δβ.

doi:10.6342/NTU202204042

$$a_o = \frac{2\delta + \Delta\beta}{4\delta} \tag{4.17a}$$

$$a_e = \frac{2\delta - \Delta\beta}{4\delta} \tag{4.17b}$$

Now we have all the required information to calculate the power in the waveguide of the sensor region.

Let's consider the sensor structure in Fig. 4-4, the round waveguide is a lossless waveguide which has a single eigenmode with propagation constant β_1. B_1 is purely real because the eigenmode is lossless. The sensing element has eigenmode with propagation constant β_2 , a complex number, the negative imaginary part signifies loss as oppose to positive signifying gain.

$$\beta_1 = \beta_{1,r} \tag{4.18a}$$

$$\beta_2 = \beta_{2,r} - i\beta_{2,i} \tag{4.18b}$$

where $\beta_{1,r}$, $\beta_{2,r}$ and $\beta_{2,i}$ are all positive number.

doi:10.6342/NTU202204042

4.4.3 Phase Matching Condition

At phase matching condition,

$$\beta_{1,r} = \beta_{2,r} \tag{4.19}$$

Therefore,

$$\Delta\beta = (\beta_1 - \beta_2) = i\beta_{2,i} \tag{4.20a}$$

$$\beta_{av} = \frac{(\beta_1 + \beta_2)}{2} = \beta_{2,r} - \frac{i\beta_{2,i}}{2} \tag{4.20b}$$

$$\delta = \sqrt{\left(\frac{\Delta\beta}{2}\right)^2 + \kappa^2} = \sqrt{\left(\frac{i\beta_{2,i}}{2}\right)^2 + \kappa^2} = \sqrt{-\left(\frac{\beta_{2,i}}{2}\right)^2 + \kappa^2} \tag{4.20c}$$

From Eq. (4.20.c), we can see that δ will be either real or imaginary depending on the magnitude of $\beta_{2,i}$ in comparison to κ. This actually influenced how power flow characteristics in the sensor. We characterized them as over coupled, critically coupled and under coupled conditions in analogy to under damped, critically damped and over damped conditions in a spring mass system. This is because the power-distance curve of the waveguide in the sensor element under these conditions have similar profiles to the displacement-time curve of the spring mass system.

doi:10.6342/NTU202204042

The conditions are categorized as follows:

Over coupled: $|\beta_{2,i}| < 2\kappa \quad => \quad -\left(\frac{\beta_{2,i}}{2}\right)^2 + \kappa^2 > 0$ $\quad \delta =$ Purely Real

Critical coupled: $|\beta_{2,i}| = 2\kappa \quad => \quad -\left(\frac{\beta_{2,i}}{2}\right)^2 + \kappa^2 = 0$ $\quad \delta = 0$

Under coupled $|\beta_{2,i}| > 2\kappa \quad => \quad -\left(\frac{\beta_{2,i}}{2}\right)^2 + \kappa^2 < 0$ $\quad \delta =$ Purely Imaginary

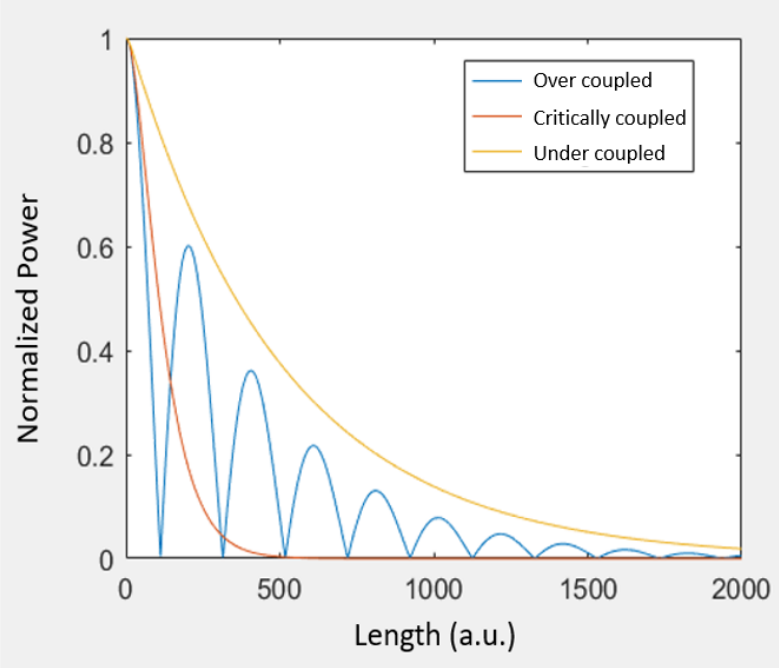

Fig. 4-7 Power along the waveguide in the sensor region at phase matching condition for three types of coupled condition.

doi:10.6342/NTU202204042

For over coupled condition:

$\delta = h$, where h is a real positive number

$$\mathrm{A(z)} = \left[a_o e^{ihz} + a_e e^{-ihz}\right] e^{-i\beta_{2,r}z} e^{-\frac{\beta_{2,i}}{2}z} \tag{4.21a}$$

$$\mathrm{P}(z) = \frac{|A(z)|^2}{|A(0)|^2} = \left[1 - \frac{2\kappa^2 - {\beta_{2,i}}^2}{2h^2}\sin(hz)\right] e^{-\beta_{2,i}z} \tag{4.21b}$$

(substitute Eq. (4.17a) and (4.17b) into Eq.(4.21a) to get Eq. (4.21b))

The first term of Eq. (4.21b) is an oscillating function while the second term is a purely decaying envelope function. The power at such condition is plot in the graph in Fig. 4-7 (Blue line). This is quite similar to a lossless coupler where optical power oscillates between the two waveguides. However, in a coupled waveguide sensor, the power is decaying as well as oscillating (Fig. 4-8).

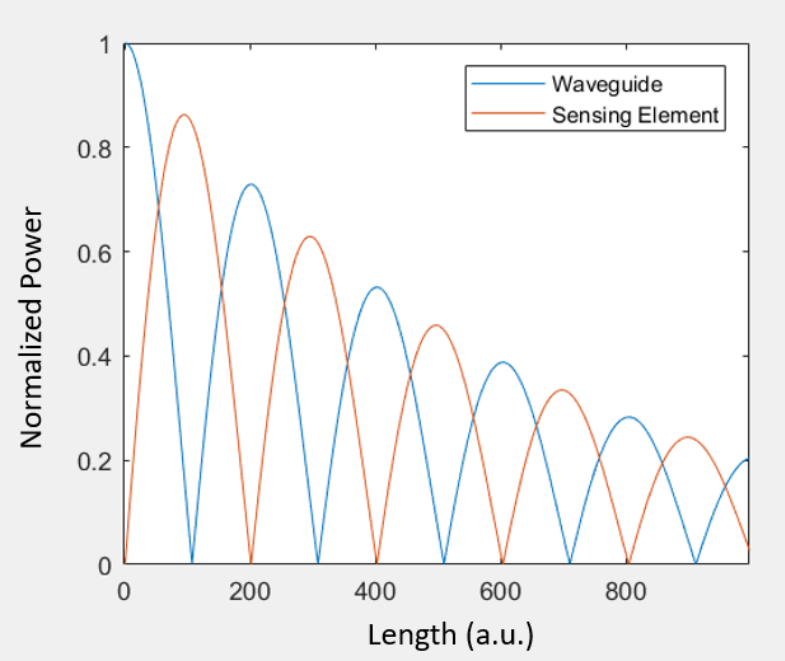

Fig. 4-8 Power along the waveguide (Blue line) and sensing element (Orange line) in the sensor region at phase matching condition for over coupled condition

doi:10.6342/NTU202204042

For critical coupled condition:

$\delta = 0$,

$$\mathrm{A(z)} = [a_{\mathrm{o}} + a_{\mathrm{e}}]e^{-i\beta_{2,r}z}e^{-\frac{\beta_{2,i}}{2}z} \tag{4.22a}$$

$$\mathrm{P}(z) = \frac{|A(z)|^2}{|A(0)|^2} = e^{-\beta_{2,i}z} \tag{4.22b}$$

(substitute Eq. (4.16a) into Eq.(4.22a) to get Eq. (4.22b))

Eq. (4.22b) is a purely decaying function as plotted in Fig. 4-7 (Orange line). At this condition, power no longer oscillates between the two waveguides. After the power from waveguide is coupled into the sensing element, power in both structure decays together (Fig. 4-9).

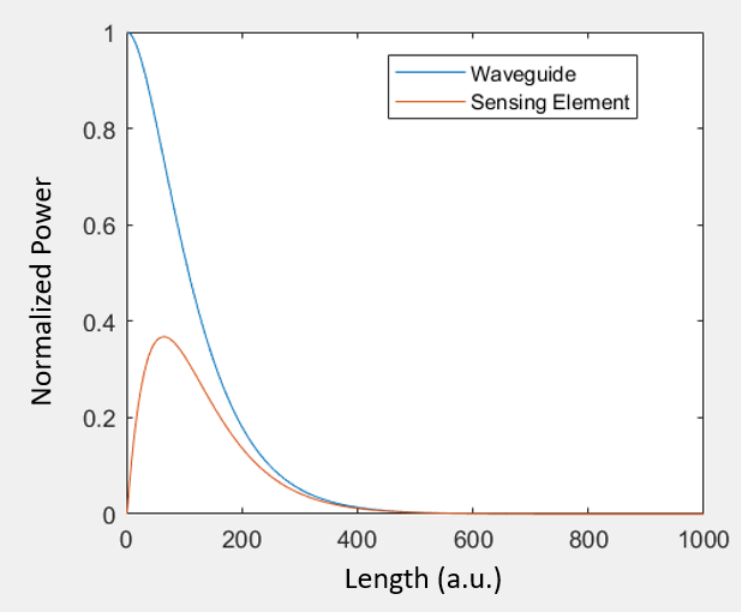

Fig. 4-9 Power along the waveguide (Blue line) and sensing element (Orange line) in the sensor region at phase matching condition for critical coupled condition

doi:10.6342/NTU202204042

For under coupled condition:

$\delta = ih$, where h is a positive real number

$$\mathrm{A(z)} = [a_o e^{hz} + a_e e^{-hz}] e^{-i\beta_{2,r} z} e^{-\frac{\beta_{2,i}}{2} z} \tag{4.23a}$$

$$\mathrm{P(L)} = \frac{|A(z)|^2}{|A(0)|^2} = \left[\cosh(hz) + \frac{\beta_{2,i}}{2h}\sinh(hz)\right]^2 e^{-\beta_{2,i} z} \tag{4.23b}$$

(substitute Eq. (4.17a) and (4.17b) into Eq.(4.23a) to get Eq. (4.23b))

Eq. (4.23b) similar to Eq. (4.19b) is a purely decaying function although at a slower rate as plotted in Fig. 4-7 (Yellow line). Similar to critical coupled condition, after the power from waveguide is coupled into the sensing element, power in both structure decays together (Fig. 4-10). However, when the loss increases the decay rate decreases and the rate approaches 0 as the loss is way larger than the coupling coefficient (Fig. 4-11). It's interesting as intuitively, we would think that a higher loss in sensing element would increase the decay rate of the power and it is actually the opposite instead.

doi:10.6342/NTU202204042

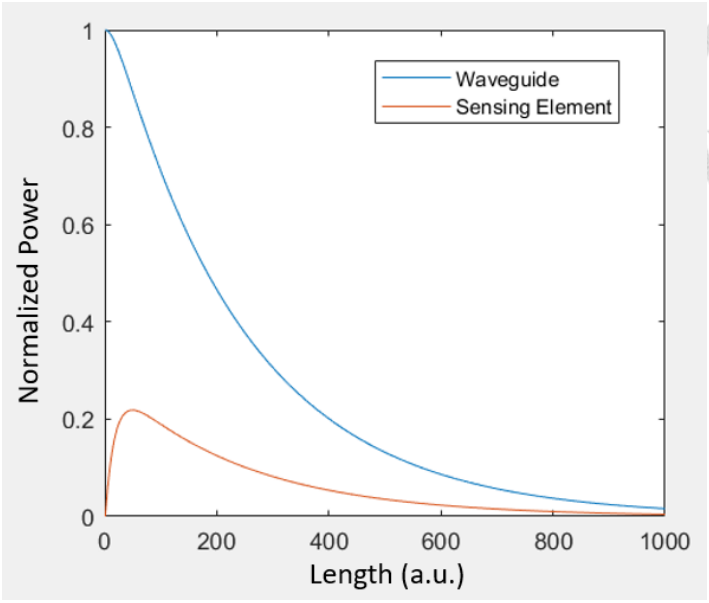

Fig. 4-10 Power along the waveguide (Blue line) and sensing element (Orange line) in the sensor region at phase matching condition for under coupled condition

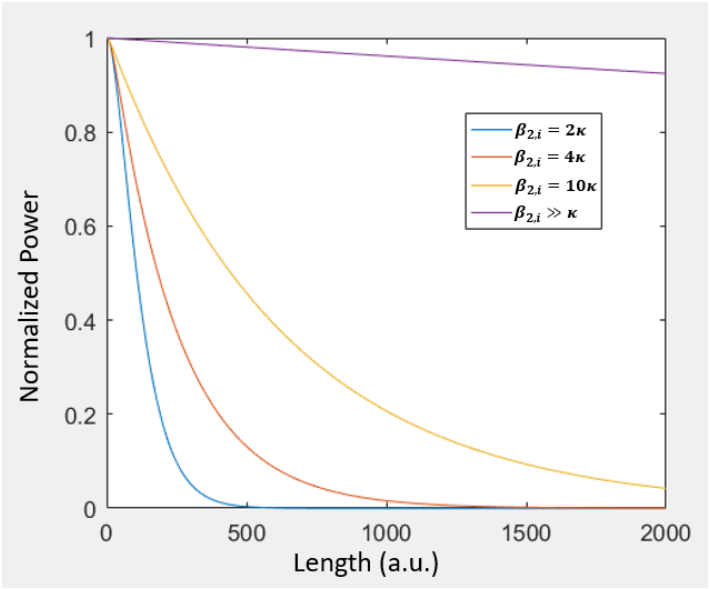

Fig. 4-11 Power along the waveguide in the sensor region at phase matching condition for different loss in terms of coupling coefficient value

doi:10.6342/NTU202204042

4.4.4 Non-phase Matching Condition

At non-phase matching condition, the difference between propagation constant of optical modes in the sensing element and waveguide in a sensor can be expressed as:

$$\Delta\beta = (\beta_1 - \beta_2) = \Delta\beta_r + i\beta_{2,i} \quad (4.24)$$

where $\Delta\beta_r$ is the real part of the propagation constant difference.

For all coupled conditions, we can see that the power in waveguide of the sensor region decay at a slower rate as the $|\Delta\beta|$ increases (Fig. 4-12). Notice the lower the loss of the optical mode of the sensing element, the power decay rate for same $\Delta\beta_r$ decreases.

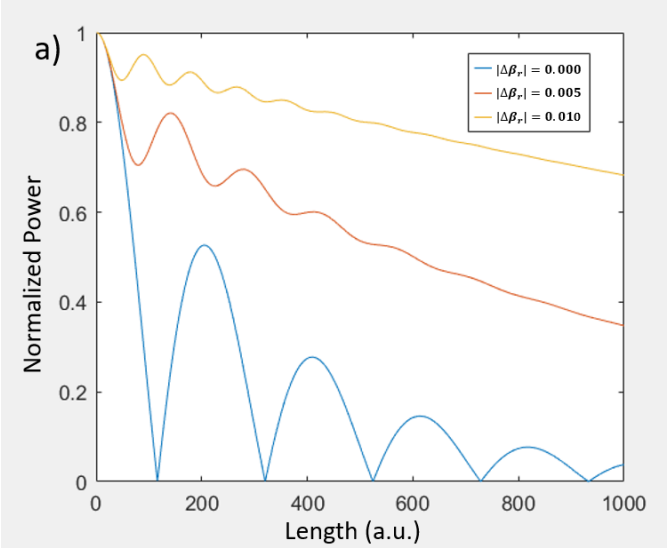

Fig. 4-12 (a) Power along the waveguide in the sensor region at different propagation constant difference for over coupled condition

doi:10.6342/NTU202204042

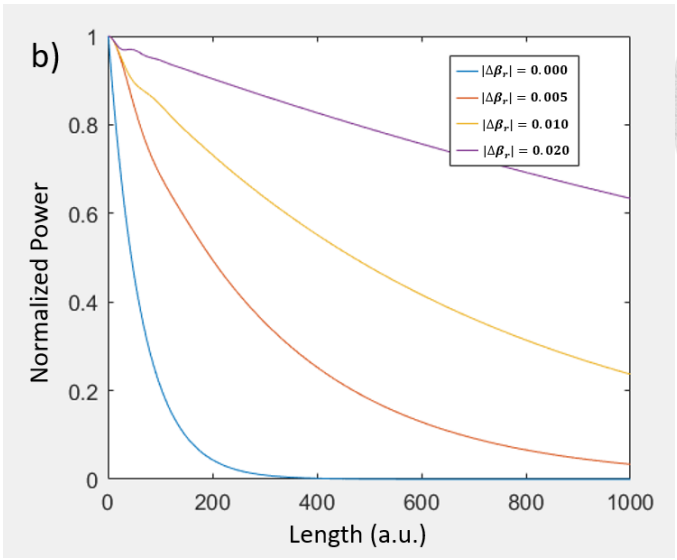

Fig. 4-12 (b) Power along the waveguide in the sensor region at different propagation constant difference for critical coupled condition

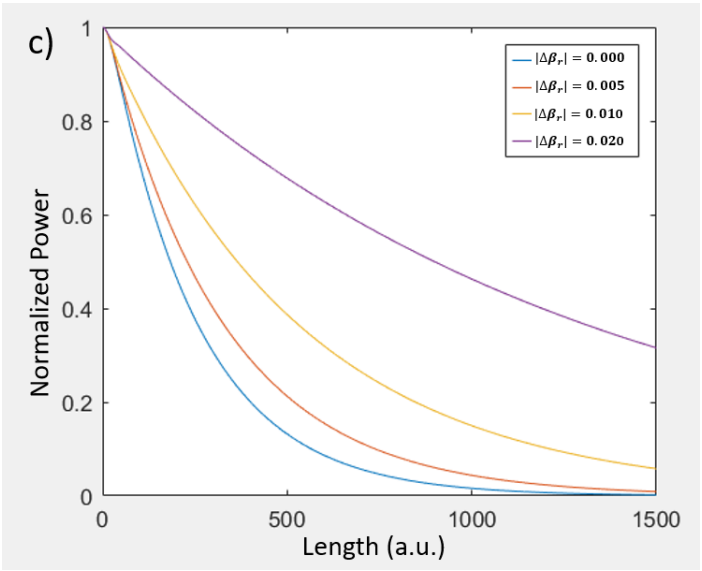

Fig. 4-12 (c) Power along the waveguide in the sensor region at different propagation constant difference for under coupled condition

doi:10.6342/NTU202204042

4.4.5 Sensor Optical Spectrum

At wavelength above and below phase matching wavelength, $|\Delta\beta_r| > 0$, therefore the optical modes passing through the sensor region has lower loss in power compared to optical mode at phase matching wavelength, forming a local minimum at the phase matching frequency (Fig. 4-13). $\Delta\beta_r$ at different wavelength can be expressed as the difference between effective refractive index of the modes in the waveguide and sensing element in the sensor:

$$\Delta\beta_r(\lambda_n) = \frac{2\pi}{\lambda_n}\Delta \mathrm{N}_{eff,\,r}\,(\lambda_n) \tag{4.25}$$

From Fig. 4-13, we can see that the geometry of the sensor such as the length of the sensor can influence the shape of the spectrum. For under coupled and critically coupled conditions, we can see that if the length of sensor is longer than the length when the power at phase matched wavelength has reach null, the width to depth ratio of spectrum increases (Fig. 4-13b). This will lower the FOM of a sensor. As for over coupled condition, choosing the length for the sensor would be more critical because of the interferometer-like spectrum. Length between two null points at phase match wavelength would yield spectrum that is less sharp (Fig.4-15(b)-(c)).

As for the distance between the sensing element and waveguide, we can use this parameter to control the coupling coefficient κ of the sensor. As seen from Eq. (4.9), κ is proportional to the electric field strength overlapping the perturbed region (Fig. 4-5). With the waveguide and sensing element in a sensor region closer to each other, the electric field of the evanescent field overlapping each element will be stronger.

We can thus change the distance between the sensor element and waveguide so that the sensor is at different coupled conditions. This enables us to control the shape of the sensor's optical spectrum and will be further discussed in section 4.6. However, the

doi:10.6342/NTU202204042

coupling coefficient will reach a maximum value when the distance between the sensing element and waveguide is 0. If the loss in the sensing element is too high and is larger than two times the maximum coupling coefficient, the sensor will always be at under coupled condition.

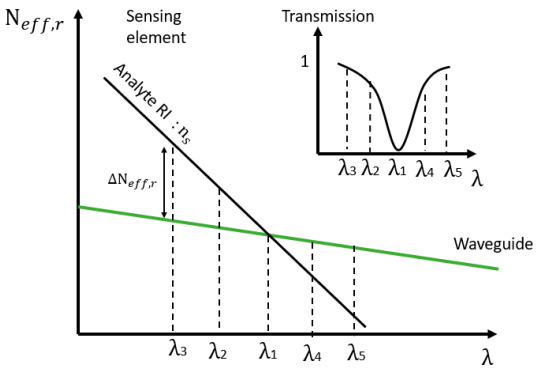

Fig. 4-13 Wavelength other than phase matching wavelength, λ_1 has $|\Delta\beta_r(\lambda_n)| > 0$ [see Eq. (4.25)], therefore transmission power is higher at other wavelengths, forming a spectrum with local minimum at λ_1(Inset)

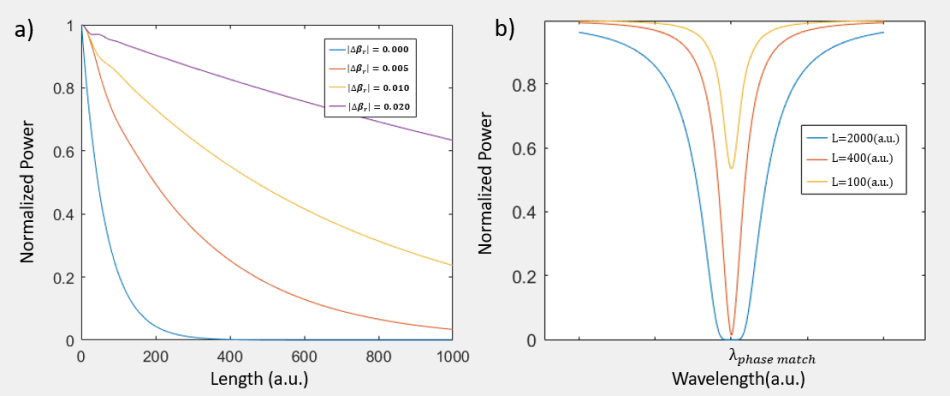

Fig. 4-14 (a) Power along the waveguide in the sensor region at different propagation constant difference for critical coupled condition. (b) The optical spectrum for different sensor length based on exact condition in (a).

doi:10.6342/NTU202204042

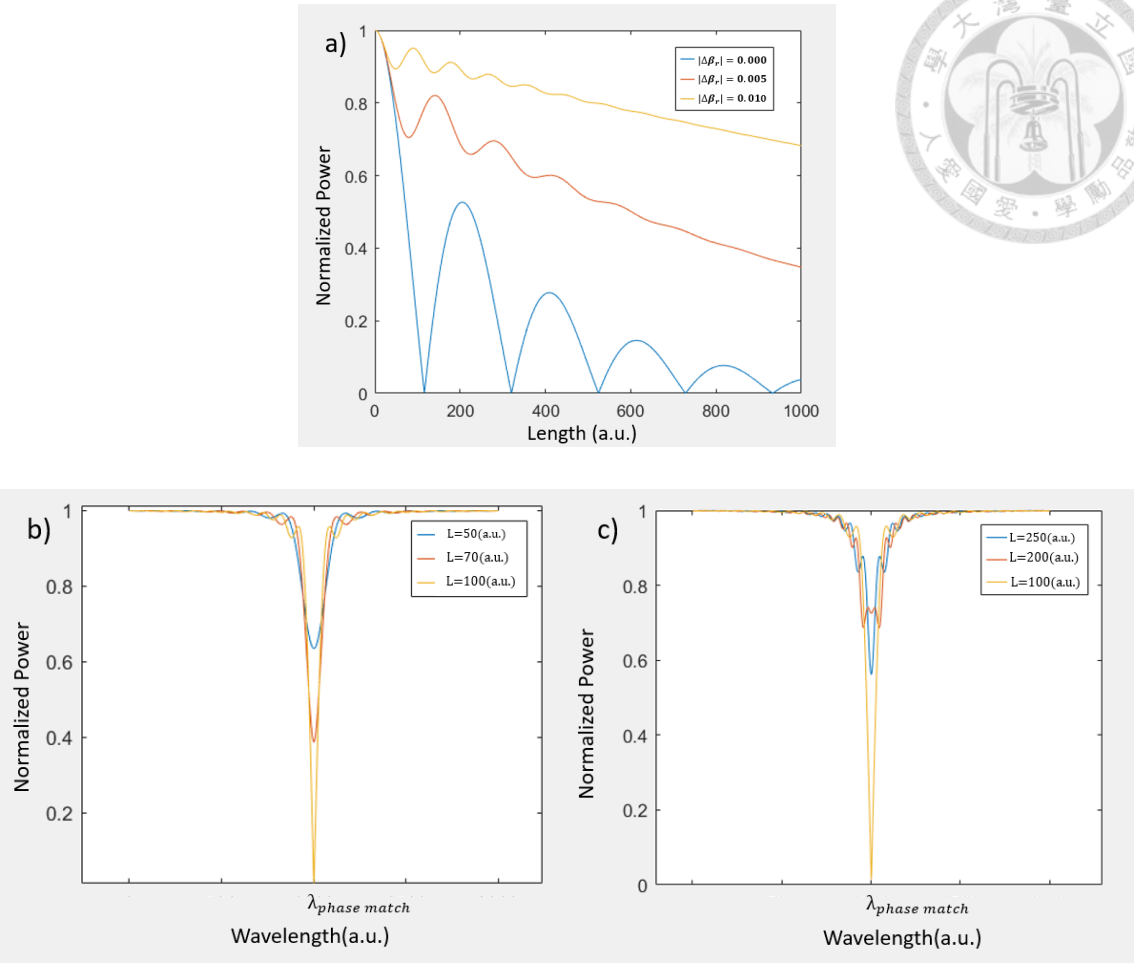

Fig. 4-15 (a) Power along the waveguide in the sensor region at different propagation constant difference for over coupled condition. (b) The optical spectrum for different sensor length based on exact condition in (a). (c) The optical spectrum for different sensor length based on exact condition in (a).

doi:10.6342/NTU202204042

4.5 Performance of Sensor

4.5.1 Sensitivity

From the precious section, we know that the local minimum in a sensor's optical spectrum is at the phase matching wavelength. The real part of effective mode index of the sensing's element and waveguide will be as denoted as $N_{eff,\ sr}$ and $N_{eff,\ w}$ respectively. When the analyte's RI, n_s changes, the $N_{eff,\ sr}$ vs λ curve of the sensing element's optical mode changes causing a change to the phase matching wavelength as well (Fig. 4-15). The ratio of change in phase matching wavelength to the change in n_s is therefore the sensitivity, S:

$$S = \frac{\delta\lambda}{\delta n_s} \tag{4.26}$$

(Note that δ in Eq. (4.26) is not the same one as in Eq. (4.20c). It is the symbol for small change here)

In Fig. 4-16, the black line (right) is the $N_{eff,\ sr}$ vs λ curve when the analyte's RI is n_s. When the analyte's RI changes from n_s to $n_s + \delta n_s$, $N_{eff,\ sr}$ at every wavelength shift by $\delta N_{eff,\ sr}$ and a new $N_{eff,\ sr}$ vs λ curve is drawn (left black line). The gradient of the black line when the analyte's RI is n_s and $n_s + \delta n_s$ are $\left(\frac{\partial N_{eff,\ sr}}{\partial\lambda}\right)_{n_s}$ and $\left(\frac{\partial N_{eff,\ sr}}{\partial\lambda}\right)_{n_s+\delta n_s}$ respectively. The green line in Fig. 4-15 is the $N_{eff,\ w}$ vs λ of the waveguide and its gradient is $\left(\frac{dN_{eff,\ w}}{d\lambda}\right)$.

If δn_s is small:

$$\left(\frac{\partial N_{eff,\ sr}}{\partial\lambda}\right)_{n_s} = \left(\frac{\partial N_{eff,\ sr}}{\partial\lambda}\right)_{n_s+\delta n_s} \tag{4.27}$$

doi:10.6342/NTU202204042

Another approximation that we can be make is that $\left(\frac{\partial \mathrm{N}_{eff,\ w}}{\partial \lambda}\right)$ and $\left(\frac{\partial \mathrm{N}_{eff,\ sr}}{\partial \lambda}\right)_{n_s}$ are both constant if the wavelength range is small. With these approximations and some trigonometry, we can derive $\delta\lambda$ and the sensitivity of a sensor, S can then be expressed as ratio between $\delta\lambda$ and δn_s.

$$\delta\lambda = \frac{\delta \mathrm{N}_{eff,sr}}{\left(\frac{\partial \mathrm{N}_{eff,\ sr}}{\partial \lambda}\right)_{n_s} - \left(\frac{d\mathrm{N}_{eff,w}}{d\lambda}\right)} \tag{4.28a}$$

$$\delta \mathrm{N}_{eff,\ sr} = \left(\frac{\partial \mathrm{N}_{eff,sr}}{\partial \mathrm{n}_s}\right)_{\lambda} \delta n_s \tag{4.28b}$$

$$\mathrm{S} = \frac{\delta\lambda}{\delta n_s} = \frac{\left(\frac{\partial \mathrm{N}_{eff,sr}}{\partial \mathrm{n}_s}\right)_{\lambda}}{\left(\frac{\partial \mathrm{N}_{eff,\ sr}}{\partial \lambda}\right)_{n_s} - \left(\frac{d\mathrm{N}_{eff,w}}{d\lambda}\right)} \tag{4.28c}$$

where $\left(\frac{\partial \mathrm{N}_{eff,sr}}{\partial \mathrm{n}_s}\right)_{\lambda}$ is the gradient of $\mathrm{N}_{eff,sr}\ vs\ \mathrm{n}_s$ curve at constant wavelength, $\left(\frac{\partial \mathrm{N}_{eff,\ sr}}{\partial \lambda}\right)_{n_s} - \left(\frac{d\mathrm{N}_{eff,w}}{d\lambda}\right)$ is the angle between $\mathrm{N}_{eff,w}\ vs\ \lambda$ curve and $\mathrm{N}_{eff,sr}\ vs\ \lambda$ curve.

From the numerator term in Eq. (4.28c), we can see that to increase sensitivity, we have to design a sensing element to have huge change in $\mathrm{N}_{eff,sr}$ when n_s changes. Another not so intuitive result is that we can increase the sensitivity by designing the waveguide so that $\left(\frac{\partial \mathrm{N}_{eff,\ sr}}{\partial \lambda}\right)_{n_s} - \left(\frac{d\mathrm{N}_{eff,w}}{d\lambda}\right)$ decreases in value as seen from the denominator in Eq. (4.28c). If the difference in gradient approaches 0, the sensitivity will approach infinity, however at the cost of infinitely large FHWM as would be discussed in the next section.

doi:10.6342/NTU202204042

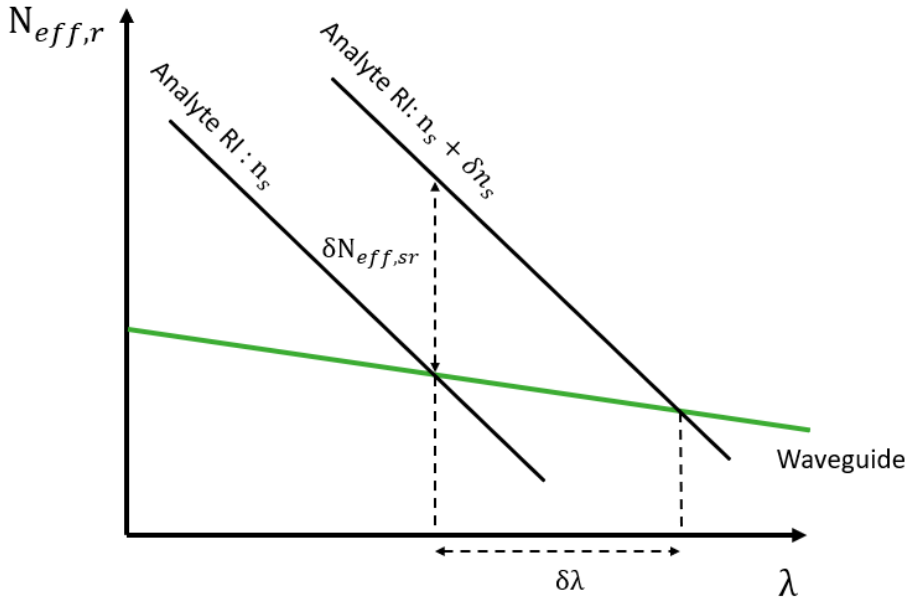

Fig. 4-16 (Black line) Real part of effective index of optical mode of sensing element (Green line) Real part of effective index of waveguide mode

doi:10.6342/NTU202204042

4.5.2 FWHM

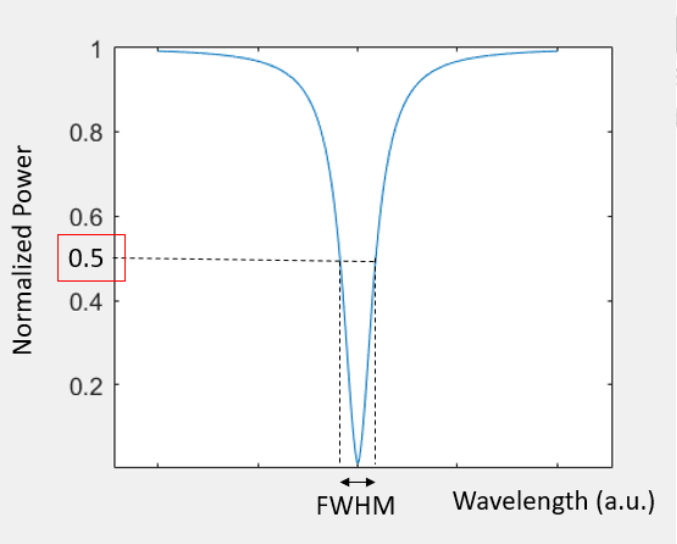

Fig. 4-17 FHWM of a sensor's signal

Full width half maximum (FWHM) of a sensor signal is the spectral width of the signal at half its maximum which is an important parameter to determine the resolution of a sensor (Fig. 4-17). For two sensors with same κ and $\beta_{2,i}$, the $P(L)\ vs\ \Delta\beta_r$ curve would be identical, however their FHWM would not be necessarily identical. This is because $\Delta\beta_r$ itself is a function of λ, $\Delta N_{eff,r}$. From Fig. (4-18), we can derive $\Delta\beta_r$ in terms of $\Delta N_{eff,r}$ and λ. Assuming Δλ is small ($\lambda_1 \approx \lambda_3$):

$$\Delta\beta_r = \frac{2\pi}{\lambda_3}\Delta N_{eff,r} \cong \frac{2\pi}{\lambda_1}\Delta N_{eff,r} \tag{4.29}$$

Expressing $\Delta N_{eff,r}$ in terms of $\left(\frac{\partial N_{eff,\,sr}}{\partial\lambda}\right)_{n_s}$ and $\left(\frac{dN_{eff,w}}{d\lambda}\right)$, we get

$$\Delta N_{eff,r} = \left[\left(\frac{\partial N_{eff,\,sr}}{\partial\lambda}\right)_{n_s} - \left(\frac{dN_{eff,w}}{d\lambda}\right)\right]\Delta\lambda \tag{4.30}$$

$$\Delta\beta_r = \frac{2\pi}{\lambda_1}\left[\left(\frac{\partial N_{eff,\,sr}}{\partial\lambda}\right)_{n_s} - \left(\frac{dN_{eff,w}}{d\lambda}\right)\right]\Delta\lambda \tag{4.31}$$

Then, we can get FHWM of the sensor:

doi:10.6342/NTU202204042

$$\mathrm{FHWM} = 2\Delta\lambda = 2\left(\lambda_{-3dB} - \lambda_{phase\ match}\right) \qquad (4.32)$$

$$= \frac{\Delta\beta_{r,-3dB}}{\frac{2\pi}{\lambda_1}\left[\left(\frac{\partial \mathrm{N}_{eff,\ sr}}{\partial\lambda}\right)_{n_s} - \left(\frac{d\mathrm{N}_{eff,w}}{d\lambda}\right)\right]}$$

Where $\Delta\beta_{r,-3dB}$ is at the wavelength λ_{-3dB}, where power is half compared to power at phase matching wavelength. $\Delta\beta_{r,-3dB}$ is a function of κ, $\beta_{2,i}, and\ L$.

$$\Delta\beta_{r,-3dB} = f(\kappa, \beta_{2,i}, L) \qquad (4.33)$$

Also, from Eq. (4.32), we can see that angle between $\mathrm{N}_{eff,w}\ vs\ \lambda$ curve and $\mathrm{N}_{eff,sr}\ vs\ \lambda$ curve, $\left(\frac{\partial \mathrm{N}_{eff,\ sr}}{\partial\lambda}\right)_{n_s} - \left(\frac{d\mathrm{N}_{eff,w}}{d\lambda}\right)$ also plays a role in FWHM. In Fig. 4-19a, let us consider two sensors with different sensing element but same waveguide where the sensing element on both sensors have the same κ, $\beta_{2,i}$ and L. We can see that the sensor with higher angle difference has higher FWHM (Fig. 4-19b). As the angle difference approaches infinity, the FHWM approaches 0, however the sensitivity approaches 0 as well as seen from Eq. (4.25).

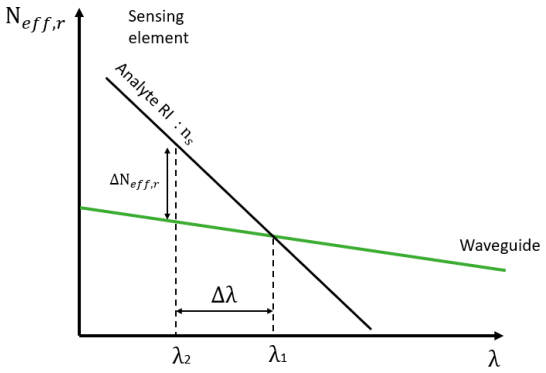

Fig. 4-18 $N_{eff,r} vs\ \lambda$ for the sensing element and waveguide

doi:10.6342/NTU202204042

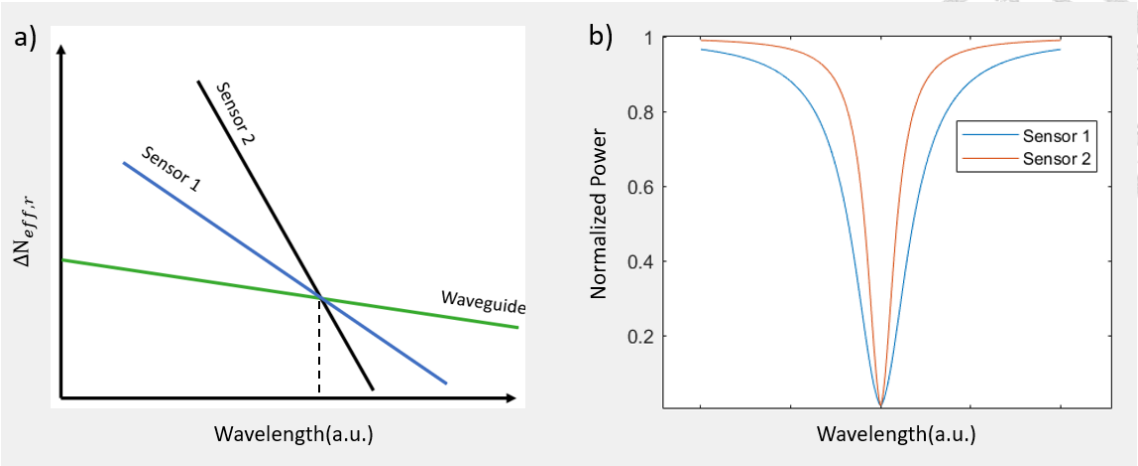

Fig. 4-19 (a) $N_{eff,r} vs\ \lambda$ for two different sensing element and a waveguide. (b) Optical spectrum of the two sensors from (a).

To see the effect of $\beta_{2,i}$ and κ on $\Delta\beta_{r,-3dB}$, $\Delta\beta_{r,-3dB}$ is plotted against $\frac{\kappa}{\beta_{2,i}}$ at different $\beta_{2,i}$ value. As $\beta_{2,i}$ is a function of the length of the sensor, we define the length of the sensor, $L_{0.01}$ such that the power at phase matched wavelength at this length has decayed to 0.01 of input power, $P(L_{0.01}) = 0.01P_{in}$. From Fig. 4-20, we can see that a local minimum exists at $\frac{\kappa}{\beta_{2,i}} \approx 0.85$ for all values of $\beta_{2,i}$ which is in the over coupling region. When we are optimizing $\Delta\beta_{r,-3dB}$ during the design stage of our sensor, we can change the distance between the sensing element and waveguide to manipulate κ so that $\frac{\kappa}{\beta_{2,i}}$ reaches 0.85 where the local minimum $\Delta\beta_{r,-3dB}$ occurs. However, if $\beta_{2,i}$ is too large, even with the distance between the sensor element and waveguide reaching 0, the maximum κ might be too small for $\frac{\kappa}{\beta_{2,i}} = 0.85$. Also, with lower $\beta_{2,i}$, $\Delta\beta_{r,-3dB}$ is smaller when $\frac{\kappa}{\beta_{2,i}}$ is kept constant. Both of these points indicate that low loss increases flexibility for optimizing FWHM and decreases the minimum possible FWHM of a sensor.

doi:10.6342/NTU202204042

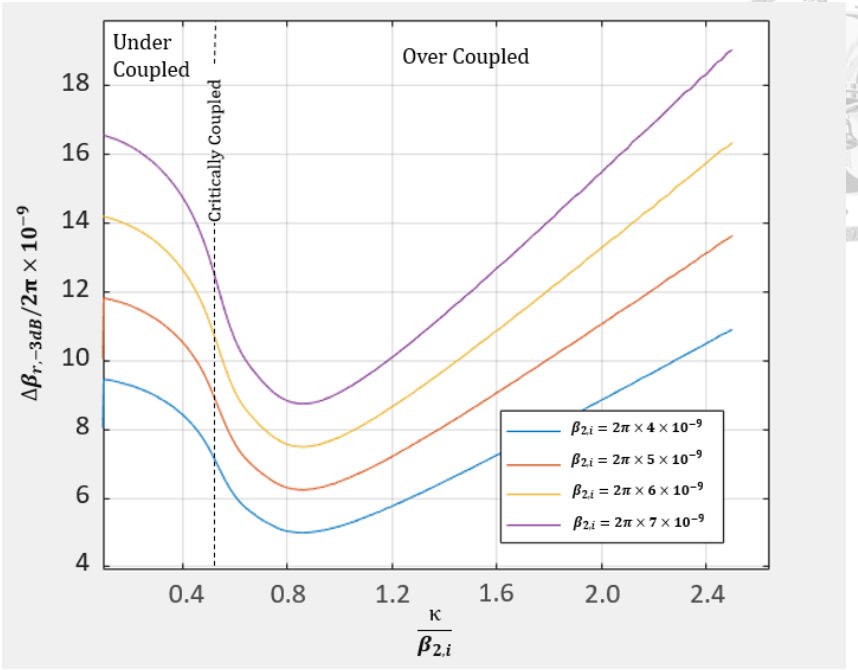

Fig. 4-20 Graph of $\Delta\beta_{r,-3dB}$ against $\frac{\kappa}{\beta_{2,i}}$ at different $\beta_{2,i}$ value at $L_{0.01}$

4.5.3 Length

Lastly, we will plot $L_{0.01}$ against $\frac{\kappa}{\beta_{2,i}}$ curve for different $\beta_{2,i}$ to investigate the effect of $\beta_{2,i}$ and κ on the length of sensor (Fig. 4-21). We can see that $L_{0.01}$ increases as $\beta_{2,i}$ decreases when $\frac{\kappa}{\beta_{2,i}}$ is kept constant and $L_{0.01}$ decreases when $\frac{\kappa}{\beta_{2,i}}$ increases as $\beta_{2,i}$ is kept constant. This means that lower loss increases required sensor length while higher coupling coefficient decreases sensor length.

doi:10.6342/NTU202204042

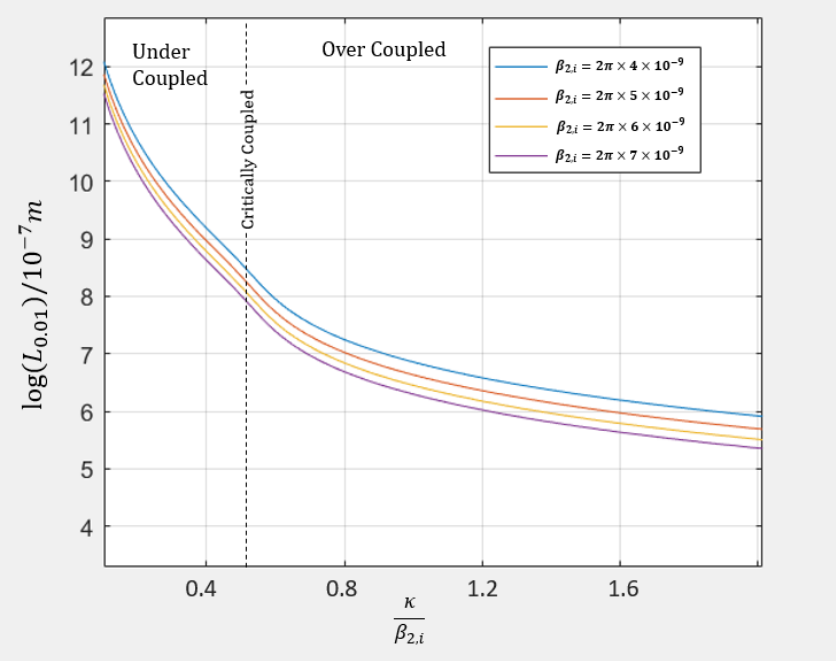

Fig. 4-21 Graph of $\Delta\beta_{r,-3dB}$ against $\frac{\kappa}{\beta_{2,i}}$ at different $\beta_{2,i}$ value at $L_{0.01}$

4.5.4 FOM

One of the other frequently used performance parameters is Figure of Merit (FOM). It is the ratio between sensitivity and FWHM of a sensor and is an indicator for the overall performance of a sensor.

$$\text{FOM} = \frac{S}{FWHM} = \frac{\frac{2\pi}{\lambda_1}\left(\frac{\partial \mathrm{N}_{eff,sr}}{\partial \mathrm{n}_s}\right)_\lambda}{\Delta\beta_{r,-3dB}} \tag{4.34}$$

From Eq. (4.34), we can see that FOM increases as $\left(\frac{\partial \mathrm{N}_{eff,sr}}{\partial \mathrm{n}_s}\right)_\lambda$ increases and $\Delta\beta_{r,-3dB}$ decreases. Different from the sensitivity and FWHM, FOM is not a function of $\left(\frac{\partial \mathrm{N}_{eff,\,sr}}{\partial \lambda}\right)_{n_s} - \left(\frac{d\mathrm{N}_{eff,w}}{d\lambda}\right)$.

doi:10.6342/NTU202204042

4.6 Validation with Optical Simulation

In this section, computer simulation is used to validate the physical phenomena we observed from the analytical analysis of coupled waveguide sensor in the previous section. FDE is used to solve the optical eigenmodes in the sensor and EME is used to simulate the propagation of the optical eigenmodes along the sensor. The structure used in our simulation is a lossless round core waveguide and a rectangular dielectric lossy waveguide as sensor element (Fig. 4-22). The radius of the round waveguide, *r* is 4.1μm, the width, *w* and thickness, *t* of the rectangular sensing element is 10μm and 0.1μm respectively. The distance between the sensing element and the waveguide, d is 3μm. The refractive index of the round waveguide, n_1 is 1.4476, the refractive index rectangular sensing element, n_2 is $1.88 - 0.01\mathrm{i}$, the refractive index of the area surrounding the round core and below the rectangular waveguide, n_3 is 1.4424 and the refractive index of the area above the rectangular waveguide (analyte region), n_s is 1.321. For simplicity, the refractive index is set to be constant for all wavelength.

Fig.4-23 (a) and (b) shows the individual optical eigenmode of sensing element and waveguide respectively while Fig. 4-23 (c) and (d) shows the even and odd hybrid mode of the sensor. Fig. 4-24(a) shows the $\mathrm{N}_{eff,r}$ vs λ curve of the sensing element and the phase matching wavelength is 1.3975μm which is the wavelength at the intersection point between the two curves. Fig. 4-25(a) is the sideview of the sensor and Fig. 4-25(b)-(f) shows the electric field amplitude at the z-y plane that pass through the center axis of the round waveguide. Far from non-phase matched wavelength, the optical mode travels in the waveguide and does not couple power to the sensor Fig. 4-24(b). At phase matched wavelength, the power can couple to the sensor element and the coupling characteristic depends on the coupling coefficient to loss ratio, $\frac{\kappa}{\beta_{2,i}}$. In our structure, the

doi:10.6342/NTU202204042

coupling coefficient can be manipulated by changing *d*. Fig. 4-24(c)-(f) shows the electric field amplitude at different *d*.

As predicted in section 4.3.3, for smaller *d*, the power oscillates between the waveguide and sensing element while also decaying as seen in Fig. 4-25(e)-(f) (over coupled condition). As *d* increases, the oscillating behavior changes to pure decaying (critical coupled condition) and the decay length increases with increasing *d* (under coupled condition) as seen in Fig. 4-25(c) and (d) respectively. Fig. 4-26 shows the power in the waveguide along the length of the sensor for different *d* while keeping $\beta_{2,i}$ constant. Apart from coupling coefficient, we can also change the coupling characteristics by manipulating the loss of the sensing element, $\beta_{2,i}$. Fig. 4-26 shows the power in the waveguide along the length of the sensor for different $\beta_{2,i}$ while keeping d constant. As $\beta_{2,i}$ increases, the power flow along the waveguide and sensing element changes from decay oscillating to pure decaying and the decaying length increases for pure decaying condition as $\beta_{2,i}$ continues to increase.

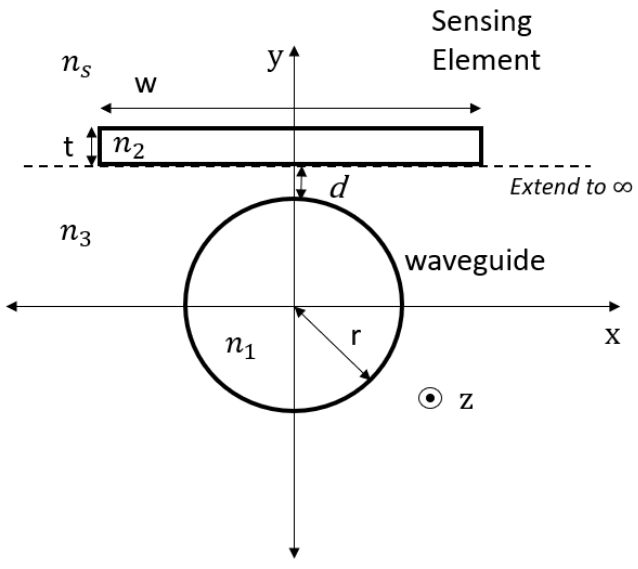

Fig. 4-22 The axial cross section of the sensing structure.

doi:10.6342/NTU202204042

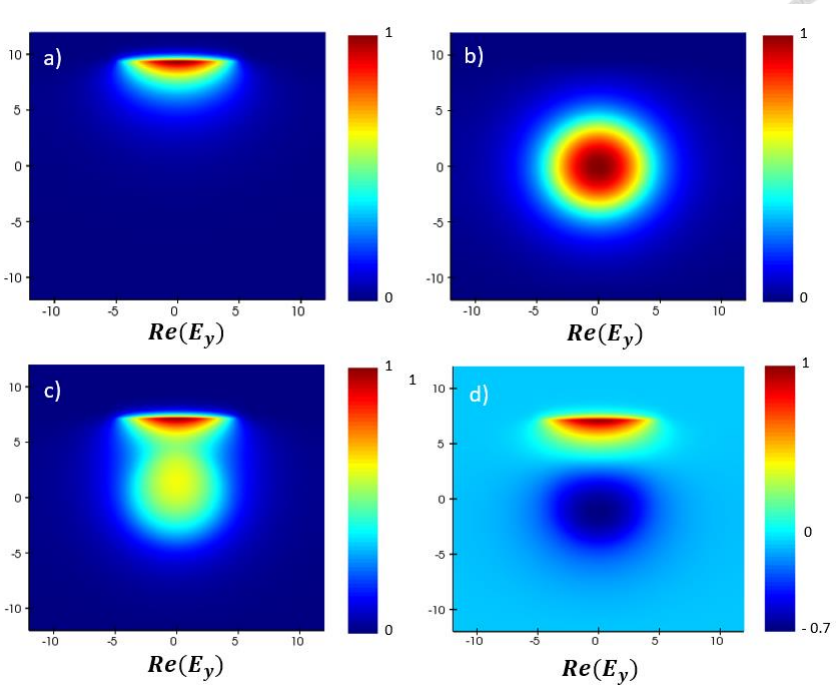

Fig. 4-23 (a)Individual mode of sensor (b) Individual mode of waveguide (c)-(d) even and odd supermode

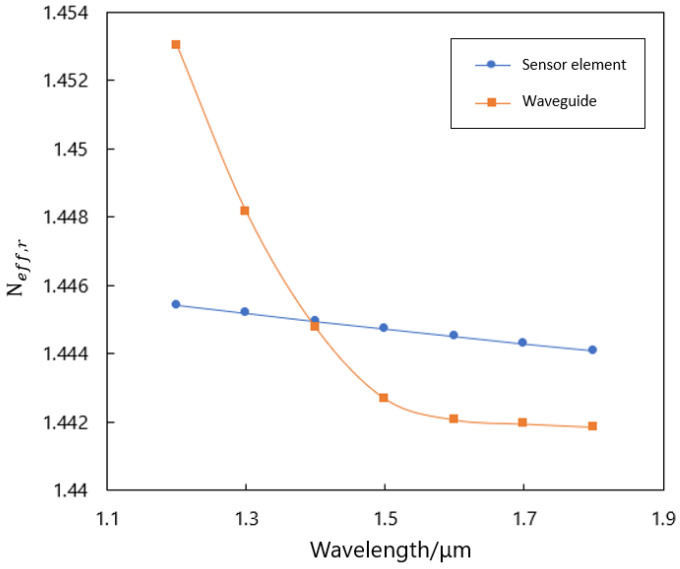

Fig. 4-24 Neff, r of sensor element and waveguide against wavelength

doi:10.6342/NTU202204042

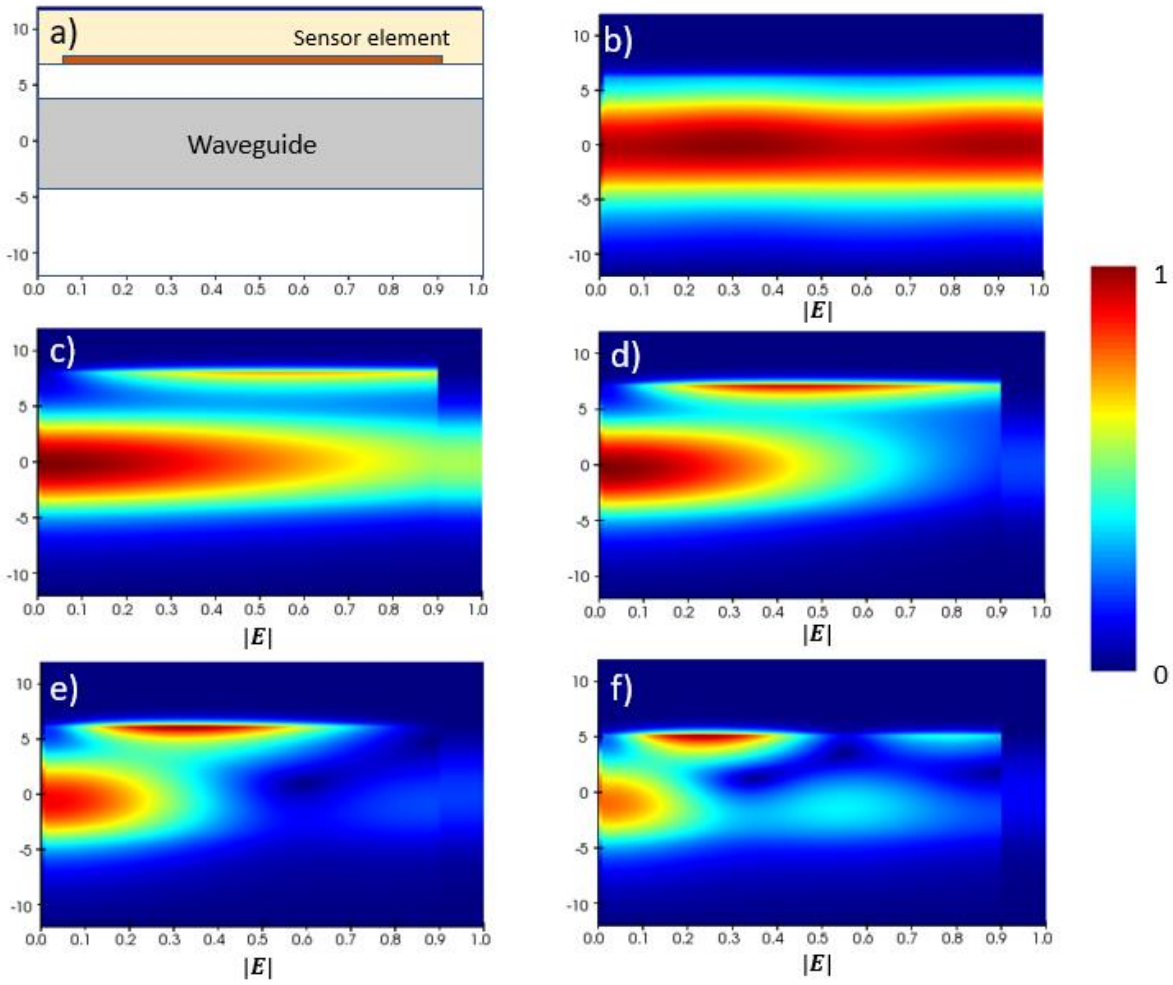

Fig. 4-25 (a) Sideview of sensor (b) Non-phase match condition (c)-(f) Phase matched condition with decreasing distance, *d* between sensor element and waveguide. (c) $d =$ 4 μm (d) $d = 3$ μm (e) $d = 2$ μm (f) $d = 1$ μm

doi:10.6342/NTU202204042

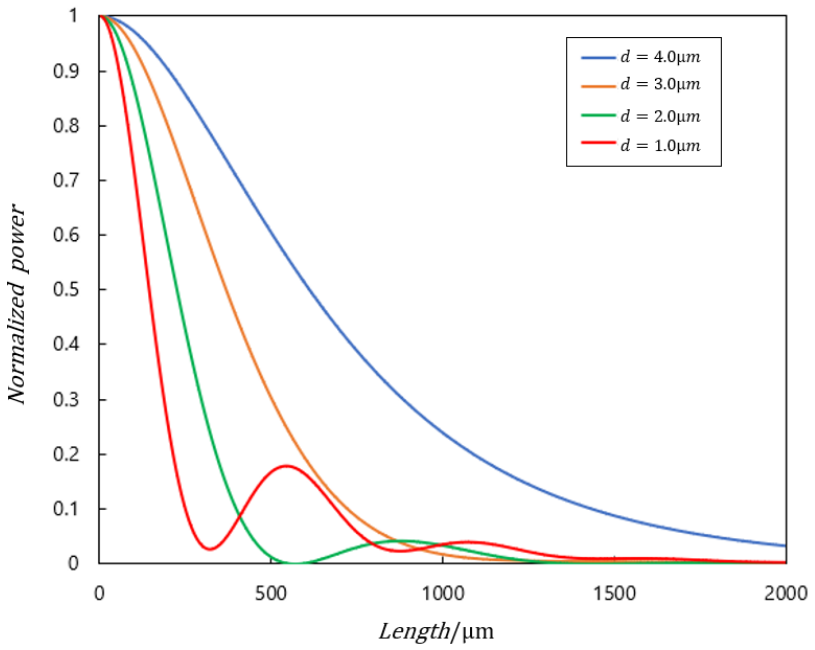

Fig. 4-26 Using d to control coupling condition

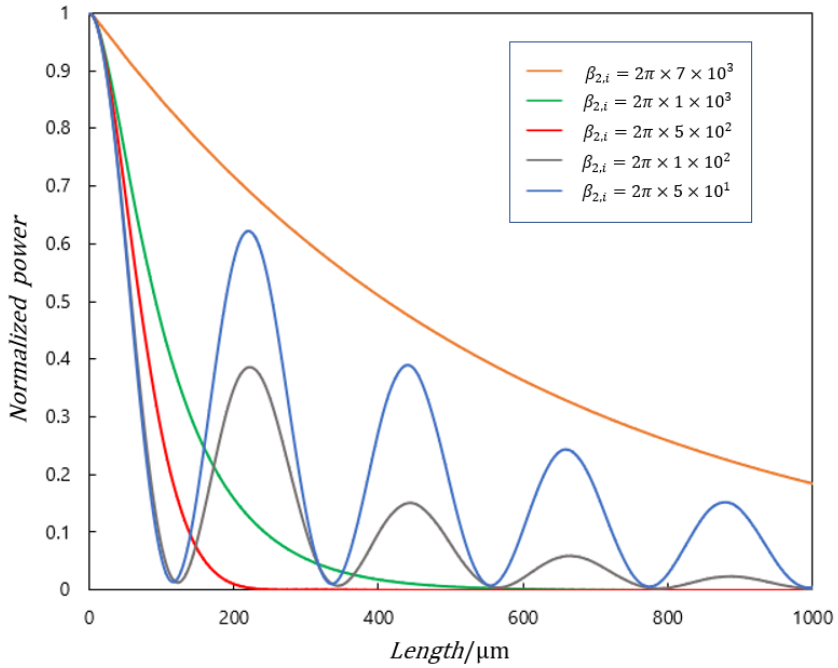

Fig. 4-27 Using loss, $\beta_{2,i}$ to control coupling condition

At near phase-matching condition, power can still couple to the sensing element but at a lower rate. The spectrum of the sensor shows a local minimum at the phase

doi:10.6342/NTU202204042

matched wavelength (Fig. 4-28) and thus the whole spectrum shifts when n_s changes. The sensitivity of this sensor with d = 2μm and length of 516μm is calculated to be 4000nm/RIU with FHWM of 170nm based on optical simulation. The FOM is calculated to be 23.5.

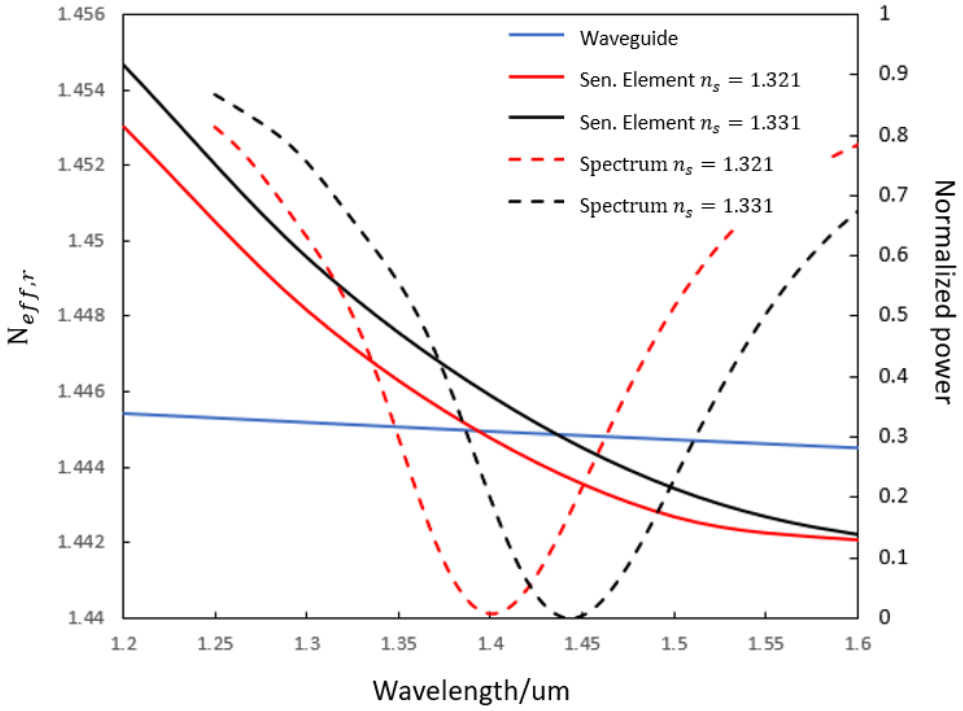

Fig. 4-28 Effective index of mode in waveguide and sensing element (Primary Axis) and spectrum of sensor at different n_s (Secondary Axis)

In the next example we will try predict the increase of the performance of the sensor in Fig. 4-22 according to Eq. (4.28), Eq (4.32) and Eq. (4.34) as a few sensor parameters are changed. This includes changing t from 100 nm to 120 nm, n_1 from 1.4476 to 1.455 which causes $\left(\frac{\partial N_{eff,sr}}{\partial n_s}\right)_\lambda$ to increase from 111 to 169 and $\left(\frac{\partial N_{eff,\,sr}}{\partial \lambda}\right)_{n_s} - \left(\frac{dN_{eff,w}}{d\lambda}\right)$ to increase from 0.025 to 0.037. The sensitivity of the new sensor is calculated to be better by 3% using Eq (4.28) while the FOM should increase by 1.52 folds using Eq. (4.34) assuming $\Delta\beta_{r,-3dB}$ does not change (we do not have calculation for $\Delta\beta_{r,-3dB}$). The

doi:10.6342/NTU202204042

spectrum of both sensors obtained using EME simulation is shown in (Fig. 4-29). The sensitivity of the new sensor from the simulation is 4000nm/RIU and does not change from the sensitivity of the old sensor as predicted. However, the FOM of the new sensor increases from 23.5 to 42.78 which is 1.82 folds the FOM of the old sensor. The FWHM of the new sensor changes from 170 to 93.5 nm compare to the old sensor. Based on FWHM and $\left(\frac{\partial N_{eff,\,sr}}{\partial \lambda}\right)_{n_s} - \left(\frac{dN_{eff,w}}{d\lambda}\right)$ value, the $\Delta\beta_{r,-3dB}$ of sensor is calculated to decrease from 4.25 to 3.46 probably due to the higher confinement of mode in new sensing element due to its higher thickness. The FOM of the sensor is calculated to increase from 26.1 to 48.8. However, the simulation shows that the FOM of the old sensor is 23.5 while the new sensor is 42.78. Overall, the equations agree well with the simulation. The difference between them might be due to the change in coupling coefficient with wavelength which we do not consider during the analysis process.

	Old Sensor	New Sensor
$\left(\frac{\partial N_{eff,sr}}{\partial n_s}\right)_{\lambda}$ / RIU^{-1}	111	169
$\left(\frac{\partial N_{eff,\,sr}}{\partial \lambda}\right)_{n_s} - \left(\frac{dN_{eff,w}}{d\lambda}\right)$/$nm^{-1}$	0.025	0.037
Sensitivity/ nm RIU^{-1}	4000(4440)	4000(4567)
FWHM/nm	170	93.5
$\Delta\beta_{r,-3dB} \times \frac{\lambda}{2\pi}$ $(\lambda = 1.5\ \mu m)$	(4.25)	(3.46)
FOM	23.5(26.1)	42.78(48.8)

Table 4-1 Performance of the new and old sensor based on simulation and calculation (calculated value in brackets).

doi:10.6342/NTU202204042

Next, we will demonstrate the effect of $\Delta\beta_{r,-3dB}$ and $\left(\frac{\partial N_{eff,\,sr}}{\partial \lambda}\right)_{n_s} - \left(\frac{dN_{eff,w}}{d\lambda}\right)$ on FWHM of the sensor spectrum. Using constant parameters, $r = 4.1\mu m$, $w = 10\mu m$, $t = 0.1\mu m$, $n_1 = 1.4476$, $n_2 = 1.88 - 0.01i$, $n_3 = 1.4424$, $n_s = 1.321$, $\left(\frac{\partial N_{eff,\,sr}}{\partial \lambda}\right)_{n_s} - \left(\frac{dN_{eff,w}}{d\lambda}\right)$ will be constant, and we can thus manipulate d to change $\Delta\beta_{r,-3dB}$ and directly see its effect on FWHM of the sensor. The FHWM vs d for two different value of $\beta_{2,i}$ is plotted in Fig. 4-30 (primary axis). For $\beta_{2,i} = 2\pi \times 1000$, we can see that there is a local minimum for FHWM at $d = 2.5\mu m$. For $\beta_{2,i} = 2\pi \times 750$, there is a minimum starting at $d = 3\mu m$. Both of this distance in the two respective sensor is the distance slightly over coupling condition occurs as seen from the slight oscillation of power from Fig. 4-31. From Fig. 4-31, power in the sensor with higher loss decays faster. Another graph plotted on Fig. 4-30 is the $L_{0.01}$against d for $\beta_{2,i} = 2\pi \times 1000$ and $\beta_{2,i} = 2\pi \times 750$. From the graph, we can see that FHWM for smaller $\beta_{2,i}$ value is smaller. Both of these phenomena observed from optical simulation generally agree well with Fig. 4-20 and Fig. 4-21. Now, we can see that by optimizing d for the sensor, we can improve the FHWM and thus improve the FOM from 23.5 when $d = 2$ to 27.02 when $d = 2.5$. We can further improve the FHWM and FOM of the sensor by changing the material of the sensor element to a lower loss material. In this case from $\beta_{2,i} = 2\pi \times 1000$ to $\beta_{2,i} = 2\pi \times 750$. The FHWM of the sensor is drop to 112 nm and the FOM increases to 35.7.

doi:10.6342/NTU202204042

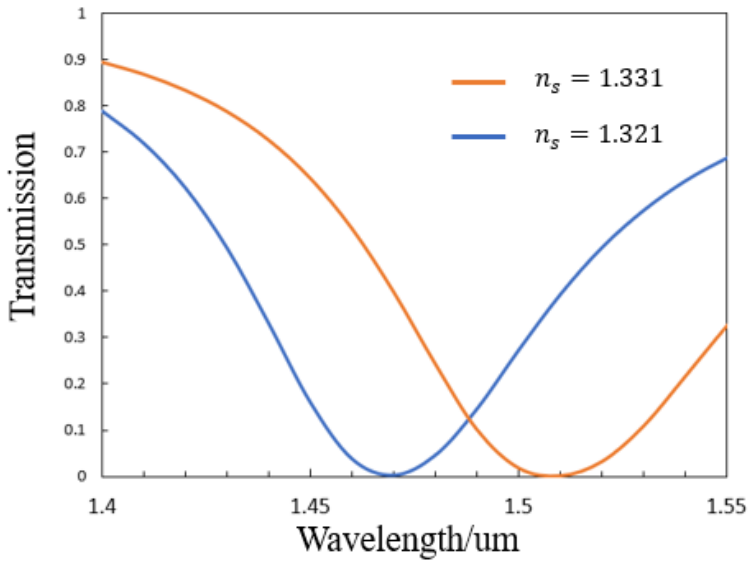

Fig. 4-29 Spectrum of new sensor

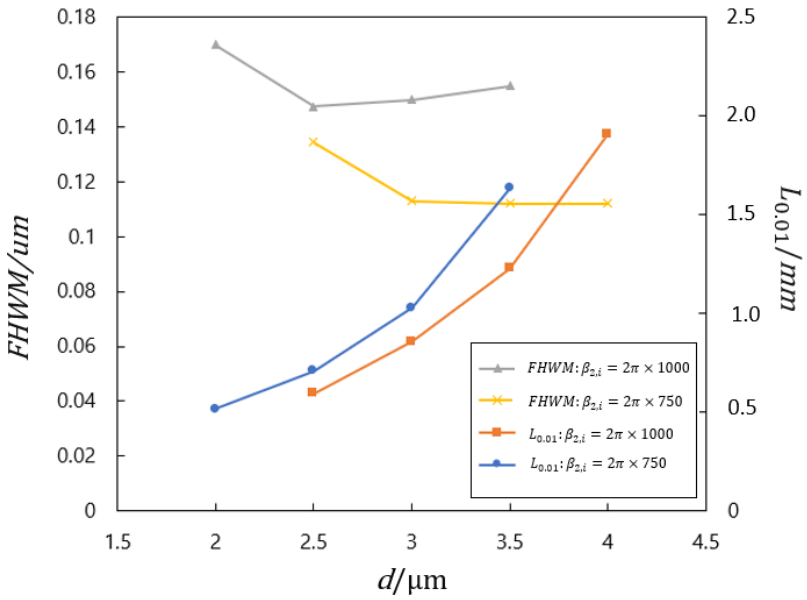

Fig. 4-30 (Primary axis) FHWM against d (Secondary axis) $L_{0.01}$against d of sensor with different loss.

doi:10.6342/NTU202204042

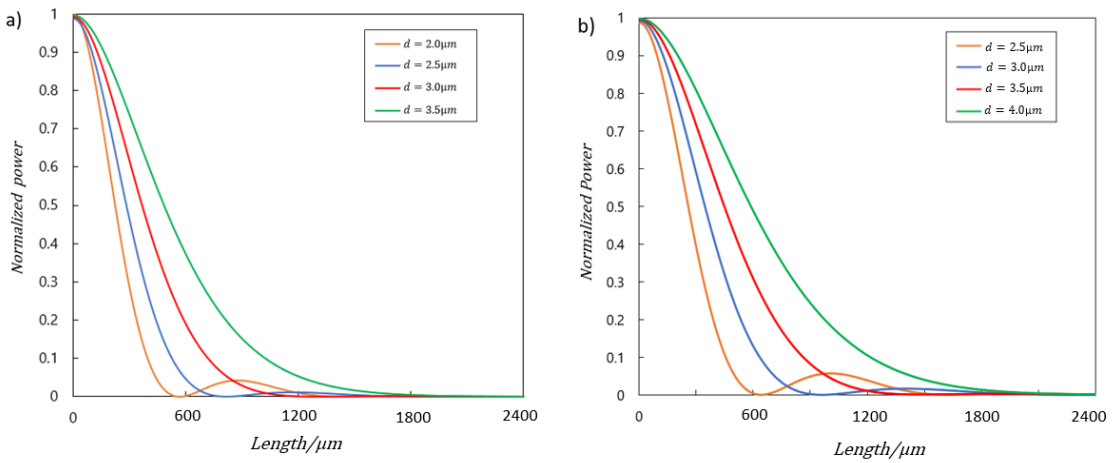

Fig. 4-31 Normalized power against length of sensor with (a) $\beta_{2,i} = 2\pi \times 1000$

(b) $\beta_{2,i} = 2\pi \times 750$

doi:10.6342/NTU202204042

4.7 Guidelines for Designing Coupled Waveguide Sensor

From the sections above, we have come up with to a few guidelines for sensor designing:

1. High $\left(\frac{\partial \mathrm{N}_{eff,sr}}{\partial \mathrm{n}_s}\right)_\lambda$: High $\left(\frac{\partial \mathrm{N}_{eff,sr}}{\partial \mathrm{n}_s}\right)_\lambda$ in sensing element increase sensitivity (Eq. 4-28) and FOM (Eq. 4-34) without sacrificing FWHM and length and therefore is the most important parameter we should aim for.
2. Low loss optical mode in sensing optimum, $\beta_{2,i}$: Reduction in loss in optical mode, $\beta_{2,i}$ decreases $\Delta\beta_{r,-3dB}$ (Fig. 4-20) and thus decreases FWHM (Eq. 4-32). As it does not have effect on sensitivity, decrease in $\beta_{2,i}$ increases FOM (E1. 4-34). However, sensor length is sacrificed (Fig. 4-21). Low loss also increases possibility of reaching $\frac{\kappa}{\beta_{2,i}}$ = 0.85 value which is the condition for lowest FWHM as there is a maximum value for κ when distance between waveguide and sensing element is 0.
3. Optimized coupling coefficient, κ : From Fig. 4-20, we can see that optimizing coupling coefficient can reduce the FWHM without changing the sensitivity and length of sensor. It can be done by changing the distance between the sensor element and waveguide. Slightly over coupled condition can provide the best balance for performance between length and FWHM.
4. Balancing angle between $N_{eff,w} vs\ \lambda$ and $N_{eff,sr} vs\ \lambda$ curve, $\left(\frac{\partial \mathrm{N}_{eff,\ sr}}{\partial \lambda}\right)_{n_s} - \left(\frac{d\mathrm{N}_{eff,w}}{d\lambda}\right)$: This parameter does not affect the FOM because an increase in it increases both sensitivity and FWHM. We can use it to tune our sensor for either higher sensitivity or lower FWHM but not both.

doi:10.6342/NTU202204042

	Sensitivity	FWHM	FOM	Length
High $\left(\frac{\partial N_{eff,sr}}{\partial n_s}\right)_{\lambda}$	Increase	No effect	Increase	No effect
Low loss, $\beta_{2,i}$	No effect	Decrease	Increase	Increase
Low $\left(\frac{\partial N_{eff,\,sr}}{\partial \lambda}\right)_{n_s} - \left(\frac{dN_{eff,w}}{d\lambda}\right)$	Increase	Increase	No effect	No effect
Optimized coupling coefficient,	No effect	Decrease	Increase	*Decrease when coupling coefficient increase

Table 4-2 Parameters in a sensor and the effect on the performance of sensor.

4.8 Summary

In this chapter, we have seen how the optical characteristics of a sensor can influence its performance and come out with some guidelines to aid in the design of a RI sensor.

doi:10.6342/NTU202204042

Chapter 5 Conclusion and Future Work

5.1 Conclusion

In this thesis, we worked on methods to improve the production and quality of SCF. We also investigated criteria for high performance coupling based waveguide RI sensor. In Chapter 2, we found the reason for low yield in production of SCF which is the formation of air bubble at the neck of the preform. We investigated the reason for air bubble formation and came up with a hypothesis which was the trapping of Taylor bubble in the melting process of the silicon powder. Through experiment, we found out that increasing the inner diameter of the preform during the drawing process is a possible solution to mitigate this problem. A new two stage drawing process was proposed to accommodate for drawing larger inner diameter preform in our lab's fiber drawing furnace. Initial experiment with larger inner diameter of 6 mm proved that our solution to mitigate air bubble formation during drawing works although there is still some small bubble inside of the molten core. In the process for troubleshooting the production of SCF, we designed and built an automated fiber drawing system so that we can control the geometry of the SCF precisely with high repeatability. It was tested to work flawlessly for drawing pure silica fiber. An intermediate preform drawing system for the use in the two-stage drawing process was also designed and built. We also investigated how the different parameters of the furnace affected the temperature of the preform through thermal modelling with COMSOL Multiphysics and verified our model with experiment.

In chapter 3, we investigated ways to improve the quality of SCF through recrystallization of silicon core by CO2 laser annealing. We carried out thermal modeling of the annealing process to find out parameters such as beam size, power,

doi:10.6342/NTU202204042

translation speed on the cooling rate of the silicon core as it is crucial in achieving large grain size. In the experiment stage, a positioning system was built to increase the stability of the annealing process. A temperature monitoring system based on thermal radiation was built to study the temperature during annealing and experiments was carried out using this system to validate our thermal simulation of the annealing process. Besides, a simulation study for single mode coupling between SMF and multimode SCF was carried out to determine the optimum SCF diameter for the highest percentage of single mode transmission in multimode SCF to lower loss in normal SCF and taper SCF. To facilitate single mode coupling between SMF and SCF, an algorithm to decompose multimode light into all its modal component was written to check for single mode transmission. Lastly, we did a near field measurement of SCF mode and found out that the loss in n and p-type SCF was extremely high compared to intrinsic SCF. We deduced that the reason is due to ineffective annealing process

In chapter 4, we used Coupled Mode Theory to determine the criteria and guidelines for improving performance in a coupled waveguide RI sensor so that we can design SCF based RI sensor in the future. We found out that sensing element with high $\left(\frac{\partial \mathrm{N}_{eff,sr}}{\partial \mathrm{n}_s}\right)_\lambda$ can increase the sensitivity and FOM of the sensor without affecting the length and FWHM of the sensor. Low loss in optical mode of the sensing element will decrease the FWHM and increase FOM although the length of the sensors needs to be increased. Low $\left(\frac{\partial \mathrm{N}_{eff,\,sr}}{\partial \lambda}\right)_{n_s} - \left(\frac{d\mathrm{N}_{eff,w}}{d\lambda}\right)$ will increase sensitivity and FWHM and has no effect on the FOM or length of the senor. There is also an optimum distance between the sensing element and waveguide for the shortest possible sensor length. A critical condition between the coupling strength and loss in optical mode of the sensing element was discovered such that for $|\beta_{2,i}| > 2\kappa$ optical power will oscillate between the

doi:10.6342/NTU202204042

waveguide and sensing element while for $|\beta_{2,i}| < 2\kappa$, optical power will couple partially from the waveguide to the sensing element once and then the power in both of them will decay together. All of the results we get from the analysis of Coupled Mode Theory on coupled waveguide sensor was validated using optical simulation.

5.2 Future Work

The utmost important future work is to produce SCF of high quality in high and stable yield so that experiments with SCF can be carried out. Therefore, a detail investigation for the melting process of silicon powder in tube should be carry out to further eliminate even the smallest air bubble in the SCF core. No literature about this process has been published so this work would be quite novel and would provide useful insight for the community drawing fiber using powder-in-tube method. After that, the proposed two stage drawing process can be tested and SCF can be test drawn using the automated system built here.

As for the improvement of the quality of SCF, methods for single crystal recrystallization such as using taper tip as seed can be tested during the annealing process. The relationship between cooling rate and grain size was not well established either and can be further investigate with the temperature monitoring system. An upgrade to CMOS camera based dichroic bolometer to improve the accuracy of the temperature measurement can also be carried out. Other unfinished work such as single mode coupling and mode decomposition can be carried out when SCF with low loss can be fabricated. Lastly, a SCF based RI sensor has yet to be designed in our lab and therefore can be carried out based on the guidelines listed in Chapter 4.

doi:10.6342/NTU202204042

REFERENCES

[1]Bayindir, Mehmet, et al. "Metal–insulator–semiconductor optoelectronic fibres." *Nature* 431.7010 (2004): 826-829.

[2] Mehta, P., et al. "All-optical modulation using two-photon absorption in silicon core optical fibers." *Optics express* 19.20 (2011): 19078-19083.

[3] Mehta, P., et al. "Nonlinear transmission properties of hydrogenated amorphous silicon core optical fibers." *Optics express* 18.16 (2010): 16826-16831.

[4] Shen, L., et al. "Four-wave mixing and octave-spanning supercontinuum generation in a small core hydrogenated amorphous silicon fiber pumped in the mid-infrared." *Optics Letters* 39.19 (2014): 5721-5724.

[5] Wu, Dong, et al. "Net optical parametric gain in a submicron silicon core fiber pumped in the telecom band." *APL Photonics* 4.8 (2019): 086102.

[6] Sohanpal, Ronit, et al. "Parametric frequency comb generation using silicon core fiber." *2021 Optical Fiber Communications Conference and Exhibition (OFC)*. IEEE, 2021.

[7] Peacock, Anna C., et al. "Wavelength conversion and supercontinuum generation in silicon optical fibers." *IEEE Journal of Selected Topics in Quantum Electronics* 24.3 (2017): 1-9.

[8] Bass M 2010 Handbook of Optics: Volume IV—Optical Properties of Materials, Nonlinear Optics, Quantum Optics 3rd edn (New York: McGraw-Hill) ch5

[9] Eggleton, et al., "Chalcogenide photonics." Nature photonics 5.3 (2011): 141-148.

[10] Peacock, Anna C., and Noel Healy. "Semiconductor optical fibres for infrared applications: A review." *Semiconductor Science and Technology* 31.10 (2016): 103004.

doi:10.6342/NTU202204042

[11] Sazio, Pier JA, et al. "Microstructured optical fibers as high-pressure microfluidic reactors." *Science* 311.5767 (2006): 1583-1586.

[12] Coco, Michael G., et al. "HPCVD of ZnSxSe1–x Claddings for ZnSe Optical Fibers." *Novel Optical Materials and Applications*. Optical Society of America, 2021.

[13] Matres, J., et al. "High nonlinear figure-of-merit amorphous silicon waveguides." *Optics express* 21.4 (2013): 3932-3940.

[14] Ballato, J., et al. "Silicon optical fiber." *Optics express* 16.23 (2008): 18675-18683.

[15] Ren, Haonan, et al. "Tapered silicon core fibers with nano-spikes for optical coupling via spliced silica fibers." *Optics Express* 25.20 (2017): 24157-24163.

[16] Healy, Noel, et al. "CO2 laser-induced directional recrystallization to produce single crystal silicon-core optical fibers with low loss." *Advanced Optical Materials* 4.7 (2016): 1004-1008.

[17] Kudinova, M., et al. "Silicon-core optical fiber with losses below 0.2 dB/cm." *Specialty Optical Fibers*. Optical Society of America, 2020.

[18] Ordu, Mustafa, et al. "Effect of thermal annealing on mid-infrared transmission in semiconductor alloy-core glass-cladded fibers." *Advanced Fiber Materials* 2.3 (2020): 178-184.

[19] Gupta, N., et al. "Annealing of silicon optical fibers." *Journal of Applied Physics* 110.9 (2011): 093107. 1

[20] Ji, Xiaoyu, et al. "Single-crystal silicon optical fiber by direct laser crystallization." *ACS Photonics* 4.1 (2017): 85-92.

[21] Healy, Noel, et al. "CO2 laser-induced directional recrystallization to produce single crystal silicon-core optical fibers with low loss." *Advanced Optical Materials* 4.7 (2016): 1004-1008.

doi:10.6342/NTU202204042

[22] Iverson, R. B., and R. Reif. "Recrystallization of amorphized polycrystalline silicon films on SiO2: Temperature dependence of the crystallization parameters." *Journal of applied physics* 62.5 (1987): 1675-1681.

[23] Zhao, Ziwen, et al. "CO 2 laser annealing of Ge core optical fibers with different laser power." *Optical Materials Express* 9.3 (2019): 1333-1347.

[24] Hunsperger, Robert G., A. Yariv, and A. Lee. "Parallel end-butt coupling for optical integrated circuits." *Applied optics* 16.4 (1977): 1026-1032.

[25] Sim, Dong Hoon, Yuichi Takushima, and Yun C. Chung. "High-speed multimode fiber transmission by using mode-field matched center-launching technique." *Journal of Lightwave Technology* 27.8 (2009): 1018-1026.

[26] Shiraishi, Kazuo, Yoshizo Aizawa, and Shojiro Kawakami. "Beam expanding fiber using thermal diffusion of the dopant." *Journal of lightwave technology* 8.8 (1990): 1151-1161.

[27] Kose, Bulent, et al. "Performance of single-mode transmission over multimode fiber: Offset launch vs fundamental mode launch." *Optical Fiber Communication Conference*. Optica Publishing Group, 2021.

[28] Li, Qian, et al. "Production of monodisperse gold nanobipyramids with number percentages approaching 100% and evaluation of their plasmonic properties." *Advanced Optical Materials* 3.6 (2015): 801-812.

[29]Rao, Yun-Jiang. "Recent progress in fiber-optic extrinsic Fabry–Perot interferometric sensors." *Optical Fiber Technology* 12.3 (2006): 227-237.

[30] Foreman, Matthew R., Jon D. Swaim, and Frank Vollmer. "Whispering gallery mode sensors." *Advances in optics and photonics* 7.2 (2015): 168-240.

doi:10.6342/NTU202204042

[31]Svedendahl, Mikael, et al. "Refractometric sensing using propagating versus localized surface plasmons: a direct comparison." *Nano letters* 9.12 (2009): 4428-4433.

[32]Wang, Qi, and Wan-Ming Zhao. "A comprehensive review of lossy mode resonance-based fiber optic sensors." *Optics and Lasers in Engineering* 100 (2018): 47-60.

[33]Mishra, Satyendra Kumar, Bing Zou, and Kin Seng Chiang. "Surface-plasmon-resonance refractive-index sensor with Cu-coated polymer waveguide." *IEEE photonics technology letters* 28.17 (2016): 1835-1838.

[34]Arregui, Francisco J., et al. "Giant sensitivity of optical fiber sensors by means of lossy mode resonance." *Sensors and Actuators B: Chemical* 232 (2016): 660-665. 8

[35] Testa, Genni, et al. "Planar silicon-polydimethylsiloxane optofluidic ring resonator sensors." *IEEE Photonics Technology Letters* 28.2 (2015): 155-158.

[36] Wang, Da-Shin, and Shih-Kang Fan. "Microfluidic surface plasmon resonance sensors: From principles to point-of-care applications." *Sensors* 16.8 (2016): 1175.

[37]Nooke, Alida, et al. "On the application of gold based SPR sensors for the detection of hazardous gases." *Sensors and Actuators B: Chemical* 149.1 (2010): 194-198.

[38]BASAK, RAJAT KUMAR. *Development of Specialty Photonic Crystal Fiber for Plasmonic Applications*. Diss. CSIR-Central Glass and Ceramic Research Institute, 2018.

[39] Cheng, Xu, and Yogesh Jaluria. "Effect of draw furnace geometry on high-speed optical fiber manufacturing." *Numerical Heat Transfer: Part A: Applications* 41.8 (2002): 757-781.

[40] Mawardi, A., and R. Pitchumani. "Optical fiber drawing process model using an analytical neck-down profile." *IEEE Photonics Journal* 2.4 (2010): 620-629.

doi:10.6342/NTU202204042

[41] Choudhury, S. Roy, and Yogesh Jaluria. "Practical aspects in the drawing of an optical fiber." *Journal of Materials Research* 13.2 (1998): 483-493.

[42] Bretherton, Francis Patton. "The motion of long bubbles in tubes." *Journal of Fluid Mechanics* 10.2 (1961): 166-188.

[43] Sato, Yuzuru, et al. "Viscosity of molten silicon and the factors affecting measurement." *Journal of Crystal Growth* 249.3-4 (2003): 404-415.

[44] Zhao, Ning, et al. "Viscosity and surface tension of liquid Sn-Cu lead-free solders." *Journal of electronic materials* 38.6 (2009): 828-833.

[45] Magnini, M., et al. "Dynamics of long gas bubbles rising in a vertical tube in a cocurrent liquid flow." *Physical Review Fluids* 4.2 (2019): 023601.

[46] Nur, A., R. Afrianita, and R. D. T. F. Ramli. "Effect of pipe diameter changes on the properties of fluid in closed channels using Osborne Reynold Apparatus." *IOP Conference Series: Materials Science and Engineering*. Vol. 602. No. 1. IOP Publishing, 2019.

[47] Auguste, Jean-Louis, et al. "Modified powder-in-tube technique based on the consolidation processing of powder materials for fabricating specialty optical fibers." *Materials* 7.8 (2014): 6045-6063.

[48] Paek, U. C., and C. R. Kurkjian. "Calculation of cooling rate and induced stresses in drawing of optical fibers." *Journal of the American Ceramic Society* 58.7-8 (1975): 330-335.

[49] Wissuchek, Donald J., Carl W. Ponader, and James J. Price. "Analysis of residual stress in optical fiber." *Optical Fiber Reliability and Testing*. Vol. 3848. SPIE, 1999.

[50] Meng, Xiangmei, et al. "Combustion study of partially gasified willow and DDGS chars using TG analysis and COMSOL modeling." *Biomass and bioenergy* 39 (2012): 356-369.

doi:10.6342/NTU202204042

[51] Bhat, A. A., et al. "Thermal Analysis of Induction Furnace." *Proceedings of the COSMOL conference in Banglore*. 2012.

[52] Heat Transfer Module User's Guide. COMSOL Multiphysics® v. 5.6. COMSOL AB, Stockholm, Sweden. 2021

[53] CFD Module User's Guide. COMSOL Multiphysics® v. 5.3. COMSOL AB, Stockholm, Sweden. 2017

[54]Fujiwara, Kozo. "Crystal growth behaviors of silicon during melt growth processes." *International Journal of Photoenergy* 2012 (2012).

[55] Fujiwara, Kozo, et al. "Directional growth method to obtain high quality polycrystalline silicon from its melt." *Journal of Crystal Growth* 292.2 (2006): 282-285.

[56] Wang, T. Y., et al. "Grain control using spot cooling in multi-crystalline silicon crystal growth." *Journal of Crystal Growth* 311.2 (2009): 263-267.

[57] Lee, Jun-Kyu, et al. "Directional solidification behaviors of polycrystalline silicon by electron-beam melting." *Japanese Journal of Applied Physics* 52.10S (2013): 10MB09.

[58] Calder, I. D., and R. Sue. "Modeling of cw laser annealing of multilayer structures." *Journal of Applied Physics* 53.11 (1982): 7545-7550.

[59]Dornberger, E., et al. "Thermal simulation of the Czochralski silicon growth process by three different models and comparison with experimental results." *Journal of crystal growth* 180.3-4 (1997): 461-467.

[60]Glassbrenner, C. Jo, and Glen A. Slack. "Thermal conductivity of silicon and germanium from 3 K to the melting point." *Physical review* 134.4A (1964): A1058.

[61]Okhotin, A. S., A. S. Pushkarskii, and V. V. Gorbachev, *Thermophysical Properties of Semiconductors*, Moscow, "Atom" Publ. House, 1972, (in Russian).

doi:10.6342/NTU202204042

[62] T. Sat¯o, “Spectral Emissivity of Silicon”, Japanese Journal of Applied Physics 6, 339–347 (1967).

[63]Homa, Marta, and Natalia Sobczak. "Measurements of temperature and heat of phase transformation of pure silicon by using differential scanning calorimetry." *Journal of Thermal Analysis and Calorimetry* 138.6 (2019): 4215-4221.

[64] Rhim, et al. "Thermophysical properties measurement of molten silicon by high-temperature electrostatic levitator: density, volume expansion, specific heat capacity, emissivity, surface tension and viscosity." *Journal of crystal growth* 208.1-4 (2000): 313-321.

[65]E. Takasuka, et al. “Emissivity of liquid silicon in visible and infrared regions”, Journal of Applied Physics 81, 6384–6389 (1997).

[66]Combis, Patrick, et al. "Evaluation of the fused silica thermal conductivity by comparing infrared thermometry measurements with two-dimensional simulations." *Applied Physics Letters* 101.21 (2012): 211908.

[67] Zhao, Jian, et al. "Structural modification of silica glass by laser scanning." *Journal of applied physics* 95.10 (2004): 5475-5482.

[68] Tanaka, H., et al. "Evaluation of hemispherical total emissivity for thermal radiation calorimetry." *International journal of thermophysics* 21.4 (2000): 927-940.

[69] Wang, Xiaoman, et al. "Thermal characterization of convective heat transfer in microwires based on modified steady state" hot wire" method." *arXiv preprint arXiv:1907.10751* (2019).

[70] Love, J. D., et al. "Tapered single-mode fibres and devices. Part 1: Adiabaticity criteria." *IEE Proceedings J (Optoelectronics)* 138.5 (1991): 343-354.

doi:10.6342/NTU202204042

[71] Ho, Keang-Po, and Joseph M. Kahn. "Mode-dependent loss and gain: statistics and effect on mode-division multiplexing." *Optics express* 19.17 (2011): 16612-16635.

[72] Manuylovich, Egor S., Vladislav V. Dvoyrin, and Sergei K. Turitsyn. "Fast mode decomposition in few-mode fibers." *Nature communications* 11.1 (2020): 1-9.

[73] Shapira, O., Abouraddy, A. F., Joannopoulos, J. D. & Fink, Y. Complete modal decomposition for optical waveguides. *Phys. Rev. Lett.* **94**, 143902 (2005).

[74] Lü, H., Zhou, P., Wang, X. & Jiang, Z. Fast and accurate modal decomposition of multimode fiber based on stochastic parallel gradient descent algorithm. *Appl. Opt.* **52**, 2905–2908 (2013).

[75] Reiter, Sina, et al. "Parasitic absorption in polycrystalline Si-layers for carrier-selective front junctions." *Energy Procedia* 92 (2016): 199-204.

[76] Huang, Wei-Ping, and Jianwei Mu. "Complex coupled-mode theory for optical waveguides." *Optics Express* 17.21 (2009): 19134-19152.

[77] Gonthier, François, et al. "Mode coupling in nonuniform fibers: comparison between coupled-mode theory and finite-difference beam-propagation method simulations." *JOSA B* 8.2 (1991): 416-421.

[78] Cooper, Michael L., and Shayan Mookherjea. "Numerically-assisted coupled-mode theory for silicon waveguide couplers and arrayed waveguides." *Optics Express* 17.3 (2009): 1583-1599.

[79]Ma, Aning, Yuee Li, and Xiaoping Zhang. "Coupled mode theory for surface plasmon polariton waveguides." *Plasmonics* 8.2 (2013): 769-777.

[80] Sukhorukov, Andrey A., et al. "Nonlinear coupled-mode theory for periodic plasmonic waveguides and metamaterials with loss and gain." *Optics Letters* 39.3 (2014): 462-465.

doi:10.6342/NTU202204042